2019

Supply channel heat transfer with simultaneous impingement jet array cooling and crossflow cooling

David Ritchie

SUPPLY CHANNEL HEAT TRANSFER WITH SIMULTANEOUS IMPINGEMENT JET ARRAY COOLING AND CROSSFLOW COOLING

by

DAVID RITCHIE

A THESIS

Submitted in partial fulfillment of the requirements for the degree of
Master of Science in Engineering
in
The Department of Mechanical and Aerospace Engineering
to
The School of Graduate Studies
of
The University of Alabama in Huntsville

HUNTSVILLE, ALABAMA
2019

In presenting this thesis in partial fulfillment of the requirements for a master's degree from The University of Alabama in Huntsville, I agree that the Library of this University shall make it freely available for inspection. I further agree that permission for extensive copying for scholarly purposes may be granted by my advisor or, in his/her absence, by the Chair of the Department or the Dean of the School of Graduate Studies. It is also understood that due recognition shall be given to me and to The University of Alabama in Huntsville in any scholarly use which may be made of any material in this thesis.

David Pitkin

(Student signature)

03-26-2019

(Date)

THESIS APPROVAL FORM

Submitted by David Ritchie in partial fulfillment of the requirements for the degree of Master of Science in Mechanical Engineering and accepted on behalf of the Faculty of the School of Graduate Studies by the thesis committee.

We, the undersigned members of the Graduate Faculty of The University of Alabama in Huntsville, certify that we have advised and/or supervised the candidate on the work described in this thesis. We further certify that we have reviewed the thesis manuscript and approve it in partial fulfillment of the requirements for the degree of Master of Science in Mechanical Engineering.

03-28-2014

Committee Chair

Dr. Phillip Ligrani (Date)

Dr. Keith Hollingsworth

Dr. Jason Cassibry

Department Chair

Dr. Keith Hollingsworth

College Dean

Dr. Shankar Mahalingam

Graduate Dean

Dr. David Berkowitz

ABSTRACT

The School of Graduate Studies

The University of Alabama in Huntsville

Degree Master of Science in Engineering Program Mechanical Engineering

Name of Candidate David Ritchie

Title Supply Channel Heat Transfer with Simultaneous Impingement Jet Array Cooling and Crossflow Cooling

Experimental data are provided for four different sets of experimental conditions for the coolant-side of a double wall cooled effusion test plate. Employed are three different passages for main flow, cross flow, and impingement flow. Coolant is supplied through the cross flow channel and by means of an impingement jet array to the coolant-side of the effusion test plate. This coolant then supplies all effusion hole entrances. The impingement plate and effusion plate both contain six staggered rows of 10 holes per row, where impingement holes are offset so that each is located between effusion hole entrance locations. Installed within the effusion test plate on the coolant-side is a custom-manufactured etched-foil heater, which is employed to provide a uniform surface heat flux thermal boundary condition. The inlet and outlet of the main flow passage are configured with a contraction ratio of 4 to provide a strong favorable pressure gradient with streamwise development. Liquid crystal thermography is employed to measure spatially-resolved distributions of surface Nusselt number values along the cold-side of the effusion plate. Of particular interest is the simultaneous use of cross flow and impingement flow, as associated Reynolds numbers and mass flow rates are varied. Resulting data are compared to measured data (from previous investigations) using arrangements which employed cooling air provided either by a cross flow only configuration, or by an impingement only arrangement. In the present study, surface Nusselt number distributions are strongly affected by distributions and concentrations of coolant distributed across the surface on the coolant-side of the effusion plate. Here, higher surface Nusselt number values indicate increased surface heat transfer augmentation, and improved cooling and thermal protection along on the surface. Results

indicate that the impingement-only arrangement provides the most effective distribution of coolant along the cold-side of the effusion test plate, when compared to the combination arrangements and to the cross flow only arrangements. As initial blowing ratio and impingement flow Reynolds number increase, while cross flow Reynolds number is held constant, impingement flow begins to overpower the cross flow, which leads to the higher Nusselt number values for particular test cases where cross flow is constant and impingement flow varies.

Abstract Approval: Committee Chair

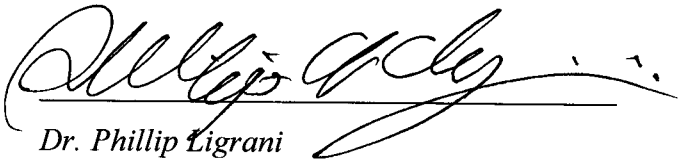

Dr. Phillip Ligrani

Department Chair

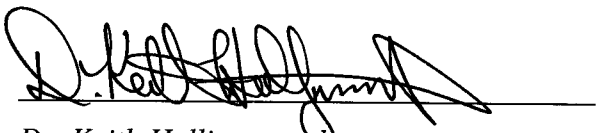

Dr. Keith Hollingsworth

Graduate Dean

Dr. David Berkowitz

ACKNOWLEDGEMENTS

I sincerely thank my advisor Dr. Phillip Ligrani for his invaluable knowledge, advice, and encouragement throughout my time working with him. I have never worked with someone as knowledgeable and as welcoming as him. It has truly been a pleasure working under his guidance. I am extremely grateful for and truly thank my teammates Dr. Zhong Ren, Sneha Vanga, and Austin Click for being wonderful friends and coworkers over the past few years. I am truly blessed to have been able to work with and learn from them. I also thank them for helping me with the experimental data collection and analysis. Finally, I would like to thank my parents, family, and friends from the bottom of my heart for their never-ending love and support.

TABLE OF CONTENTS

LIST OF FIGURES

LIST OF TABLES

Table PAGE

LIST OF SYMBOLS

A	area
B	blue
BR	film cooling blowing ratio
C	Sutherland's formula constant
C_d	discharge coefficient
CR	contraction ratio
c	specific heat
DH	hydraulic diameter
DR	density ratio
d	diameter
G	green
h	hue angle
h	heat transfer coefficient
I	current
I	momentum flux ratio
K	flow coefficient
k	thermal conductivity
LED	light emitting diode
l	distance between thermocouple and surface
M	Mach number
$\dot{m}$	mass flow rate
N_e	number of holes in the film cooling test plate
N_i	number of holes in the impingement plate
P	power
PVC	light emitting diode
ΔP_e	differential pressure through film cooling plate
ΔP_i	differential pressure through impingement plate
ΔP_{or}	differential pressure through ASME orifice plate
P_s	static pressure

P_d	dynamic pressure
P_t	stagnation pressure
Q	heat (power)
q	heat flux
R	red
R	gas constant
Re	Reynolds number
T_i	initial temperature
T_r	thermocouple recovery temperature
T_s	static temperature
T_t	stagnation temperature
T_w	wall temperature
T_0	reference static temperature
t	thickness of PVC plastic
V	voltage
VR	velocity ratio
V	flow velocity
x	streamwise coordinate
y	spanwise coordinate

Greek symbols

α	thermocouple recovery factor
γ	specific heat ratio
μ	dynamic viscosity
μ_0	reference dynamic viscosity
ρ	density
ρ_s	static air density
ν	kinematic viscosity

Subscripts

Avg	average values along test plate
crct	corrected
cf	crossflow
CL	centerline
DH	hydraulic diameter
e	film cooling plate
i	impingement plate
ht	film heater
Local	local values along effusion test plate
LC	liquid crystal
ms	main flow
or	orifice plate
pipe	connecting impingement plenum pipe
PVC	polyvinyl chloride
pst	polystyrene
s	static
t	stagnation
tc	thermocouple
w	wall

CHAPTER 1

INTRODUCTION

The current experiment incorporates a facility residing at the Propulsion Research Center of the University of Alabama in Huntsville. This facility is designed and constructed to simulate double wall cooling, similar to arrangements employed within combustion chamber liners of gas turbine engines. Employed are three flow passages, as shown in Figures 1 and 2. These channels supply full coverage film cooling flow through a combination of impingement flow and cross flow. For the main air flow passage, past studies have used a contraction ratio of 1 (Figure 1), whereas the present study uses a contraction ratio of 4 (Figure 2). Employed in the present study is simultaneous use of cross cooling flow and impingement jet array cooling. Presented are cold-side, supply channel heat transfer characteristics, measured using liquid crystal thermography.

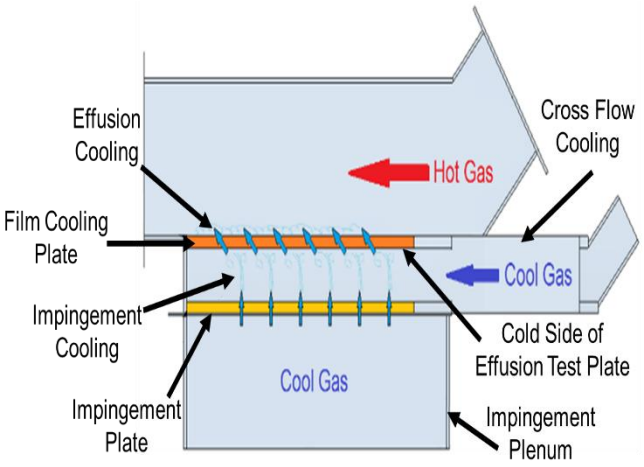

Figure 1. CR=1 double wall cooling experimental arrangement.

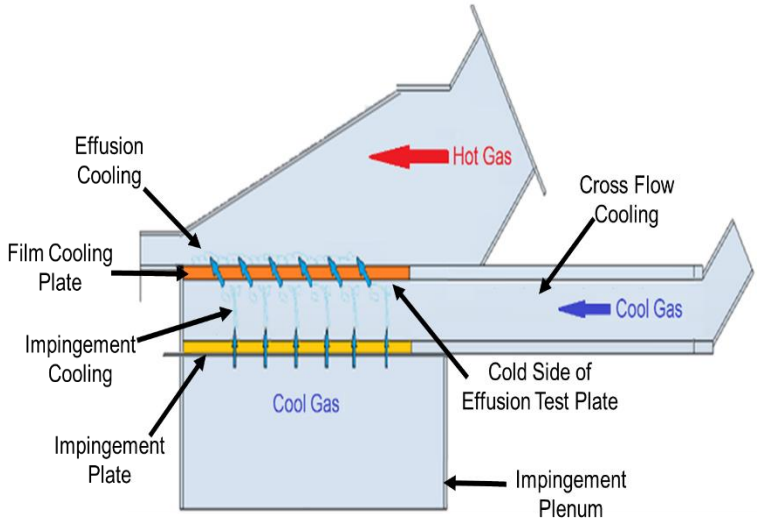

Figure 2. CR=4 double wall cooling experimental arrangement.

1.1 Overview

The present study uses three flow passages which includes a mainstream channel, a cross flow channel, and an impingement jet array channel. The impingement jet array and cross flow passages supply coolant to an effusion test plate. Coolant passes through the test plate into the mainstream by means of 6.35 mm effusion holes, angled at 25 degrees, and arranged in six staggered rows of 10 effusion holes per row. The effusion plate is 431.8 mm in the spanwise direction and 711.2 mm in the streamwise direction, seen in Figure 4. The impingement plate used to create the impingement jet array also consists of six staggered rows of 10 effusion holes per row, offset such that impingement holes are located in between effusion hole entrance locations, shown in Figure 5. Holes are separated by 15 non-dimensional streamwise hole spacings (x/d_e), and 4 spanwise hole spacings (y/d_e). Mainstream velocities of 5 m/s and 8 m/s are used to produce different mainstream Reynold number conditions for a range of blowing ratios. Blowing ratio is defined in Equation 43 for the ratio of local effusion hole exit mass flow rate to the mainstream mass flow rate, measured at the inlet of the test section. Located under the surface of the effusion test plate on the coolant-side of the plate is a custom etched-foil heater. The heater is used to uniformly heat the plate to provide a constant heat flux surface boundary condition.

To investigate cold-side characteristics, liquid crystal thermography is used for local heat transfer measurements. Four arrangements of combination impingement and cross flow are

analyzed in the present study: (1) high mainstream Reynolds number/constant cross flow Reynolds number/varying impingement Reynolds number, (2) low mainstream Reynolds number/constant cross flow Reynolds number/varying impingement Reynolds number, (3) high mainstream Reynolds number/constant impingement Reynolds number/varying cross flow Reynolds number, and (4) low mainstream Reynolds number/constant impingement Reynolds number/varying cross flow Reynolds number. A main flow passage with a contraction ratio of 4 is used to provide a strong favorable pressure gradient. As such, the present study expands on data taken by Ren (2018), where impingement flow only and cross flow only arrangements are tested for contraction ratios of one and four. Hot-side tests from Ren (2018) focus on spatially-resolved heat transfer coefficient and adiabatic film cooling effectiveness distributions, determined by means of infrared thermography. Cold-side tests from Ren (2018) employ liquid crystal thermography to measure spatially-resolved surface distributions of Nusselt numbers.

1.2 Literature Survey

Little information is known about coolant-side characteristics, because most past studies observe data on the hot-side of effusion test plates. Knowledge about coolant-side characteristics are potentially important because of their contribution to cooling effusion test plates in addition to the film cooling occurring on the hot-side of the effusion test plates. Investigations in recent years consider film cooling with different hole arrays, hole angles, and hole spacings. Two recent studies by Ren et al. (2018) and Ligrani et al. (2018) consider full-coverage film-cooling data for varying contraction ratios and different blowing ratios. Considered are hot-side and cold-side surface heat transfer distributions for cross flow only and for impingement only arrangements, with a main flow passage contraction ratio of 4. Compared to contraction ratio of 1 results, contraction ratio of 4 data generally show smaller line-averaged heat transfer coefficient values, due to decreased local blowing ratio distributions along the test plate. This causes less coolant to accumulate along and near to the surface of the test plate. Coolant-side Nusselt number data is measured using liquid crystal thermography. Cold-side line-averaged Nusselt numbers are also generally less for contraction ratio 4, than contraction ratio 1 values, when compared at similar streamwise locations, blowing ratios, and Reynolds numbers. Regardless of CR value, line-averaged Nusselt numbers, in general, increase with initial blowing ratio value. High cold-side Nusselt numbers are generally present at locations near impingement holes, as well near effusion

hole entrance locations. Of cross flow cooling and impingement cooling, impingement flow generally gives much larger values of local and line-averaged Nusselt numbers, compared to cross flow only arrangements. Only two studies by Sasaki et al. (1979) and Vinton et al. (2017) consider the effects of a main flow streamwise pressure gradient.

Most existing studies consider only the hot-side of effusion plates. For example, Sasaki et al. (1979) gives film effectiveness data for single row and multi-row staggered hole configurations. Most of the investigations mentioned only present surface distributions of film effectiveness. Among all the studies mentioned, only a study by Kelly et al (2003). presents surface heat transfer coefficient distribution. Investigative approaches in studying combustion liners cooling techniques and arrangements include a variety of experimental studies by Wang et al. (2016), Jackowski et al. (2016), Ji et al (2016), and McClintic et al. (2017), among others. Numerical approaches include studies by Sung et al. (2016) and Ledezma et al. (2016). Combined experimental and numerical approaches include investigations given by Bailey et al. (2002) and Lin et al. (2003). Hole configurations include normal, round arrangements seen in papers by Lin et al. (2003), Ji et al. (2016), and Ji et al. (2017). Sung et al. (2016), Vinton et al. (2017), and McClintic et al. (2017). present provide results for a variety of inclined, compound angle, and shaped hole arrangements by. Andrews et al. (1988) present data for various configurations of effusion and impingement cooling. According to this study, combined impingement and effusion cooling gives higher effectiveness, than impingement only. Plenum supplied and cross flow supplied film effectiveness data for multi-row staggered hole effusion cooling arrangements are given by Martiny et al. (1995) and by Bailey et al. (2002), respectively. These studies provide relationships between effectiveness, hole number, and hole diameter, which show that effectiveness is improved through an increase in number of holes, along with a decrease in hole diameter. Al Dabagh et al. (1990) focus on optimum number of impingement cooling holes for a given number of effusion holes. According to these investigations, the optimum arrangement is present when the same number of impingement and effusion cooling holes are used, and impingement cooling holes are placed and centered between effusion cooling holes

Other recent investigations consider simultaneous use of effusion and impingement cooling. Studies by Andrews et al. (1988) and Shi et al. (2016) consider only the external, effusion cooled surface, while only the internal, impingement cooled surface results are given by

investigations from Cho et al. (2001), Hong et al. (2017), Cho et al. (2008), and El-Jummah et al. (2016), whereas the present study includes both an external, effusion cooled surface and the internal, impingement and cross flow cooled surface. Within the investigation of Cho et al (2001), effusion plate thickness is 2.0 effusion hole diameters, and impingement plate thickness is 1.33 effusion hole diameters. Here, the effusion plate and the impingement plate both have a thickness of 3.0 effusion hole diameters, whereas many other studies, such as those from Andrews et al. (1988), (1992), and (1999), El-Jummah et al. (2016) and (2017), and Oguntade (2017) employ relatively thin, effusion plates. Staggered arrays of film cooling injection holes are investigated by Nguyen et al. (2012). According to this study, at least four rows of holes are necessary to form a coolant layer along the hot-side surface. Cho et al. (2008) consider effects of impingement/effusion cooling hole arrangements on local surface heat transfer characteristics. The investigations show that staggered hole arrangements and smaller hole sizes yield better performance. Shi et al. (2016) considers cooling effectiveness on the mainstream-side of a test plate, where streamwise and spanwise spacing of effusion and impingement holes are the same, such that one impingement hole is present for each effusion hole. Surveys of combustor liner cooling technology, and effusion cooling, as applied to combustor components, are provided by Rogers et al., (2016), Schulz (2001), and Krewinkel (2013). Krewinkel (2013) reports that hole spacing and hole inclination angle are primary factors which affect the film effectiveness.

1.3 Current Test Facility

The present study provides new data on the effects of combined impingement jet array and cross flow cooling for a main flow passage contraction ratio of 4. Included are comparisons with impingement only and cross flow only data from previous investigations. The current facility incorporates impingement cooling and cross flow film cooling a sparse array effusion plate. Three separate blowers are used to supply main flow, cross flow, and impingement flow. Impingement flow is supplied through an array of impingement jet holes to provide coolant to the surface of the test place at locations between effusion holes on the test plate. Cross flow is supplied adjacent to the effusion plate. The present study focuses only on the cold-side arrangement.

1.4 Organization of the Thesis

The thesis consists of 4 chapters, 2 appendices, and a reference list. Chapter 2 contains the experimental apparatus and procedures, including descriptions of the test facility, the main testing section, methods for calculating various flow parameters, cold-side testing procedures and measurement apparatus, and experimental uncertainty values. Chapter 3 describes the coolant-side results for four different experimental arrangements: (1) high mainstream Reynolds number/constant cross flow Reynolds number/varying impingement Reynolds number, (2) low mainstream Reynolds number/constant cross flow Reynolds number/varying impingement Reynolds number, (3) high mainstream Reynolds number/constant impingement Reynolds number/varying cross flow Reynolds number, and (4) low mainstream Reynolds number/constant impingement Reynolds number/varying cross flow Reynolds number. Data are provided for a range of blowing ratios and Reynolds numbers, which are compared with cold-side data for CR=4, with impingement cooling only, and with cross flow cooling only. Experimental conditions, including values of cross flow Reynolds numbers, impingement Reynolds numbers, and mainstream Reynolds numbers, are provided in Tables 1-4. A summary and conclusions are presented in Chapter 4. Appendix A presents a data file directory. Appendix B presents the software directory.

CHAPTER 2

EXPERIMENTAL APPARATUS AND PROCEDURES

2.1 Double Wall Cooling Test Facility

Details of the present facility are shown in Figures 3-13. As seen in Figure 3, the current facility consists of a mainstream channel, a cross flow channel, and an impingement channel. These three channels each employ a separate blower to supply separate air flows. The main flow channel supplies heated air on the hot side of the effusion test plate, while the cross flow and impingement channels supply the cooling air on the cold side of the effusion test plate. Arrangements of cross flow only, impingement only, or a combination of both are used for testing. A custom etched-foil heater in the test plate is used to simulate the heating effects on the cold side of the effusion plate.

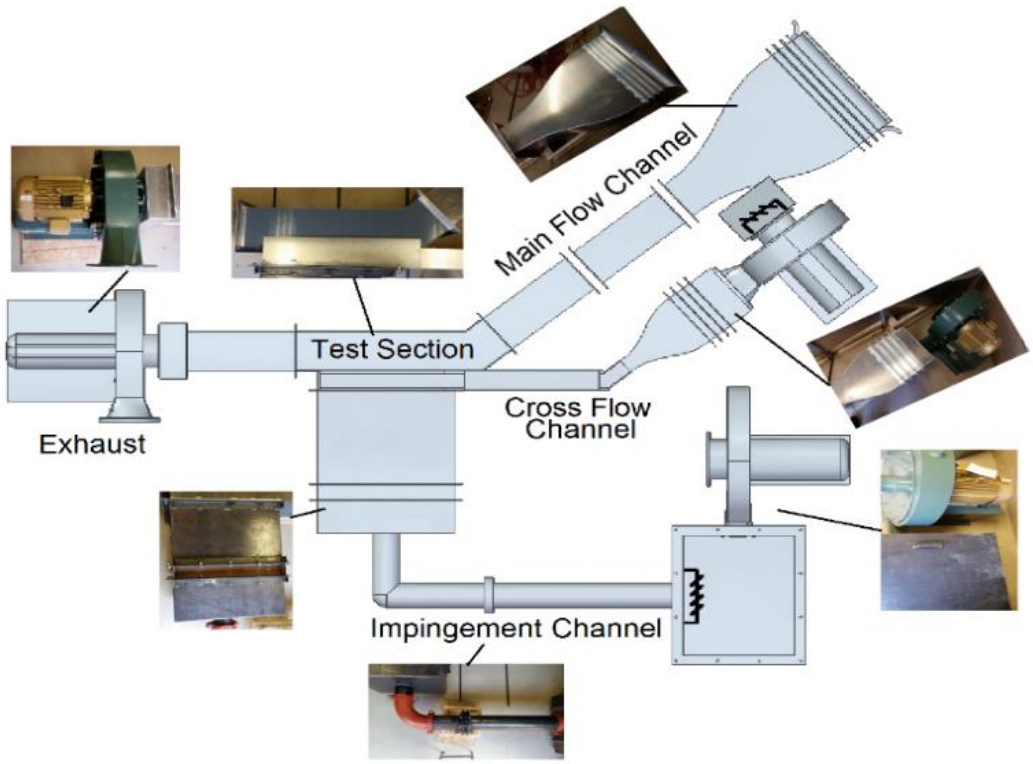

Figure 3. Experimental test facility layout.

An overview of the entire layout of the facility is presented in Figure 3 with photographs of different components. The intake to the main flow consists of a bell shaped inlet with honeycomb mesh followed by meshed screens for flow straightening, leading to a converging nozzle passage with a two-dimensional, fifth-order polynomial geometry. The nozzle is followed by a straight duct containing two separated Kanthol-D wire mesh heaters which supply step heating to the mainstream flow. These Kanthol-D wire mesh heaters are connected in series to an Ametek Sorensen SGA60/500D, 30-kilowatt DC power supply. Flow then passes into a duct with a 40-degree bend, which is the followed by the test section with a contraction area ratio of 4. The air then encounters a baffle in a transition duct before exiting through the blower, located at the exhaust. The main flow channel, aside from the blower and test section, is constructed using aluminum, while the test section is constructed with acrylic plastic. To ensure the Kanthol-D wire mesh heaters do not interact thermally or electrically with the facility, three 12 mm thick Teflon gaskets are used. Suction is used to induce air flow through the main flow passage by means of a New York Blower Co. 1708A pressure blower with a 15 HP 1800 RPM motor. All three blowers each have a separate Fuji Electric three phase variable frequency drive with ratings of 15 HP, 7.5 HP, and 15 HP, which correspond to the main flow blower, cross flow blower, and impingement blower, respectively. The blowers' settings are adjusted to match appropriate experimental flow conditions by changing the frequency of the variable frequency drives. Blower settings for each experimental condition are given in Tables 2-9.

The cross flow channel consists of an air passage from a heat exchanger connected to the inlet of a New York Blower Co. 1808S blower with a 7.5 HP 1800 RPM motor. The heat exchanger passes liquid nitrogen to cool the supply air. Air is then provided through a connected plenum and a two-dimensional, fifth-order polynomial geometry nozzle. The connected plenum contains a baffle followed by a honeycomb mesh and meshed screens for flow straightening. Downstream, air then passes to the cross flow portion of the test section. Aside from the blower and heat exchanger, the cross flow channel is constructed using aluminum.

The impingement channel has two upstream plenums, with a pipe connecting them. The first upstream plenum is connected to a New York Blower Co. 2404A pressure blower with a 15 HP 1800 RPM motor. The inlet of this blower is also connected to an air passage from the heat exchanger just mentioned. The outlet of this blower is connected to the first upstream plenum, which contains a second heat exchanger inside. This heat exchanger also employs liquid nitrogen

for cooling the impingement flow air supply. The second upstream plenum contains a baffle followed by honeycomb mesh and meshed screens for flow straightening purposes. The plenum also contains a Chameleon3 CM3-U3-13Y3C 1.3 MP Color USB3 VISION, with ON Semi PYTHON 1300 sensor and a 4.5 mm EO Megapixel Fixed Focal Length Lens for viewing the liquid crystal arrangement on the cold-side of the test plate. The impingement channel is constructed of steel and is sealed using gaskets. There is also an ASME standard orifice plate located in the pipe between the two plenums for air mass flow rate measurements.

2.2 Test Section, Effusion Test Plate, Impingement Test Plate

Inside the test section is the effusion test plate that separates the mainstream flow from the cross flow and impingement flow. The test section is used with two different arrangements: one with a contraction ratio of CR=1 and one with contraction ratio of CR=4. In the present study, CR=4 is used to create a pressure gradient in the main stream flow, along the hot side of the test plate. The film cooling test plate and impingement plate are installed and sealed using GE All Purpose Silicone 1. All seals are thoroughly tested for air leaks using a gas leak detecting spray. All of the air on the cold-side of the test plate enters through the effusion holes. For the combination of cross flow and impingement tests, testing is undertaken to avoid inappropriate back flow through the channels, from either cross flow or impingement flow.

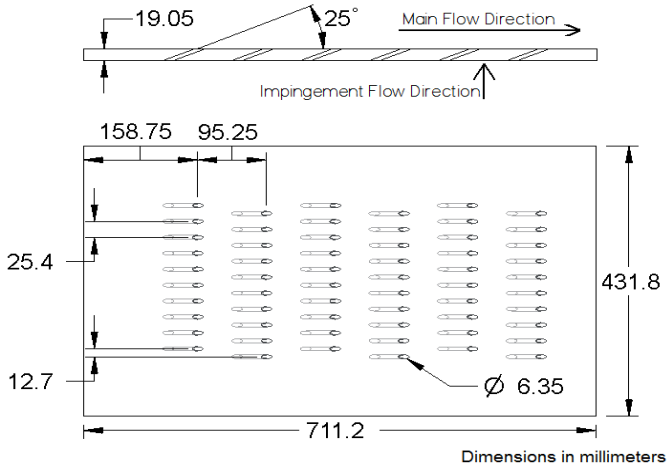

Figure 4. Film cooling test plate.

Figure 4 shows the film cooling test plate with its effusion hole locations and dimensions. These holes intake air from the impingement flow and cross flow, and deposit it along the surface of test plate on the main flow side. The effusion test plate contains 60 effusion holes, angled at 25 degrees, in 6 rows containing staggered rows with 10 effusion holes each. The offset of the rows is 12.7 mm, while the rows are separated by 95.25 mm and the holes in a row are 25.4 mm apart. Non-dimensional streamwise and spanwise hole spacings, x/d_e and y/d_e, are 15 and 4, respectively, where d_e is the effusion hole diameter of 6.35 mm. The film cooling test plate is constructed with a 1.5 mm polystyrene sheet on the top and bottom of the plate, a 16 mm PVC core, and a film heater located under the polystyrene sheet on the coolant side (cold-side), giving a total plate thickness of about 19.05 mm. The plate extends 431.8 mm in the spanwise direction and 711.2 mm in the streamwise direction.

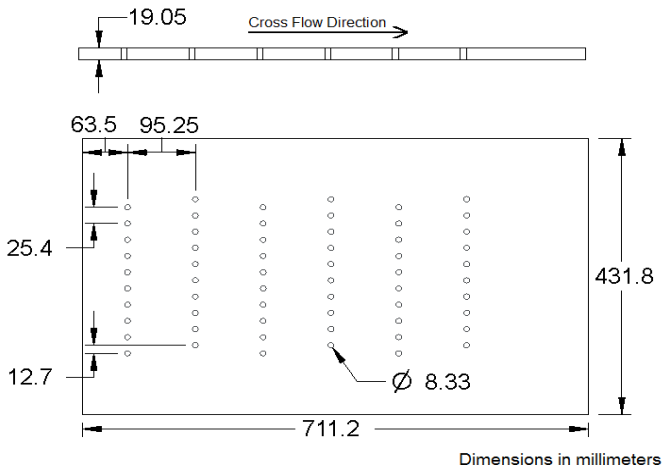

Figure 5. Impingement test plate.

The impingement plate, seen in Figure 5, contains 60 holes that are arranged into 6 rows with offset rows containing 10 holes each, similar to the film cooling test plate. However, these holes are not angled. Hole diameter is 8.33 mm, with the first row of holes located 63.5 mm from the leading edge of the plate. This arrangement locates the impingement holes between the effusion hole entrances. The impingement plate is 19 mm thick and constructed out of optically-transparent acrylic so that the Chameleon3 CM3-U3-13Y3C 1.3 MP Color USB3 VISION, with ON Semi PYTHON 1300 sensor and a 4.5 mm EO Megapixel Fixed Focal Length Lens, can view the cold side of the film cooling test plate, from its location within the impingement

plenum. Figure 6 shows relative positions of the impingement plate holes and the effusion plate entrance and exit holes. As mentioned, the impingement holes are located between effusion hole inlet locations. The impingement holes are thus aligned with the outlet locations of the effusion holes.

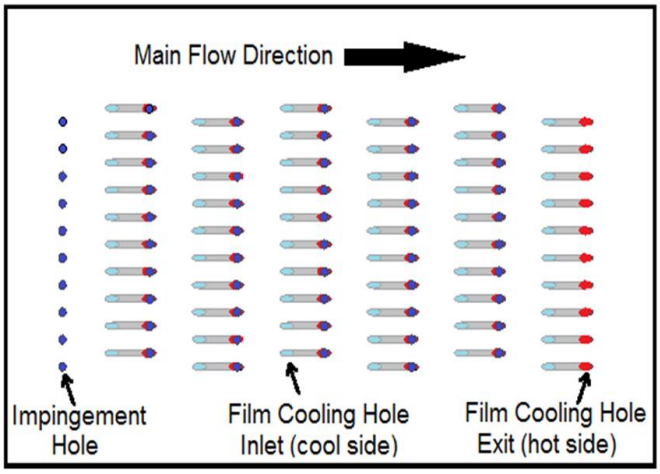

Figure 6. Film cooling and impingement test plates with effusion and impingement hole locations.

2.3 Temperature and Pressure Measurements

A variety of thermocouples and pressure taps are used. In the mainstream, as shown in Figure 7, one Kiel probe and five static pressure taps are used. Static pressure taps are made by drilling a 0.397 mm hole in the facility wall. Then, a threaded 6.35mm hole is drilled 3.175mm in the wall. A 6.35 mm metal tube is then connected to the threaded hole in the facility wall. A 6.35 mm inner diameter tubing is attached to the metal tube, as shown in Figure 11. The tubing sends static pressure signals to an array of Validyne DP15 differential pressure transducers, which are connected to Validyne CD15 Carrier Demodulators. United Sensor Corporation KCC-8 Kiel probes are employed as they are aligned with the flow streams in the center of each flow channel to measure local flow stagnation pressure. The Kiel probes are connected to the pressure transducers using a 3.18 mm inner diameter tubing. The pressure transducers also include a 100-microfarad capacitor across their carrier demodulator's output terminals to reduce extraneous noise effects. Note that the transducers have varying internal diaphragms, depending on the sensitivity needs of a particular pressure transducer. Data are recorded using LabVIEW 2017 Professional Development System version 17.0 software from National Instruments at a rate of 2

Hz, by use of National Instruments NI USB-6210 data acquisition card. Pressure and temperature tap measurement locations are seen in Figure 12. The Kiel probe and first static pressure tap are located at the upstream part of the test section, while four additional static pressure taps are located along the test section. In the cross flow channel part of the test section, one Kiel probe and five static pressure taps are used, shown in Figure 8. The Kiel probe and one static pressure tap are located in the upstream part of the cross flow channel. Figure 10 gives the instrumentation in the impingement supply channel. Here, five static pressure taps are present, with five thermocouples located at mirrored points on the other side of the impingement plenum. Shown in Figure 9, one Kiel probe and one static pressure tap are located upstream of the ASME standard orifice plate, within the pipe connecting the first upstream plenum and second upstream plenum. Two static pressure taps are located across the ASME standard orifice plate in the connecting pipe. The ASME standard orifice plate is positioned in a pipe between the two upstream impingement plenums. Five static pressure taps are located in the second upstream impingement plenum. Overall, a total of 21 pressure taps available for surface static pressure measurements.

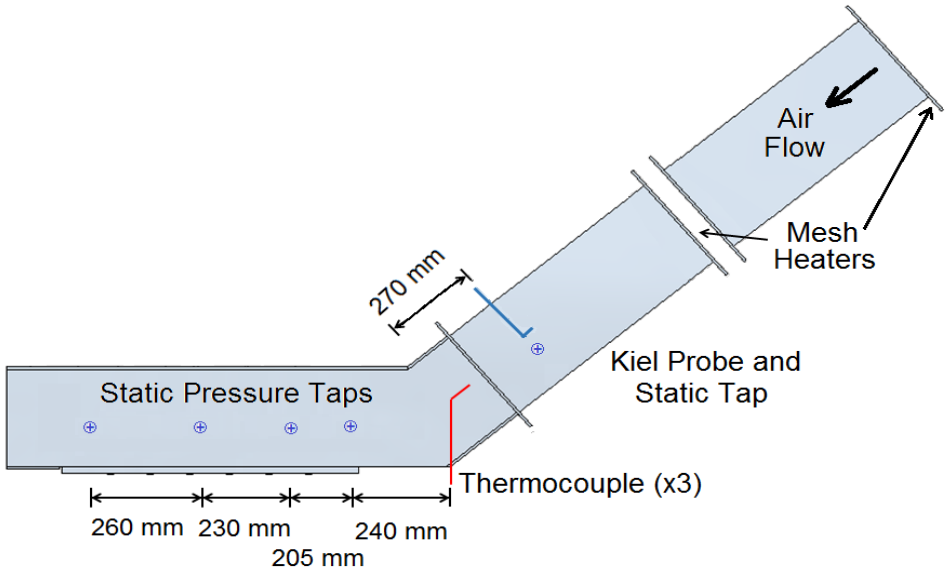

Figure 7. Instrumentation for mainstream flow channel.

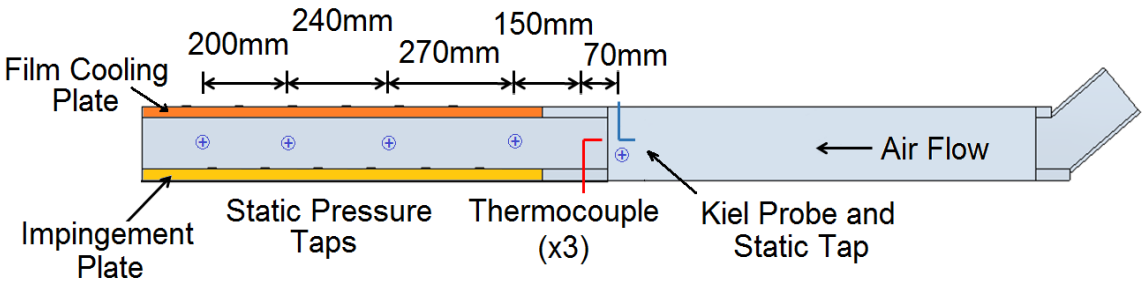

Figure 8. Instrumentation for cross flow supply channel.

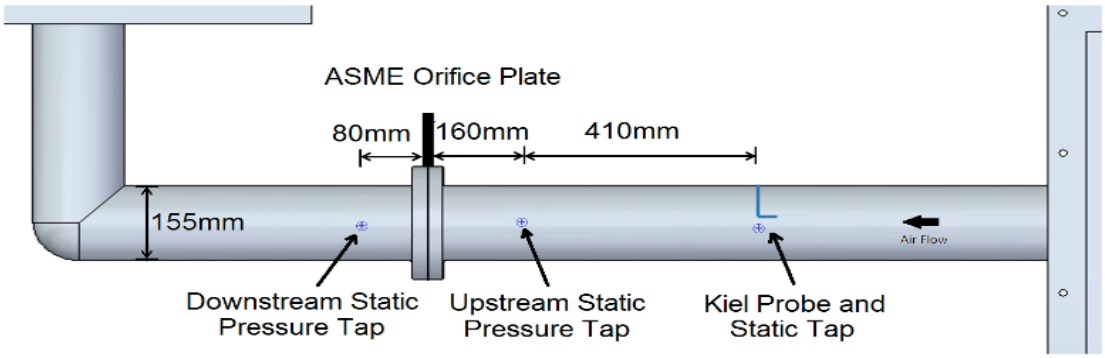

Figure 9. Instrumentation for impingement supply channel.

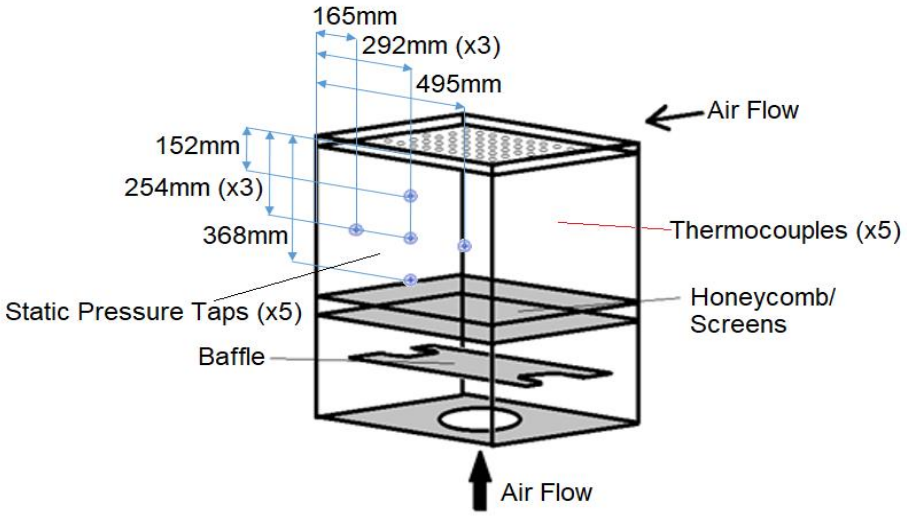

Figure 10. Instrumentation for second upstream supply plenum.

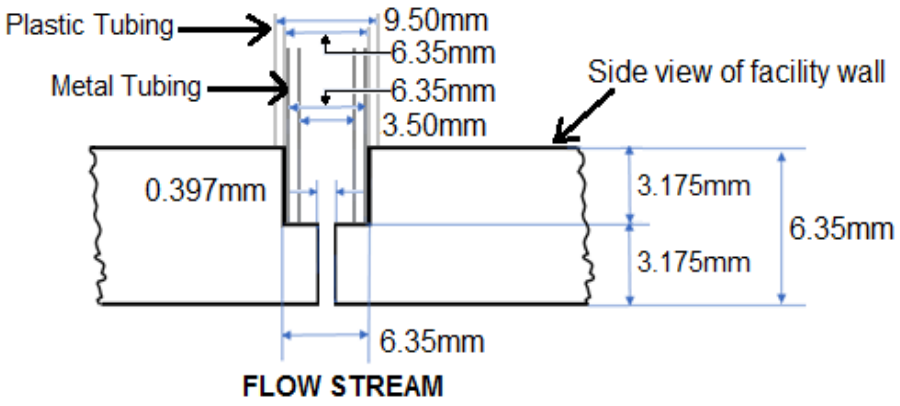

Figure 11. Static pressure tap and tubing diagram.

A diagram of the static pressure tap and tubing is shown in Figure 11. Five pressure taps are located along the main flow test section to quantify the static pressure gradient along the test section. Five additional pressure taps are also located along the cross flow passage for the same purpose. In regard to the cross flow passage on the cold-side of the test plate, stagnation pressure is approximately equal to the static pressure, since the cross flow channel is closed at the end and since local flow velocities are generally very small. This pressure is also approximately invariant along the length of the cross flow channel. Because static pressure varies along the main flow channel, a sixth-order polynomial equation is used to obtain the static pressure at the center of the exit of each row of effusion holes. The difference between the inlet stagnation pressure, $P_{t,e}$, measured within the cross flow channel, and the static pressure at the outlet of an effusion hole, $P_{s,e}$, measured within the main flow passage, gives the local effusion hole dynamic pressure $\Delta P_{e,}$. ΔP_e is then used for isentropic velocity determination.

Pressure transducer calibrations use a Meriam M100 Digital Manometer as a reference. To accomplish the calibration, a syringe is attached by a tee to the manometer and a pressure transducer. A range of pressures are applied to the syringe. As pressure is applied, pressure readings from the pressure transducer are recorded in LabVIEW 2017 Professional Development System version 17.0 software from National Instruments. Readings from the manometer are recorded in Microsoft Excel 2016 MSO version 16.0 software by hand. The variation of pressure transducer readings and manometer pressure readings are employed in Microsoft Excel 2016 MSO version 16.0 software. Calibration curves for each plot are then input to LabVIEW 2017 Professional Development System version 17.0 software from National Instruments to

characterize pressure variations for individual transducers. Before each test, the intercepts for the pressure transducers are adjusted to zero the devices.

Six thermocouples, embedded in the polystyrene on the cold-side of the effusion test plate, are shown in Figure 13. The four thermocouples located halfway down the span of the plate are used for data analysis. These are located at x and y locations of (161,218), (161,230), (368, 223), and (368, 234) with units in mm. Three thermocouples are located just before the test section in the main flow for air flow recovery temperature measurements. Similarly, three other thermocouples are located just before the test section in the cross flow channel for air flow recovery temperature measurements. A total of two thermocouples are located on the left and ride side of the impingement supply plenum. All thermocouples are Omega 5TC-TT-T-40-72 fine-wire copper constantan (Type T) thermocouples. The thermocouple data are recorded using LabVIEW 2017 Professional Development System version 17.0 software from National Instruments at 2.0 Hz using two National Instruments NI 9213 thermocouple input cards connected in a Nation Instruments NI cDAQ-9188 chassis. Non-embedded thermocouples are placed so that thermocouple wires are parallel to the flow direction. These thermocouples have a wire diameter of 0.08 mm. When mounted within a flow stream, each thermocouple is supported by a metal rod so that thermocouple position does not vary. The recovery factor of the thermocouples is 0.86, and the response time is 0.03s, according to calibration data provided by Omega Engineering. Analysis from Ren (2018) gives the response time to be approximately 0.023s.

Thermocouple calibrations use a Fluke Hart Scientific Division 1523 Reference Thermometer as a temperature reference. An Omega Thermoregulator HCTB-3030 Constant Temperature Liquid Circulating Bath, filled with distilled water, is used to maintain a constant temperature environment for calibration. Thermocouples, along with the thermometer, are inserted into the bath at the same level, away from the walls of the bath. Temperature readings for the thermocouples are then recorded in LabVIEW 2017 Professional Development System version 17.0 software from National Instruments. Readings from the thermometer are input into Microsoft Excel 2016 MSO version 16.0 software by hand. Variations of thermocouple voltage and thermometer readings are then processed using Microsoft Excel 2016 MSO version 16.0 software. Calibration data for each thermocouple calibration are then input to LabVIEW 2017

Professional Development System version 17.0 software from National Instruments to characterize the thermocouple temperature variations.

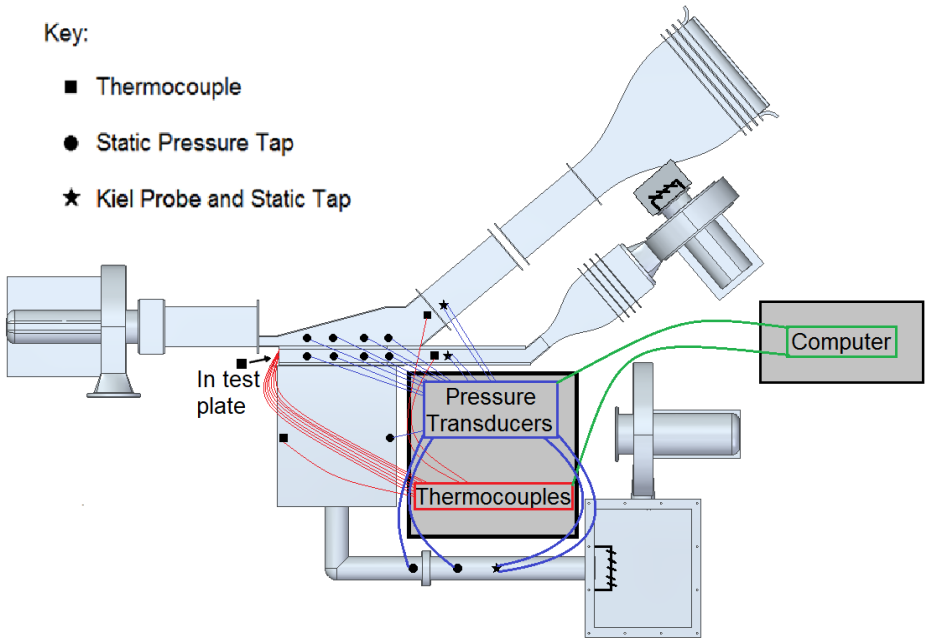

Figure 12. Experimental test facility, with temperature and pressure measurement locations.

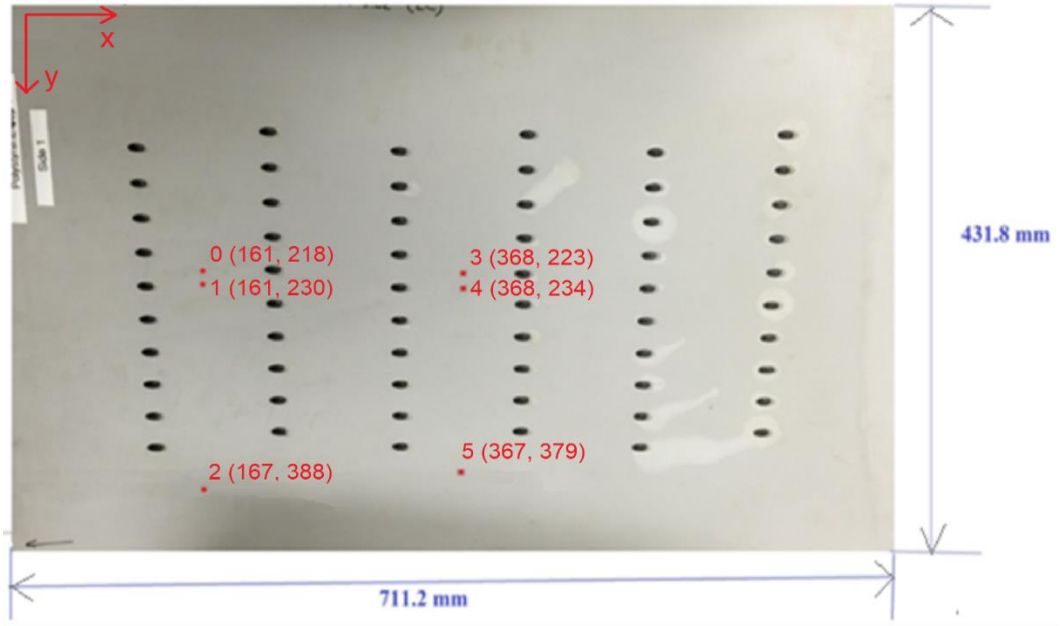

Figure 13. Locations of the six embedded thermocouples inside the polystyrene effusion test plate on the coolant side.

2.4 Impingement Flow Conditions Determination

The mass flow rate of the impingement air is determined from measurements of pressures and temperatures, relative to the ASME standard orifice plate in the connecting pipe between the first and second upstream plenums. The equations for these calculations are given by

$$\dot{m}_{or} = \dot{m}_i = KA_{pipe}\sqrt{2\rho_{s,i,pipe}\Delta P_{i,pipe}} \tag{1}$$

$$\rho_{s,i,pipe} = \frac{P_{s,i,pipe}}{RT_{s,i}} \tag{2}$$

$$V_{i,pipe,Avg} = \frac{\dot{m}_{or}}{\rho_{s,i,pipe}A_{pipe}} \tag{3}$$

The pipe centerline velocity, upstream of the orifice plate, is determined using

$$V_{i,pipe,CL} = \sqrt{\frac{2\Delta P_{i,pipe}}{\rho_{s,i,pipe}}} \tag{4}$$

where

$$\Delta P_{i,pipe} = P_{t,pipe} - P_{s,pipe} \tag{5}$$

Equations (1)–(3) are solved in an iterative fashion to obtain the values, K, $\rho_{s,i,pipe}$, $V_{i,pipe,Avg}$, and $\dot{m}_{or}$. Since no thermocouple is located in the pipe, the thermocouple in the second upstream impingement plenum is employed for pipe calculations to determine $\rho_{s,i,pipe}$. $V_{i,pipe,CL}$ is the velocity at the center line of the pipe, calculated using $\Delta P_{i,pipe}$. $\Delta P_{i,pipe}$ is then the difference in the total Kiel probe pressure and the local static pressure in the pipe. Values of $V_{pipe,CL}$ are 30 to 40 percent larger than values of $V_{i,pipe,Avg}$, which is used as a check of mass flow rate determination. The flow coefficient within Equation (1) is initially assumed to be equal to K=0.62. The value of K is then iteratively calculated using ASME orifice plate data, as dependent upon Reynolds number with length scale equal to the pipe diameter. In most cases, the resulting value of the flow coefficient is generally approximately equal to K=0.62. Two static pressure taps, located 1 diameter upstream and ½ diameter downstream of the ASME standard

orifice plate, along with a Kiel probe located 410 mm upstream, are used to measure associated stagnation and static pressures.

Since the impingement plenum cross sectional area is much larger than the area of the impingement test plate holes, the air in the impingement plenum is nearly stagnate. As a result, plenum thermocouples and wall static pressure taps provide impingement stagnation temperature, and impingement stagnation pressure, $T_{t,i}$ and $P_{t,i}$.

The impingement jet spatially-averaged velocity for an individual impingement jet hole exit is determined using the equation given by

$$V_i = \frac{\dot{m}_i}{\rho_{s,i} N_i A_i} \tag{6}$$

$T_{s,i}$ is then the impingement air static temperature spatially-averaged over the hole exit planes, as expressed using

$$T_{s,i} = T_{t,i} - \frac{{V_i}^2}{2c} \tag{7}$$

Impingement flow static density is then given by

$$\rho_{s,i} = \frac{P_{s,i}}{R T_{s,i}} \tag{8}$$

Here, $P_{s,i}$ is measured near the exits of the impingement holes within the cross flow channel. Note that $P_{s,i}$ does not vary significantly along the cross flow passage. As mentioned, because of the low air velocity with the impingement supply plenum, $P_{t,i}$ and $T_{t,i}$ are determined using a static pressure tap and a thermocouple, located along the wall and within impingement supply plenum, seen in Figure 10. Equations (6), (7), and (8) are solved in an iterative fashion to obtain values for $T_{s,i}$, $\rho_{s,i}$, and V_i. Knowing $T_{s,i}$, the absolute viscosity of the air is determined using Sutherland's formula which is expressed using

$$\mu_i = \mu_0 \frac{T_0 + C}{T_{s,i} + C} \left(\frac{T_{s,i}}{T_0} \right)^{3/2} \tag{9}$$

where C=120, T_0=291.15 K, and μ_0=1.827E-5 Pa-s.

Spatially-averaged magnitudes of discharge coefficient, Reynolds number, and Mach number associated with the impingement flow are then determined using

$$C_{d,i,Avg} = \frac{\rho_{s,i} V_i}{\sqrt{2\rho_{s,i}(\Delta P_i)}} \tag{10}$$

$$Re_{i,Avg} = \frac{\rho_{s,i} V_i d_i}{\mu_i} \tag{11}$$

$$M_{i,Avg} = \frac{V_{i,}}{\sqrt{\gamma R T_{s,i}}} \tag{12}$$

Here, ΔP_i is the difference between $P_{t,i}$ and the local static pressure in the cross flow passage, $P_{s,cf}$= $P_{s,i}$, into which impingement jets discharge.

2.5 Cross Flow Conditions Determination

Cross flow static temperature is determined using the equation given by

$$T_{s,cf} = T_{r,cf} - \alpha\left(\frac{{V_{cf}}^2}{2c}\right) \tag{13}$$

Here, $T_{r,cf}$ is the recovery temperature of the cross flow, measured using a thermocouple located near the entrance of the cross flow supply channel. The thermocouple wire is parallel to the flow direction and is mounted on a thin metal rod so that thermocouple position does not vary. With this arrangement, recovery factor α for the thermocouple equals 0.86. The cross flow air stagnation temperature is determined using

$$T_{t,cf} = T_{s,cf} + \frac{{V_{cf}}^2}{2c} \tag{14}$$

Cross flow static density is given by

$$\rho_{s,cf} = \frac{P_{s,cf}}{RT_{s,cf}} \tag{15}$$

Within Equation (15), $P_{s,cf}$ is measured using wall static pressure taps, located near the entrance of the cross flow supply channel. Spatially-averaged cross flow inlet supply velocity is then determined using

$$V_{cf} = \sqrt{2\Delta P_{cf}/\rho_{s,cf}} \tag{16}$$

where

$$\Delta P_{cf} = P_{t,cf} - P_{s,cf} \tag{17}$$

Equations (13)–(17) are solved in an iterative fashion to obtain the values of $T_{s,cf}$, $\rho_{s,cf}$, and V_{cf}. Within Equation (17), $P_{t,cf}$ is measured by a total Kiel probe near the entrance of the cross flow supply channel. The resulting cross flow entrance mass flow rate then equals

$$\dot{m}_{cf} = \rho_{s,cf} A_{cf} V_{cf} \tag{18}$$

The associated Reynolds number is then given by

$$Re_{cf} = \frac{\rho_{s,cf} V_{cf} DH_{cf}}{\mu_{cf}} \tag{19}$$

where

$$\mu_{cf} = \mu_0 \frac{T_0 + C}{T_{s,cf} + C} \left(\frac{T_{s,cf}}{T_0}\right)^{3/2} \tag{20}$$

where C=120 K, T_0=291.15 K, and μ_0=1.827 x 10^{-5} Pa-s. Within these equations, A_{cf} is the cross-sectional area of the cross flow channel.

2.6 Film Cooling Flow and Main Flow Conditions and Parameters Determination

The overall mass flow rate of the effusion coolant is the sum of the cross flow mass flow rate and impingement mass flow rate, as given by

$$\dot{m}_e = \dot{m}_{cf} + \dot{m}_i \tag{21}$$

The stagnation temperature for the effusion coolant is determined as a mass weighted average of cross flow stagnation temperature and impingement flow stagnation temperature, as expressed using

$$T_{t,e} = \frac{T_{t,cf}\dot{m}_{cf} + T_{t,i}\dot{m}_i}{\dot{m}_e} \tag{22}$$

The local static density, $\rho_{s,e}$ and spatially-averaged static density $\rho_{s,e,Avg}$ are determined with the following ideal gas equations. Note that the initial values of $T_{s,e}$ and $T_{s,e,Avg}$ are assumed to be $T_{t,e}$ for the iterative solution determination.

$$\rho_{s,e,Avg} = \frac{P_{s,e,Avg}}{RT_{s,e},Avg} \tag{23}$$

$$\rho_{s,e} = \frac{P_{s,e}}{RT_{s,e}} \tag{24}$$

Here, $P_{s,e}$ is the effusion hole exit static pressure, which is determined near the exit of each effusion hole row using a sixth-order polynomial equation from main stream static pressure measurements along the main flow channel. To determine $\rho_{s,e,Avg}$ using Equation (23), average values of $T_{s,e,Avg}$, and $P_{s,e,Avg}$ are employed. Average values of effusion flow parameters are determined from measured values near the exits of all effusion hole rows. The average effusion static temperature, local effusion static temperature, and average effusion velocity are then determined using

$$V_{e,Avg} = \frac{\dot{m}_e}{\rho_{s,e,Avg}A_eN_e} \tag{25}$$

$$T_{s,e,Avg} = T_{t,e} - \frac{V_{e,Avg}^2}{2c} \tag{26}$$

and

$$T_{s,e} = T_{t,e} - \frac{V_e^2}{2c} \tag{27}$$

respectively. An iterative solution is employed to determine values for $V_{e,Avg}$, $T_{s,e,Avg}$, and $\rho_{s,e,Avg}$ that satisfy Equations (23), (25), and (27). When repeated static temperature values are the same within a 1.0% error, then the iteration is complete. These iterations are made using Microsoft Excel 2016 MSO Version 16.0 software through its solver function. Because $T_{s,e,Avg}$ is then known, μ_e is then given by

$$\mu_e = \mu_0 \frac{T_0 + C}{T_{s,e,Avg} + C} \left(\frac{T_{s,e,Avg}}{T_0} \right)^{3/2} \tag{28}$$

where C=120 K, T_0=291.15 K, and μ_0=1.827 x 10^{-5} Pa-s.

Spatially-averaged values for the entire effusion hole array are determined next. First, the spatially-averaged effusion Reynolds number and Mach number are given as

$$Re_e = \frac{\rho_{s,e,Avg} V_{e,Avg} d_e}{\mu_e} \tag{29}$$

and

$$M_{e,Avg} = \frac{V_{e,Avg}}{\sqrt{\gamma R T_{s,e,Avg}}} \tag{30}$$

respectively. A spatially-averaged discharge coefficient is then determined using an equation of the form

$$C_{d,e,Avg} = \frac{\rho_{s,e,Avg} V_{e,Avg}}{(\rho_{s,e,Avg} V_{e,Avg})_{ideal}} = \frac{\rho_{s,e,Avg} V_{e,Avg}}{\sqrt{2 \rho_{s,e,Avg} (\Delta P_{e,Avg})}} \tag{31}$$

Within Equation (31), ΔP_e is difference between the inlet stagnation pressure, $P_{t,e}$, measured within the cross flow channel, and the static pressure at the exit of each effusion hole row, $P_{s,e}$, measured within the main flow passage. Values of ΔP_e at each effusion hole exit are then averaged to determine $\Delta P_{e,Avg}$.

Next, local effusion hole velocity, $V_{e,Local,}$ and the local mass flow rate at each effusion hole exit are determined using equations given by

$$\dot{m}_{e,Local} = C_{d,e,Avg} A_e \sqrt{2\rho_{s,e}\Delta P_e} \tag{32}$$

$$V_e = V_{e,Local} = \frac{\dot{m}_{e,Local}}{\rho_{s,e} A_e} \tag{33}$$

Here, $\rho_{s,e}$ is determined using Equation (24). Values of $\dot{m}_{e,Local}$ and $C_{d,e,Avg}$ are verified by comparing overall mass flow rate magnitudes for all effusion holes to values from Equation 21.

Local values of main flow, free stream conditions are determined next. First, freestream static temperature, freestream stagnation temperature, V_{ms}, and $\rho_{s,ms}$ are determined using an iterative solution. Associated equations are given as

$$T_{s,ms} = T_{s,ms,Local} = T_{r,ms} - \alpha\left(\frac{{V_{ms,Local}}^2}{2c}\right) \tag{34}$$

$$T_{t,ms} = T_{t,ms,Local} = T_{s,ms,Local} + \frac{{V_{ms,Local}}^2}{2c} \tag{35}$$

$$V_{ms} = V_{ms,Local} = \sqrt{\frac{2\Delta P_{ms,Local}}{\rho_{s,ms,Local}}} \tag{36}$$

and

$$\rho_{s,ms} = \rho_{s,ms,Local} = \frac{P_{s,ms,Local}}{R T_{s,ms,Local}} \tag{37}$$

where

$$\Delta P_{ms,Local} = P_{t,ms} - P_{s,ms,Local} \tag{38}$$

As such, $P_{t,ms}$ values are measured by total Kiel probe near the entrance of the main stream channel. $P_{s,ms,Local}$ is equal to $P_{s,e}$, which is calculated near the exit of each effusion hole row, using a sixth-order polynomial equation from main stream static pressure measurements along the main flow channel. μ_{ms} is then determined based upon the inlet values of $T_{s,ms,Local}$ as given by

$$\mu_{ms} = \mu_0 \frac{T_0 + C}{T_{s,ms,Local} + C} \left(\frac{T_{s,ms,Local}}{T_0} \right)^{3/2} \quad (39)$$

where C=120, T_0=291.15 K, and μ_0=1.827E-5 Pa-s. Here, local values given by Equations (32) – (38) are determined for the inlet of the main flow passage and near the exit of each effusion hole row.

$\Delta P_{ms,Avg}$ and $\rho_{s,ms,Avg}$ are determined as the average values of ΔP_{ms} and $\rho_{s,ms}$ across the main flow test section from measurements near the exit of the each effusion hole row. $V_{ms,Avg}$ is then given by

$$V_{ms,Avg} = \sqrt{\frac{2\Delta P_{ms,Avg}}{\rho_{s,ms,Avg}}} \quad (40)$$

Mainstream Reynolds numbers, $Re_{ms,Avg}$ and Re_{ms} are subsequently calculated using

$$Re_{ms,Avg} = \frac{\rho_{s,ms,Local} V_{ms,Avg} DH_{ms}}{\mu_{ms}} \quad (41)$$

$$Re_{ms} = \frac{\rho_{s,ms,Local} V_{ms,Local} DH_{ms}}{\mu_{ms}} \quad (42)$$

With this approach, $Re_{ms,Avg}$ is calculated based on the average variation of mean mainstream velocity through the main flow test section. Re_{ms} is calculated based on the inlet mean mainstream velocity within the main flow test section. $\rho_{s,ms,Local}$, DH_{ms}, and μ_{ms} within Equations (41) and (42) are determined based upon values at the inlet of the main stream test section.

The equation for local effusion hole exit blowing ratio is then given by

$$BR = BR_{e,Local} = \frac{\rho_{s,e} V_{e,Local}}{\rho_{s,ms,Local} V_{ms,Local}} \quad (43)$$

When $BR_{e,Local}$ is varying along the length of the test plate, values at the inlet of the test section are employed to characterize associated data. Effusion velocity ratio, density ratio, and

momentum flux ratio are also determined for the inlet of the test section. Associated equations are given by

$$VR = \frac{V_{e,Local}}{V_{ms,Local}} \tag{44}$$

$$DR = \frac{\rho_{s,e}}{\rho_{s,ms,Local}} \tag{45}$$

$$I = BR * VR \tag{46}$$

2.7 Measurement of Surface Heat Transfer Coefficient and Adiabatic Wall Temperature Distributions – Coolant Side of Effusion Plate

Liquid crystal thermography is used to measure spatially-resolved surface temperature distributions along the coolant side of the film cooling plate. Liquid crystals of type SPN100R25C5W from LOT#160419-709-SPN from LCRHallcrest Company are sprayed uniformly on the coolant side of the test plate in 10-12 coats over a SPB100 black backing paint of LOT#151202 (also from the LCRHallcrest Company). Further detailed explanation of the liquid crystal application process is given by Vanga (2016). These liquid crystals have an active range from 25^0C to 30^0C with a color spectrum from lower red hues to mid temperature green hues to blue hues at the highest temperatures. The camera used to record the hue values is a Chameleon3 CM3-U3-13Y3C. This camera is mounted inside the impingement plenum near the baffle in order to not disrupt the air flow to the impingement jets. Image RGB intensity values are processed and converted to hue angle values using a program called LiquiTherm Image Processor.bat created by Willard (2013). Within the cross flow passage are RibbonFlex Pro LED (Light Emitting Diode) lighting strip with 60 natural white color LEDs per meter (model #RF3528060 from Armacost Lighting). For proper image visualization by the camera inside the impingement plenum, the natural white LED lighting strip is used for uniform lighting free of reflection or shadowing. This lighting strip is glued to the outer sides of the impingement test plate, as seen in Figure 14. Note that the impingement plenum, with the camera inside, is positioned adjacent to the cross flow channel.

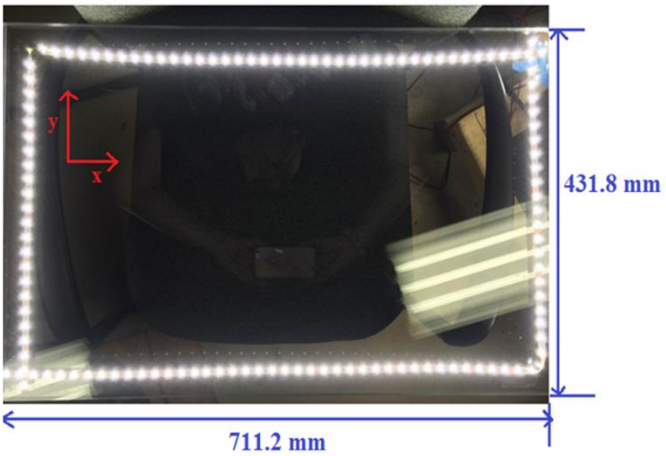

Figure 14. Natural white color LED lighting strip, model #RF3528060 from Armacost Lighting, taped to the clear acrylic plate of 711.2 mm by 431.8 mm dimensions. LED lighting strip is placed at approximately 76.2 mm from the target test plate.

Figure 15 shows the dimensions and layout of the Chameleon3 CM3-U3-13Y3C camera relative to the test section and facility. The camera is located 60.96 cm from the impingement plate and 70.48 cm from the film cooling test plate. For the current experiment, the camera is mounted on a thin metal strip in the impingement plenum. The camera is able to record in 149 frames per second, with a 1.3-million-pixel resolution. Each image is 1280-pixels by 1024-pixels, where each pixel has 8-bit resolution. The output of the camera is recorded using version 2.9.3.11 of FlyCapture Viewer Software (2016). Timed snapshots can be taken in conjunction with LabVIEW 2017 Professional Development System version 17.0 from National Instruments pressure and temperature measurements for calibration or data processing. A closer view of the camera, as located outside of the impingement plenum, is shown in Figure 16.

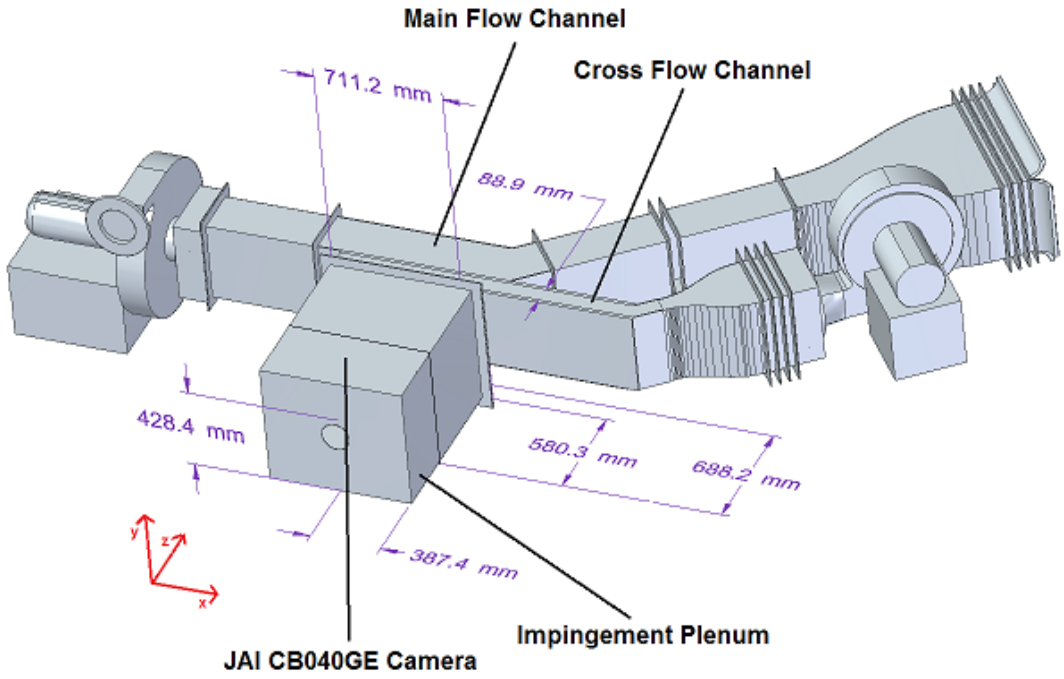

Figure 15. Layout of the experimental test facility indicating the Chameleon3 camera, effusion test plate and test section. The Chameleon3 CM3-U3-13Y3C camera is placed inside of the impingement plenum.

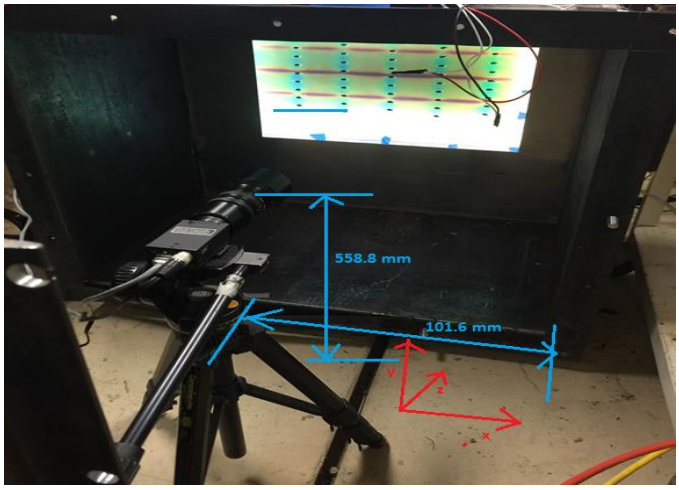

Figure 16. JAI CB040GE model camera with Navitar Zoom 7000 lens, mounted on a tripod. Shown are the JAI CB-040GE camera, placed outside the impingement plenum of the experimental test facility, and the effusion cooling test plate image, as seen from the clear acrylic plate placed between impingement plenum and crossflow channel.

The calibration of the liquid crystal is performed using a method described by Hay and Hollingsworth (1998). This arrangement is also described by Vanga (2016). The calibration uses the embedded thermocouple temperatures and corresponding hue values of the liquid crystals to develop a correlation between hue values and surface temperatures. The embedded thermo-foil film heater is used to vary the test plate temperature and the temperatures of the associated liquid crystal layer. The heater is controlled by BK PRECISION XLN10014 programmable direct current power supply which is capable of a power output to 1440 watts, 0-100 V and 14.4 Amps. This system comes with a 16-bit D/A, A/D converter embedded, with a power supply resolution of 1 mV for voltage setting and 1 mA for current. The voltage and amperage of the power are measured using two separate KEYSIGHT 34401A 6.5 digital multimeters. Both devices are used for current measurements, while one of the devices is used for voltage measurements. Amperage is verified using a Simpson 260 Series 8 analog ammeter. The calibration is performed by varying the current and voltage of the heater, as images of the test plate along with thermocouple temperature readings are recorded. These images are then converted into hue angle from their RGB values by the following equation developed by Hay and Hollingsworth (1998), as employed within the LiquiTherm Image Processor.bat file developed by Willard (2013).

$$h = arctan\left(\frac{\sqrt{3}(G-B)}{2R-G-B}\right) \tag{47}$$

within Equation (47), G is green, R is red, and B is blue. Additional calibration analysis details are provided by Vanga (2016).

For data acquisition, as measurements are acquired, the voltage and current are kept constant. For each experimental condition, five image captures are taken which are spaced 30 seconds apart. Resulting images are ensembled-averaged to obtain time-averaged data. The resulting hue angles from the LiquiTherm Image Processor program are then converted to temperature values using the equation which represents the associated liquid crystal calibration data. One liquid crystal calibration is presented in Figure 17. Here, gray circles represent the uncertainty in the temperature analysis, and the squares represent temperature variation with hue angle. The resulting sixth-order polynomial equation is then used to determine surface

temperature values for Nusselt number determination. An example of measurement area is shown in Figure 18. Note that the positions of embedded thermocouple locations, shown in Figure 13 are contained within the associated analysis region.

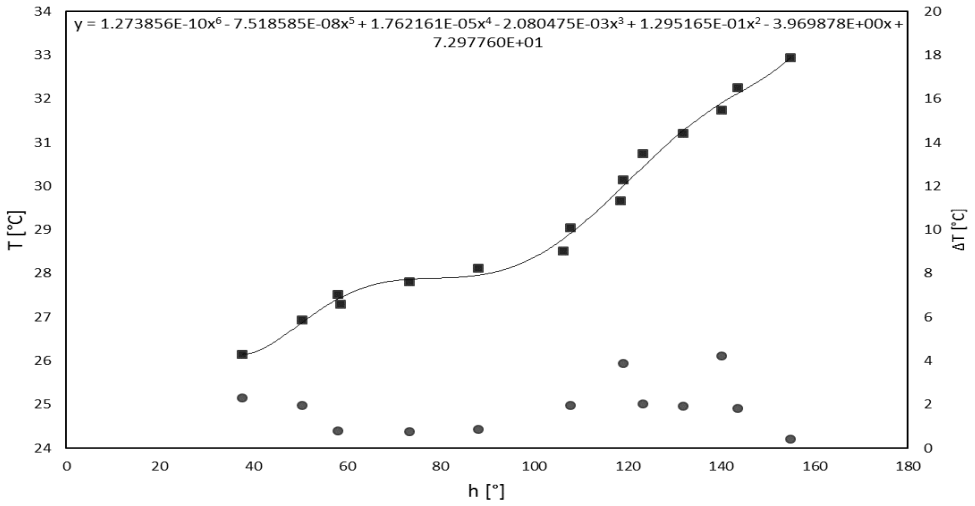

Figure 17. Variation of the temperature of the liquid crystals with hue angle. The temperature range is from 26^0C to 33^0C for the calibration test. A sixth order polynomial trendline is used to curve fit the plot. The ΔT shows uncertainty in the temperature analysis.

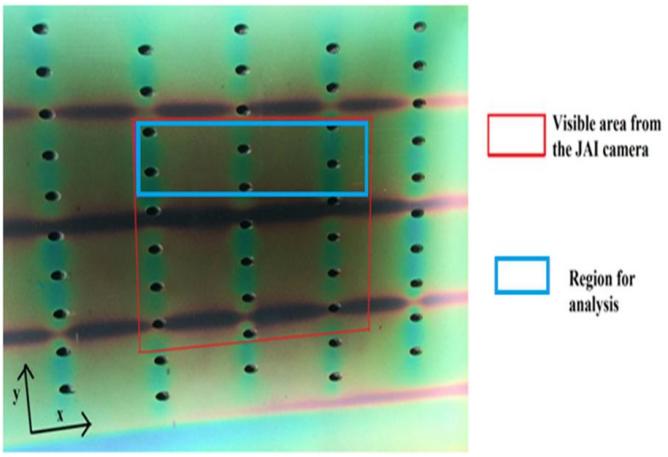

Figure 18. The blue box indicates an area of approximately 760 pixel by 164 pixel of the test plate image selected for analysis. The red box indicates the area of test plate seen from the Chameleon3 CM3-U3-13Y3C camera.

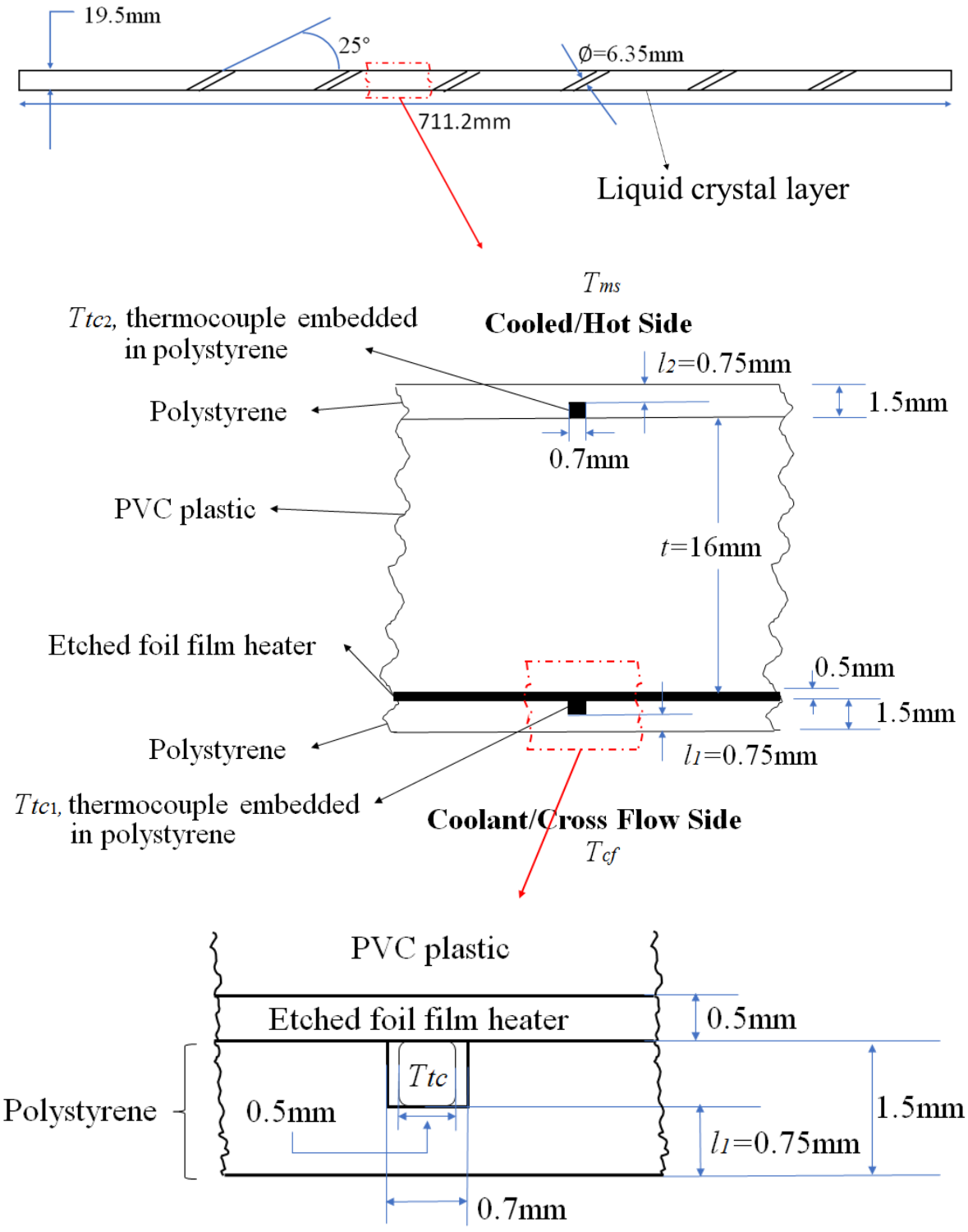

Figure 19. Dimensions and layout of different layers of the effusion test plate.

A cut-away side view of the test plate illustrating different component layers, film heater placement, and thermocouple junctions is given in Figure 19. The 1.5 mm polystyrene layers have a thermal conductivity of 0.22 W/mK. Loctite 1365736 heavy duty epoxy is used to seal the thermocouples in the test plate, since it has a similar thermal conductivity as the polystyrene. The thermal conductivity of the PVC core is that of PVC type 1 plastic with a value of 0.17 W/mK.

With surface temperatures measured using liquid crystal thermography, spatially-resolved surface Nusselt number are determined using the following analysis procedures. The power given to the heater by the power supply is calculated by

$$Q = P = VI \tag{48}$$

The power on the surface of the coolant side of the film cooling test plate is found from accounting for the conduction losses from the heat to through the polystyrene layer of the test plate as given by

$$Q_{crct} = Q - \frac{T_{tc1} - T_{ms}}{\frac{2l_2}{k_{pst} \cdot A_{ht}} + \frac{t}{k_{PVC} \cdot A_{ht}}} \tag{49}$$

where T_{ms} is used with the assumption of a uniform mainstream temperature in the main flow, and T_{tc1} is located on the cold-side of the effusion test plate (Figure 15). The liquid crystal surface temperature distribution is determined, using the liquid crystal calibration temperature T_{LC}, for the entire 760 by 164 pixel array of each image using

$$T_{w_{crct}} = T_{LC} - \frac{Q_{crct} \cdot l_1}{k_{pst} \cdot A_{ht}} \tag{50}$$

$T_{w_{crct}}$ temperature values are ensemble-averaged over five cases to obtain a time-averaged result. Next, the convective heat flux is determined using

$$q_{crct} = \frac{Q_{crct}}{A_{ht}} \tag{51}$$

Spatially resolved Nusselt numbers are then determined using an equation given by

$$Nu = \frac{q_{crct}.d_e}{k_{air}.(T_{w_{crct}} - T_{t,e})} \quad (52)$$

where $T_{t,e}$ is the stagnation temperature of the effusion coolant determined using Equation (22). Line-averaged Nusselt numbers are subsequently determined as the average of the local, spatially resolved Nusselt numbers at a constant streamwise x/d_e location over a range of spanwise y/d_e. The present arrangement uses a y/d_e range from 0 to 8. Spatially-averaged Nusselt number data are determined from averages of line-averaged Nusselt number values over x/d_e ranges from 0-15, 15 to 30, and 30 to 45. In all cases, surface locations of effusion hole inlets are not included as average values.

2.8 Experimental Uncertainty Magnitudes

According to Rogers et al. (2015), uncertainty estimates are based on 95 percent confidence levels, and determined using procedures described by Kline and McClintock (1953) and by Moffat (1988). Uncertainty of thermocouple temperature readings is $\pm$ 0.15 ^{o}C. This uncertainty is dependent upon the thermocouple calibration procedure. Pressure uncertainty is $\pm$ 0.25 Pa. This uncertainty is dependent upon the pressure transducer calibration procedure. The experimental uncertainty of the blowing ratio is $\pm$ 4.0 percent. The experimental uncertainty of the coolant mass flow rate is also approximately $\pm$ 4.0 percent, and is primarily due to uncertainty in local coolant velocity. This local coolant velocity value is a result of uncertainty in measured coolant pressure ratio ($\pm$ 0.8 percent) and uncertainty in the discharge coefficient ($\pm$ 3.4 percent). According to Vanga (2016), the uncertainty magnitude for the surface temperature of liquid crystals ranges from 0.42 to 4.2 degrees, for different magnitudes of surface heat flux, as shown by the data in Figure 17. Associated surface Nusselt number uncertainty ranges from 6 to 9 percent.

CHAPTER 3

COOLANT SIDE EXPERIMENTAL RESULTS

3.1 Introduction

This chapter gives experimental results for full-coverage effusion cooling on the coolant-side of a double-wall effusion plate. Presented are local, line-averaged and spatially-averaged Nusselt number data. Two ranges of mainstream Reynolds numbers, $Re_{ms,Avg}$, are used: 162,000 to 171,000 and 233,000 to 245,000. Experimental data are obtained as either Re_{imp} or Re_{cf}. is varied while the other is kept constant. This is done for both mainstream Reynolds numbers, giving a total of four test cases. A test section with an inlet area four times the exit area is employed. This contraction ratio of 4 creates a strong favorable pressure gradient as flow develops in the streamwise direction. The pressure gradient also causes local blowing ratio to vary with streamwise development.

3.2 Overall Experimental Test Conditions

Table 1. Reynolds number results for four different experimental arrangements.

	Re_{ms}	$Re_{ms,avg}$	Re_{cf}	Re_{imp}
CASE 1	157,201-161,193	233,00-244,000	8,180-9,060	2,410-5,120
CASE 2	102,709-107,029	164,000-171,000	5,736-5,950	1,643-3,255
CASE 3	158,601-162,338	236,000-245,000	8,914-16,655	2,678-2,723
CASE 4	99,305-102,398	162,000-168,000	6,550-12,240	1,542-1,596

Table 1 presents Reynolds number conditions for four experimental cases. Figure 20 shows the cross flow only and impingement only Reynolds number conditions for mainstream Reynolds numbers, $Re_{ms,Avg}$, of 233,000 to 245,000. Figure 21 shows the cross flow only and impingement only Reynolds number conditions for Reynolds numbers, $Re_{ms,Avg}$, of 162,000 to 171,000. Figure 22 gives impingement Reynolds number, Re_{imp}, and cross flow Reynolds number, Re_{cf}, values for the CASE 1 data. Figure 23 gives Re_{imp} and Re_{cf} values for the CASE 2 data. Figure 24 gives Re_{imp} and Re_{cf} values for the case 3 data. Figure 25 gives Re_{imp} and Re_{cf} values for the CASE 4 data.

Of interest are comparisons between heat transfer effects of the combined impingement and cross flow arrangement. Comparisons are made with impingement flow only and cross flow only data presented within Ren et al. (2018) and Ligrani et al. (2018).

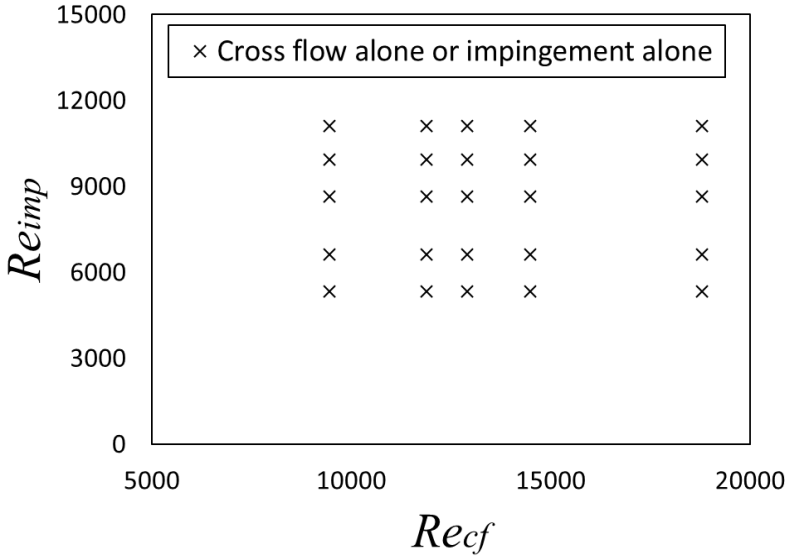

Figure 20. Cross flow only and impingement only experimental Reynolds numbers conditions for mainstream Reynolds numbers, $Re_{ms,Avg}$, of 233,000 to 245,000.

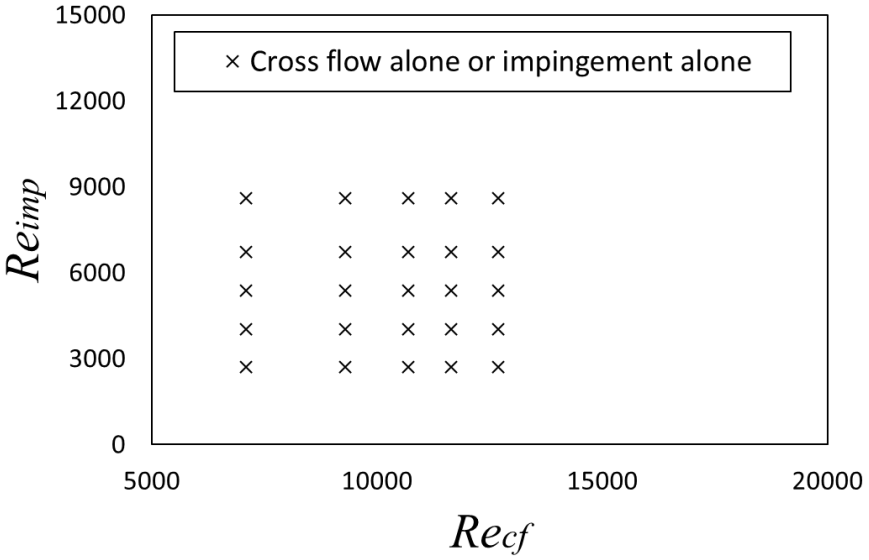

Figure 21. Cross flow only and impingement only experimental Reynolds numbers conditions for mainstream Reynolds numbers, $Re_{ms,Avg}$, of 162,000 to 171,000.

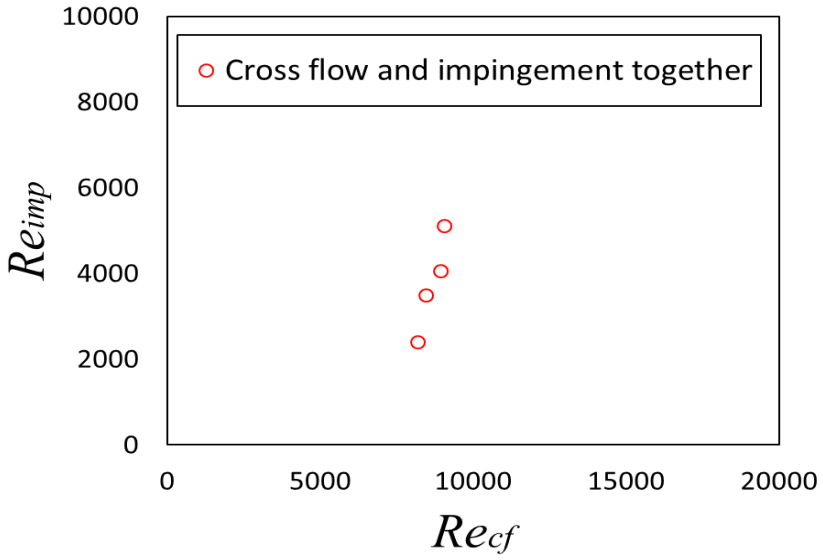

Figure 22. Combined impingement and cross flow Reynolds numbers for CASE 1 experimental conditions.

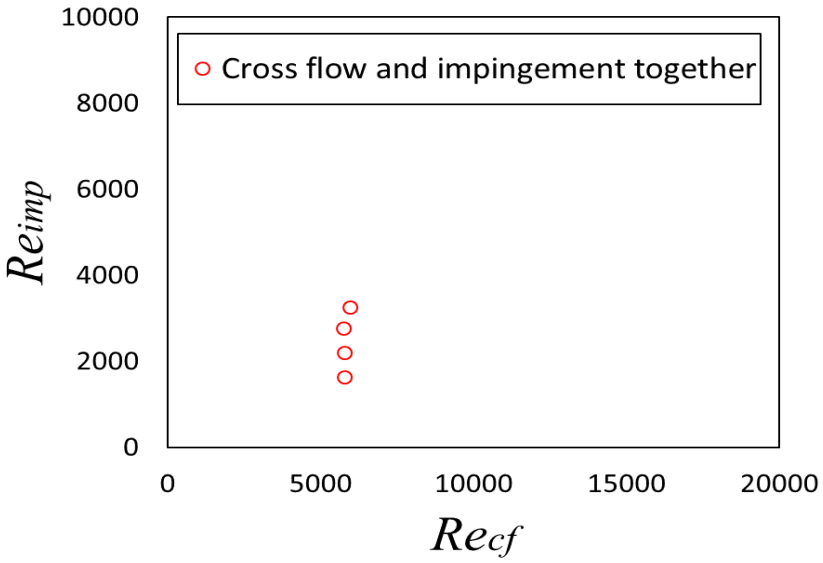

Figure 23. Combined impingement and cross flow Reynolds numbers for CASE 2 experimental conditions.

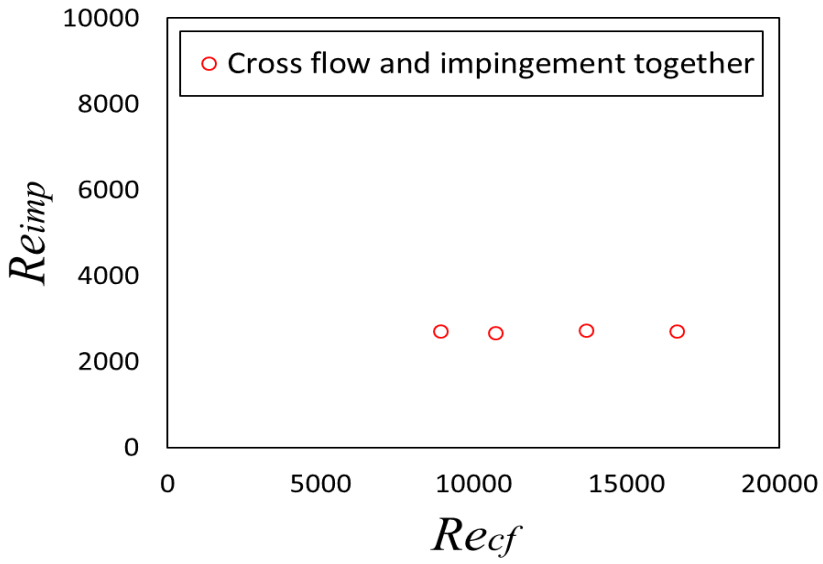

Figure 24. Combined impingement and cross flow Reynolds numbers for CASE 3 experimental conditions.

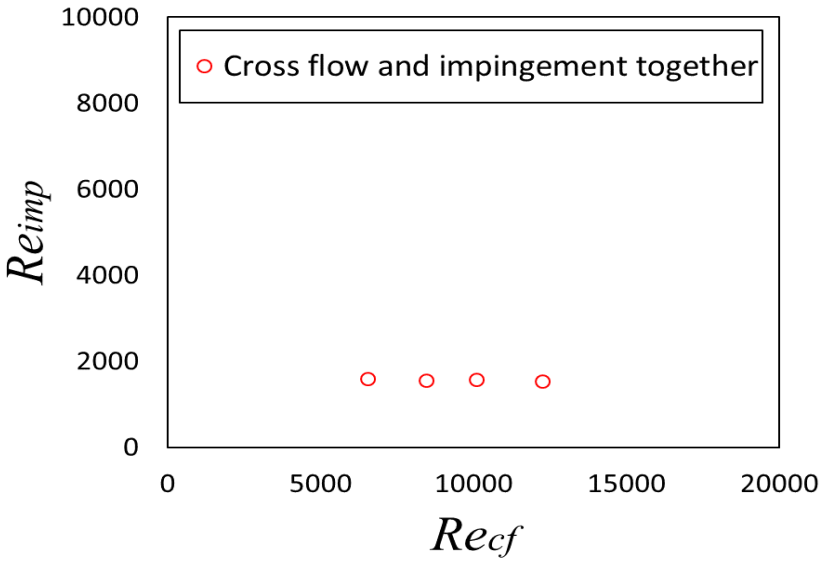

Figure 25. Combined impingement and cross flow Reynolds numbers for CASE 4 experimental conditions.

3.3 Experimental Data for Constant Re_{cf} and Varying Re_{imp} for Mainstream Reynolds Numbers $Re_{ms,Avg}$ of 233,000 to 240,000

3.3.1 Experimental Conditions for Constant Re_{cf} and Varying Re_{imp} for Mainstream Reynolds Numbers $Re_{ms,Avg}$ of 233,000 to 240,000

Table 2. Experimental conditions and blower settings for CASE 1 high mainstream Reynolds number/constant cross flow Reynolds number/varying impingement Reynolds number.

Experimental Conditions for Pressure Drop Measurements																				
Main Flow						Cross Flow				Impingement Flow				Effusion Flow						
	Blower Setting	V_{ms}	Mass Flow Rate	Re_{ms}	$Re_{ms,avg}$	Blower Setting	V_{cf}	Mass Flow Rate	Re_{cf}	Blower Setting	V_{imp}	Mass Flow Rate	Re_{imp}	V_{ef}	Mach Number	Re_{ef}	Density Ratio	Velocity Ratio	Momentum Flux Ratio	Blowing Ratio
Test	[Hz]	[m/s]	[kg/s]			[Hz]	[m/s]	[kg/s]		[Hz]	[m/s]	[kg/s]		[m/s]			DR	VR	I	BR
1	46	7.73	0.98	161193	243861	23	0.80	0.036	8180	20	4.36	0.024	2410	43.9	0.13	18800	1.0	5.9	34.88	5.9
2	46	7.67	0.97	159916	241633	27	0.83	0.037	8440	25	6.31	0.035	3490	50.8	0.15	21800	1.0	6.9	47.73	6.9
3	46	7.58	0.96	157980	237017	33	0.87	0.039	8920	30	7.37	0.041	4070	60.0	0.18	25800	1.0	8.3	68.92	8.3
4	46	7.54	0.96	157201	232515	39	0.93	0.042	9060	36	9.28	0.051	5120	69.5	0.20	30000	1.0	9.8	96.09	9.8

Table 3. Experimental heat transfer conditions and blower settings for CASE 1 high mainstream Reynolds number/constant cross flow Reynolds number/varying impingement Reynolds number.

Experimental Conditions for Heat Transfer Measurements																				
Main Flow						Cross Flow				Impingement Flow				Effusion Flow						
	Blower Setting	V_{ms}	Mass Flow Rate	Re_{ms}	$Re_{ms,avg}$	Blower Setting	V_{cf}	Mass Flow Rate	Re_{cf}	Blower Setting	V_{imp}	Mass Flow Rate	Re_{imp}	V_{ef}	Mach Number	Re_{ef}	Density Ratio	Velocity Ratio	Momentum Flux Ratio	Blowing Ratio
Test	[Hz]	[m/s]	[kg/s]			[Hz]	[m/s]	[kg/s]		[Hz]	[m/s]	[kg/s]		[m/s]			DR	VR	I	BR
1	46	8.03	0.985	161832	244389	22.8	0.89	0.040	9103	20	4.61	0.025	2547	42.5	0.13	18412	1.03	5.3	29.54	5.5
2	46	7.99	0.979	160702	241326	27.9	0.86	0.038	8769	25	6.25	0.034	3453	49.8	0.15	21470	1.04	6.3	41.26	6.5
3	46	7.92	0.971	159475	237551	33.5	0.86	0.039	8808	30	7.59	0.042	4190	58.1	0.17	25032	1.03	7.5	57.69	7.7
4	46	7.80	0.961	157752	232825	39.9	0.86	0.039	8800	36	9.52	0.052	5260	67.7	0.20	29217	1.03	8.9	81.13	9.1

Table 2 presents the experimental conditions for pressure drop measurements. Table 3 gives the experimental conditions for the heat transfer measurements. These values are taken for the CASE 1 configuration. Re_{ms} ranges from 157,201 to 161,193, $Re_{ms,Avg}$ ranges from 233,000 to 244,000, Re_{cf} ranges from 8,180 to 9,060, and Re_{imp} ranges from 2,410 to 5,120. For this case, Re_{cf} is kept constant while the Re_{imp} is varied. Included in the tables are blower settings, velocities, mass flow rates, and Reynolds numbers. These values are given for main flow, cross flow, impingement flow, and effusion flow. High Reynolds number cases are associated with a mainstream velocity of 7.5 to 8.0 m/s. Low Reynolds number cases are associated with a

mainstream velocity of about 5 m/s. Mainstream Reynolds numbers are determined using the average variation of mean mainstream velocity through the main flow test section and using main flow test section inlet mainstream flow velocity.

3.3.2 Local Line-averaged and Area-averaged Nu Variations with Initial Blowing Ratio

Time-averaged, spatially-resolved surface Nusselt number variations are shown in Figure 26. Figure 27 presents line-averaged Nusselt number data. Figure 28 presents area-averaged Nusselt numbers with varying x/d_e, for a combined impingement and cross flow arrangement. As Re_{imp} and initial blowing ratio increase while Re_{cf} is held constant, values of Nusselt numbers tend to increase, but with only small variation with Reynolds number. The amount of coolant distributed on the surface of the effusion test plate tends to decrease with streamwise development. Such trends are especially evident for surface Nusselt number variations in Figure 26 for the first three blowing ratios. Seen in Figure 26 for blowing ratio of 9.8, there is an increase in the amount of coolant build up for large x/d_e, along the effusion test plate. This increase is also seen in Figure 27, where the last peak of line-averaged Nusselt numbers is similar to the first in magnitude. This increase is due to a stronger presence of impingement flow at a higher Re_{imp}. The addition of cross flow inhibits cooling along the surface of the effusion test plate from the impingement flow. However, as initial blowing ratio and Re_{imp} increase while Re_{cf} is held constant, impingement flow begins to overpower the cross flow. This increases thermal protection along the surface of the effusion test plate, since negative effects from the cross flow are lessened on a relative basis.

3.3.3 Comparisons with CR=4 Impingement Only Data

Figure 29 shows line-averaged Nusselt number comparison plots with impingement only data. Figure 30 shows area-averaged Nusselt number comparison plots with impingement only data. Line-averaged and area-averaged Nusselt number data tends to vary less with increasing Reynolds number and initial blowing ratio, for the combination impingement/cross flow arrangement, compared to the impingement only configuration. Nusselt number data shows overall lower Nusselt numbers compared to impingement only data. This is due to cross flow inhibiting cooling along the surface of the effusion test plate.

3.3.4 Comparisons with CR=4 Cross Flow Only Data

Figure 31 shows line-averaged Nusselt number comparison plots with cross flow only data. Figure 32 shows area-averaged Nusselt number comparison plots with cross flow only data.

Line-averaged and area-averaged Nusselt number data are higher for the impingement/cross flow combination arrangement, compared to the cross flow only configuration. Nusselt number data tends to vary more with increasing Reynolds number and initial blowing ratio for the combination impingement/cross flow data, compared to the cross flow only data. This is due to the contribution of the impingement flow, which provides more coolant to the surface of the effusion plate with increasing Re_{imp}.

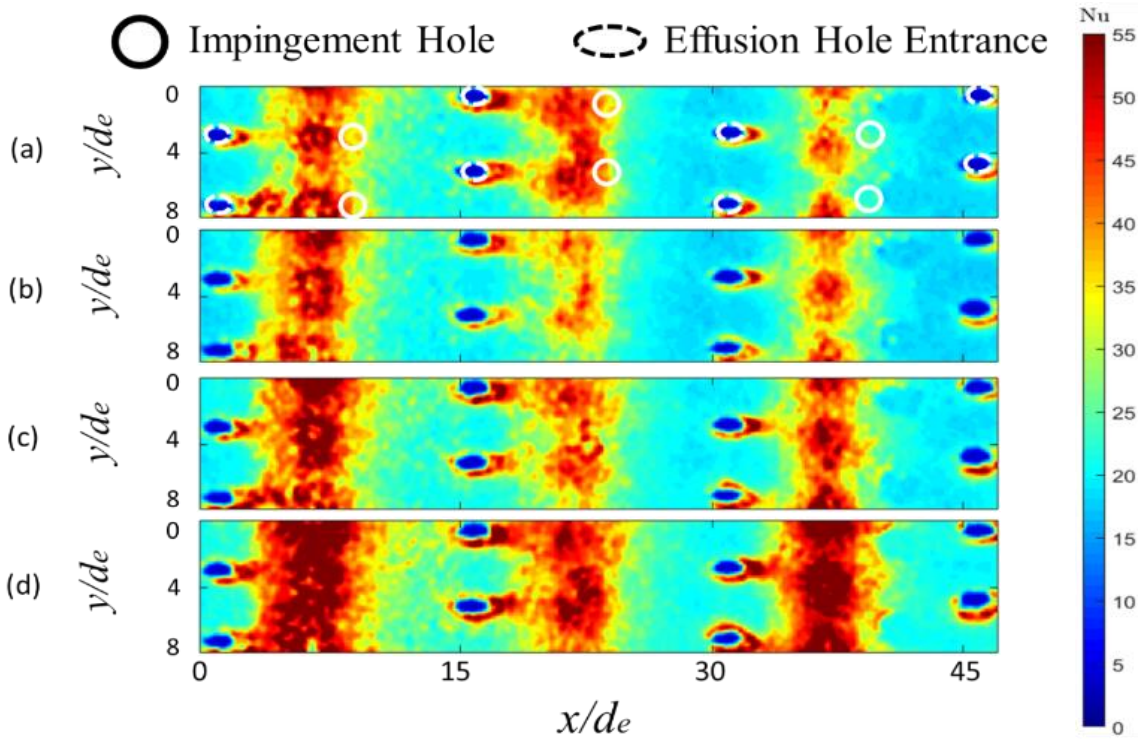

Figure 26. Surface Nusselt number variations for combined impingement and cross flow arrangement. Impingement and effusion hole locations are indicated within part (a). (a), BR=5.9 (b), BR=6.9 (c), BR=8.3 (d) BR=9.8. Data is for CASE 1 configuration for constant Re_{cf}, as Re_{imp} varies. Re_{ms} ranges from 157,201 to 161,193, and $Re_{ms,Avg}$ ranges from 233,000 to 244,000.

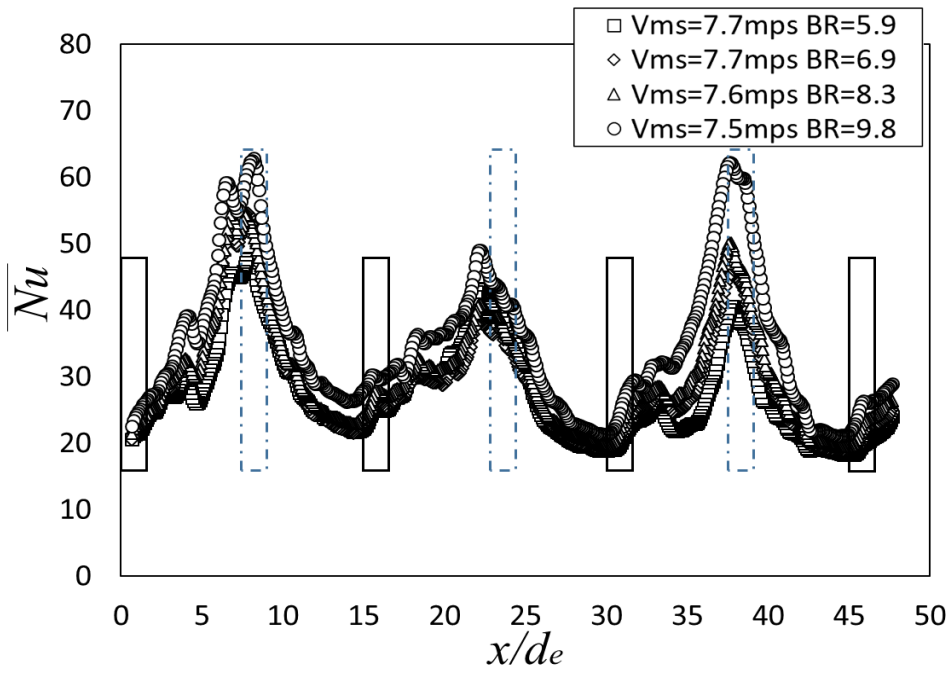

Figure 27. Line-averaged Nusselt number data for combined impingement and cross flow arrangement. Effusion hole locations are denoted by black boxes. Impingement hole locations are denoted by blue dashed boxes. Data is for CASE 1 configuration for constant Re_{cf}, as Re_{imp} varies. Re_{ms} ranges from 157,201 to 161,193, and $Re_{ms,Avg}$ ranges from 233,000 to 244,000.

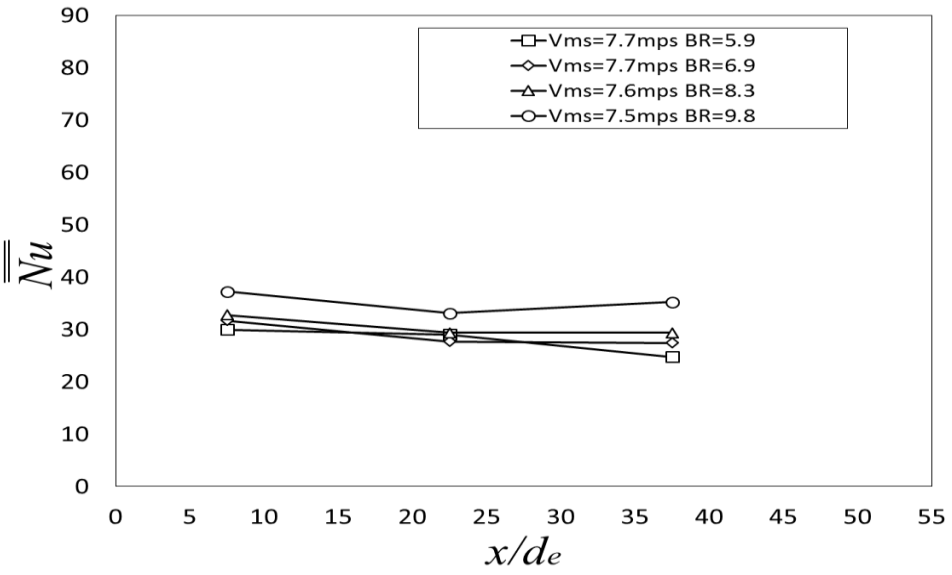

Figure 28. Spatially-averaged Nusselt number data for combined impingement and cross flow arrangement. Data is for CASE 1 configuration for constant Re_{cf}, as Re_{imp} varies. Re_{ms} ranges from 157,201 to 161,193, and $Re_{ms,Avg}$ ranges from 233,000 to 244,000.

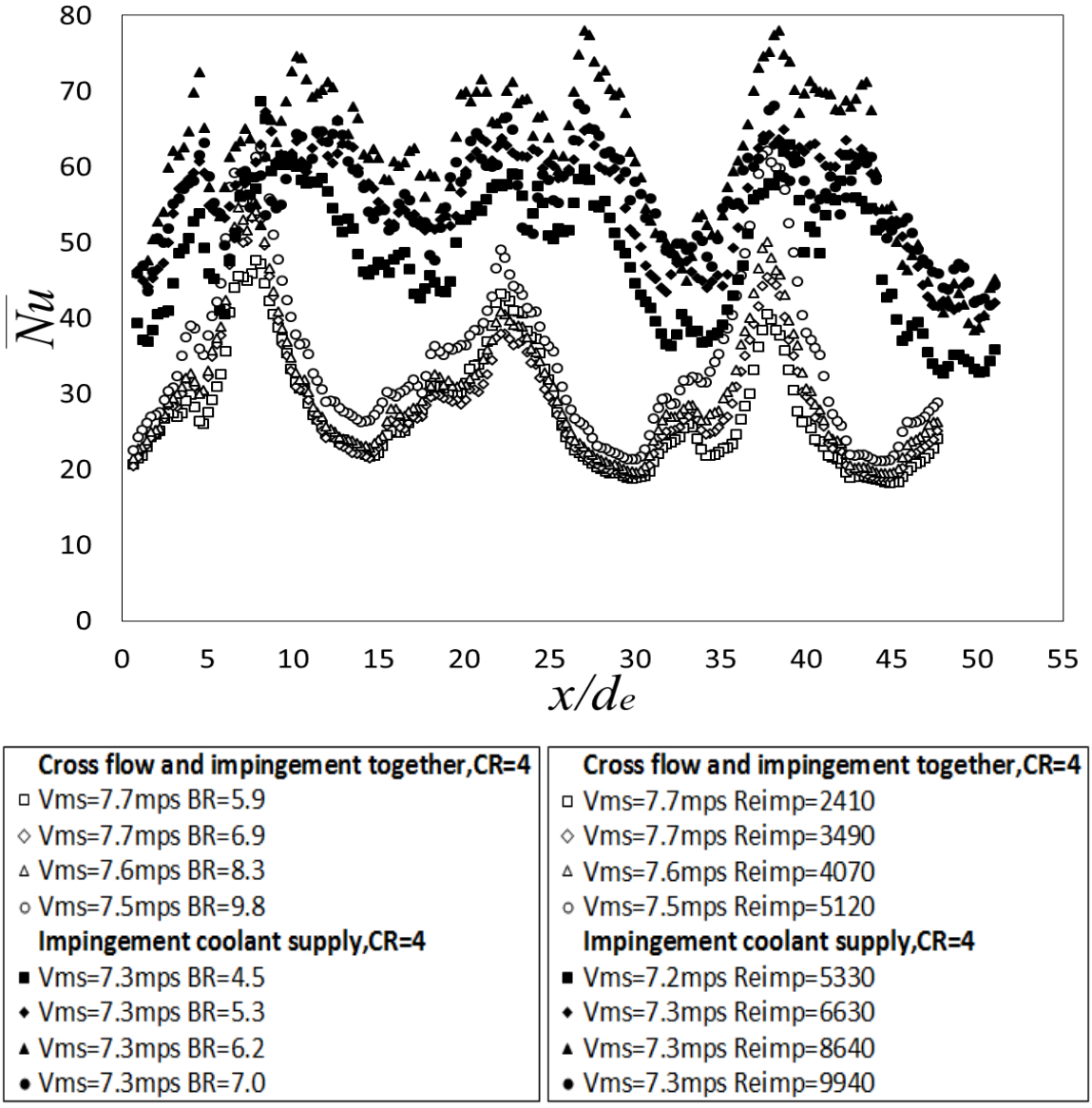

Figure 29. Line-averaged Nusselt number comparison for all experimental conditions for combined impingement and cross flow arrangement and impingement only, CR=4. Data is for CASE 1 configuration for constant Re_{cf}, as Re_{imp} varies. Re_{ms} ranges from 157,201 to 161,193, and $Re_{ms,Avg}$ ranges from 233,000 to 244,000.

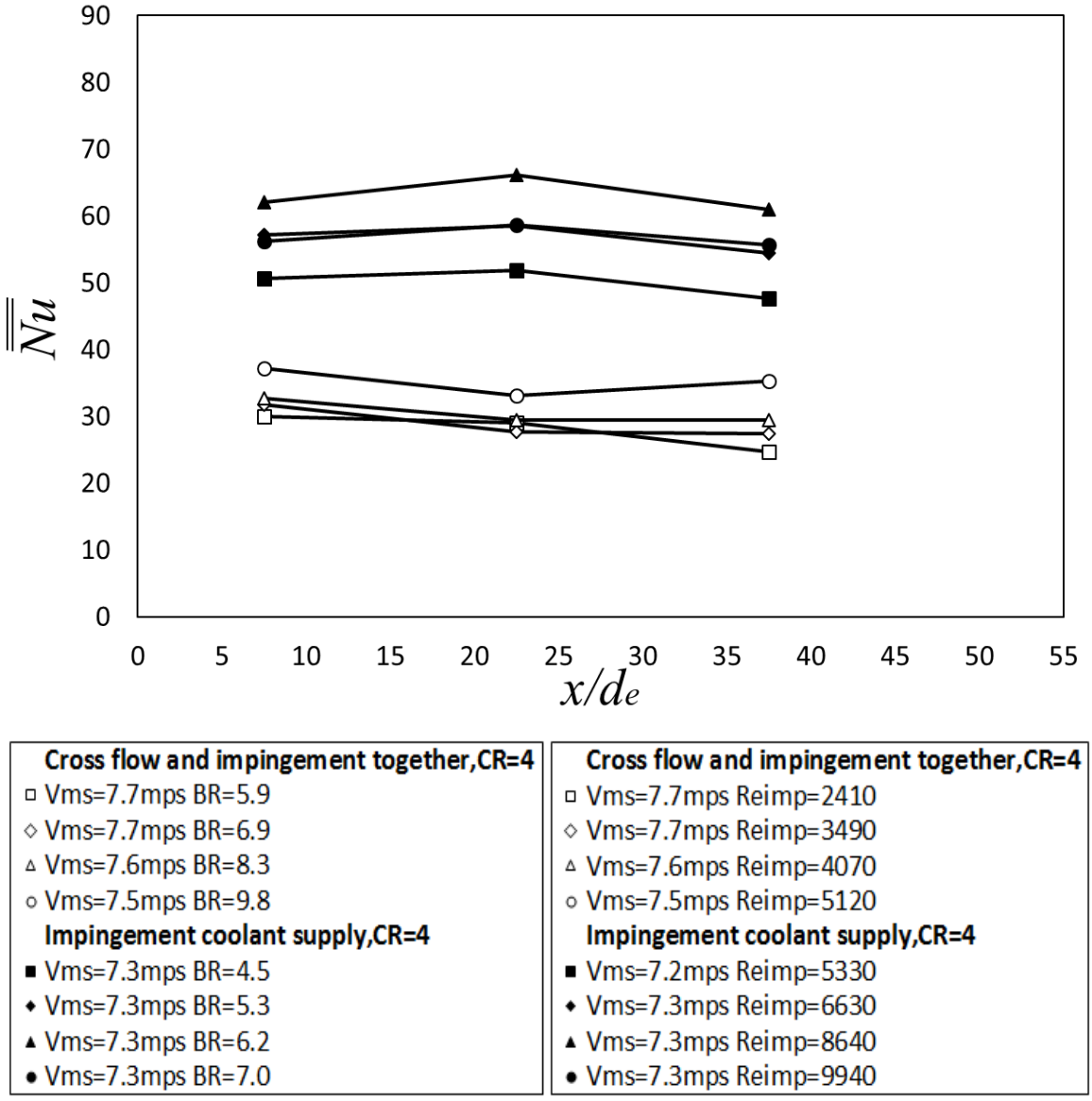

Figure 30. Spatially-averaged Nusselt number comparison for all experimental conditions for combined impingement and cross flow arrangement and impingement only, CR=4. Data is for CASE 1 configuration for constant Re_{cf}, as Re_{imp} varies. Re_{ms} ranges from 157,201 to 161,193, and $Re_{ms,Avg}$ ranges from 233,000 to 244,000.

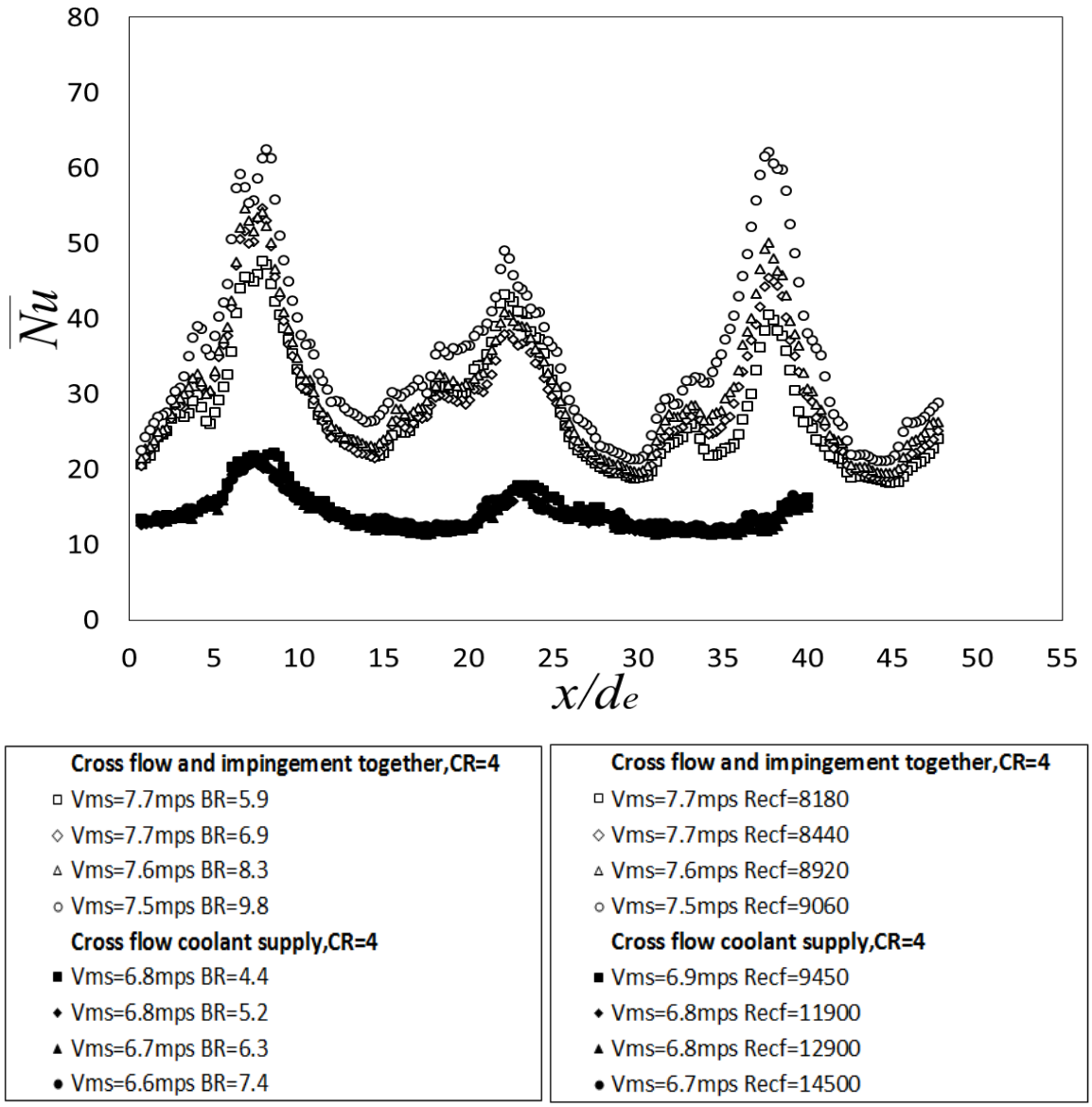

Figure 31. Line-averaged Nusselt number comparison for all experimental conditions for combined impingement and cross flow arrangement and cross flow only, CR=4. Data is for CASE 1 configuration for constant Re_{cf}, as Re_{imp} varies. Re_{ms} ranges from 157,201 to 161,193, and $Re_{ms,Avg}$ ranges from 233,000 to 244,000.

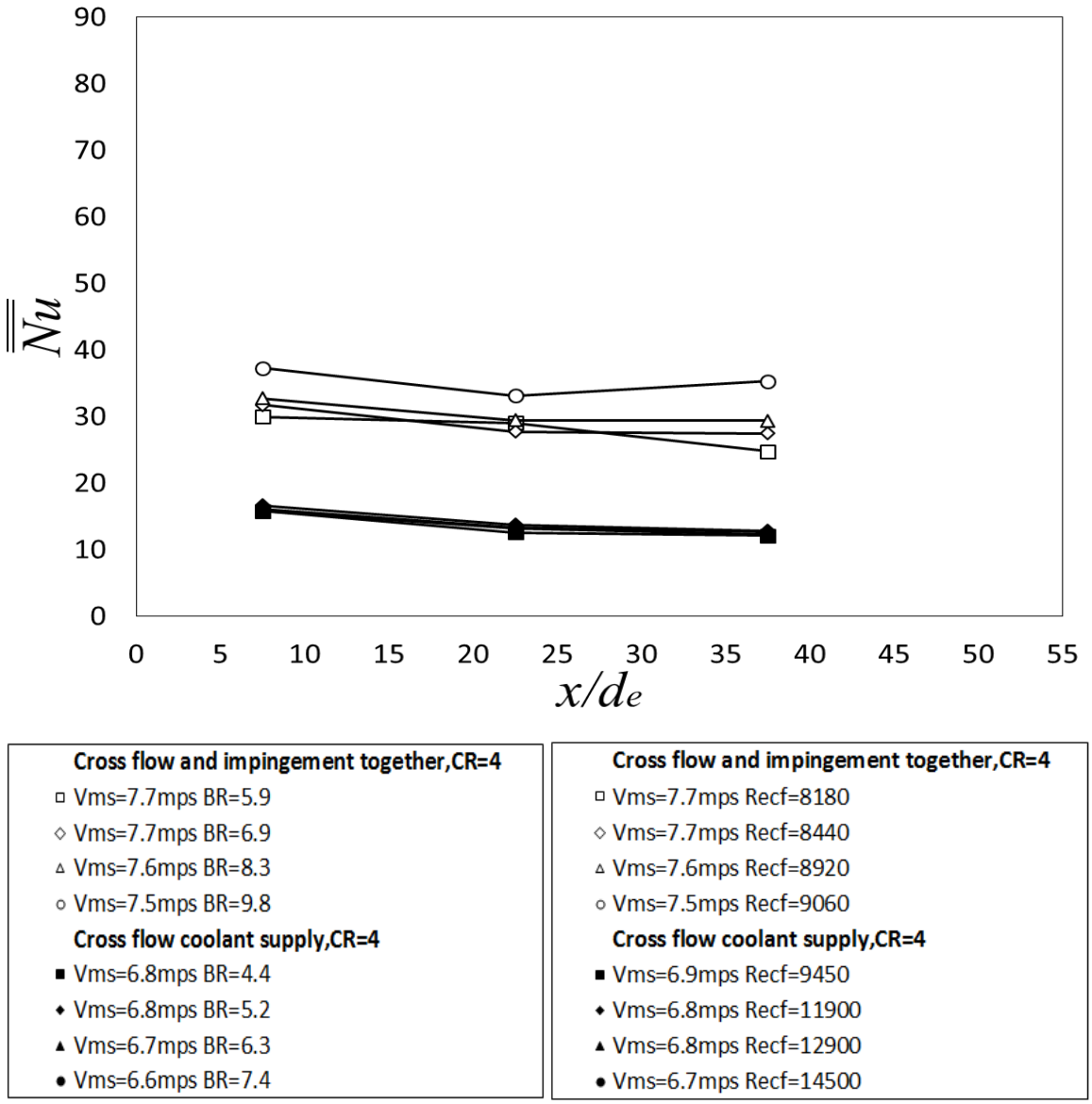

Figure 32. Spatially-averaged Nusselt number comparison for all experimental conditions for combined impingement and cross flow arrangement and cross flow only, CR=4. Data is for CASE 1 configuration for constant Re_{cf}, as Re_{imp} varies. Re_{ms} ranges from 157,201 to 161,193, and $Re_{ms,Avg}$ ranges from 233,000 to 244,000.

3.4 Experimental Data for Constant Re_{cf} and Varying Re_{imp} for Mainstream Reynolds Numbers $Re_{ms,Avg}$ of 164,000 to 171,000

3.4.1 Experimental Conditions for Constant Re_{cf} and Varying Re_{imp} for Mainstream Reynolds Numbers $Re_{ms,Avg}$ of 164,000 to 171,000

Table 4. Experimental conditions and blower settings for CASE 2 low mainstream Reynolds number/constant cross flow Reynolds number/varying impingement Reynolds number.

Experimental Conditions for Pressure Drop Measurements																				
Main Flow						Cross Flow				Impingement Flow				Effusion Flow						
	Blower Setting	V_{ms}	Mass Flow Rate	Re_{ms}	$Re_{ms,avg}$	Blower Setting	V_{cf}	Mass Flow Rate	Re_{cf}	Blower Setting	V_{imp}	Mass Flow Rate	Re_{imp}	V_{ef}	Mach Number	Re_{ef}	Density Ratio	Velocity Ratio	Momentum Flux Ratio	Blowing Ratio
Test	[Hz]	[m/s]	[kg/s]			[Hz]	[m/s]	[kg/s]		[Hz]	[m/s]	[kg/s]		[m/s]			DR	VR	I	BR
1	33	5.17	0.652	107029	170601	14	0.56	0.025	5768	12.5	2.98	0.016	1643	27.7	0.08	11909	1.0	5.4	28.89	5.4
2	33	5.01	0.631	103685	167940	17	0.56	0.025	5769	15.5	3.98	0.022	2196	31.7	0.09	13586	1.0	6.4	40.64	6.4
3	33	4.99	0.629	103283	166360	20	0.56	0.025	5736	18.5	5.03	0.028	2777	36.0	0.11	15346	1.0	7.3	52.84	7.3
4	33	4.96	0.625	102709	164323	23	0.58	0.026	5950	21.25	5.89	0.032	3255	40.3	0.12	17160	1.0	8.2	67.35	8.2

Table 5. Experimental heat transfer conditions and blower settings for CASE 2 low mainstream Reynolds number/constant cross flow Reynolds number/varying impingement Reynolds number.

Experimental Conditions for Heat Transfer Measurements																				
Main Flow						Cross Flow				Impingement Flow				Effusion Flow						
	Blower Setting	V_{ms}	Mass Flow Rate	Re_{ms}	$Re_{ms,avg}$	Blower Setting	V_{cf}	Mass Flow Rate	Re_{cf}	Blower Setting	V_{imp}	Mass Flow Rate	Re_{imp}	V_{ef}	Mach Number	Re_{ef}	Density Ratio	Velocity Ratio	Momentum Flux Ratio	Blowing Ratio
Test	[Hz]	[m/s]	[kg/s]			[Hz]	[m/s]	[kg/s]		[Hz]	[m/s]	[kg/s]		[m/s]			DR	VR	I	BR
1	33	5.22	0.645	105900	168801	14	0.56	0.025	5768	12.5	2.98	0.016	1643	27.5	0.08	11964	1.03	5.3	28.88	5.5
2	33	5.07	0.623	102365	165803	17	0.56	0.025	5769	15.5	3.98	0.022	2196	31.6	0.09	13649	1.03	6.3	40.69	6.5
3	33	5.04	0.622	102166	164560	20	0.56	0.025	5736	18.5	5.03	0.028	2777	35.8	0.11	15410	1.03	7.2	52.91	7.4
4	33	5.02	0.618	101555	162478	23	0.58	0.026	5950	21.25	5.89	0.032	3255	40.1	0.12	17246	1.03	8.1	67.42	8.3

Table 4 presents the experimental conditions for pressure drop measurements. Table 5 gives the experimental conditions for the heat transfer measurements. These values are taken for the CASE 2 configuration. Re_{ms} ranges from 102,709 to 107,029, $Re_{ms,Avg}$ ranges from 164,000 to 171,000, Re_{cf} ranges from 5,736 to 5,950, and Re_{imp} ranges from 1,643 to 3,255. For this case, Re_{cf} is kept constant while the Re_{imp} is varied. Included in the tables are blower settings, velocities, mass flow rates, and Reynolds numbers. These values are given for main flow, cross flow, impingement flow, and effusion flow.

3.4.2 Local Line-averaged and Area-averaged Nu Variations with Initial Blowing Ratio

Time-averaged, spatially-resolved surface Nusselt number variations are shown in Figure 33. Figure 34 presents line-averaged Nusselt number data. Figure 35 presents area-averaged Nusselt numbers with varying x/d_e, for a combined impingement and cross flow arrangement. As Re_{imp} and initial blowing ratio increase, while Re_{cf} is held constant, values of Nusselt numbers tend to increase, but with only very small variations with Re_{imp}. Concentrations of coolant build up, denoted by high Nusselt number values in Figure 33, continue to be qualitatively similar in magnitude with streamwise development. Such trends are also evident within Figure 34, where the peaks of line-averaged Nusselt number are similar in magnitude as x/d_e varies. As the Reynolds number and initial blowing ratio increase, so does the uniform increase of coolant build up along the effusion test plate. Such an increase is due to diminished negative effects caused by the cross flow. Because Re_{cf} in CASE 2 is held constant at a lower value compared to CASE 1, impingement flow is able spread coolant in a more uniform manner along the effusion test plate. However, due to the lower Re_{imp} values in CASE 2, the overall amount of thermal protection along the effusion test plate is reduced in comparison to CASE 1.

3.4.3 Comparisons with CR=4 Impingement Only Data

Figure 36 shows line-averaged Nusselt numbers for the combination arrangement, and for the impingement only configuration. Figure 37 shows the associated area-averaged Nusselt number data. Compared with the impingement only configuration, values of line-averaged and area-averaged Nusselt numbers for the combination impingement/cross flow tend to show only small variations with increasing initial blowing ratio at each x/d_e location. Magnitudes of Nusselt numbers for the combination arrangement tend to be lower in comparison to impingement only values, when compared at the same blowing ratio and x/d_e values. The addition of cross flow in the combination impingement/cross flow configuration tends to reduce the thermal protection along the cold surface of the effusion test plate, resulting in lower Nusselt number values relative to the impingement only configuration.

3.4.4 Comparisons with CR=4 Cross Flow Only Data

Figure 38 shows line-averaged Nusselt numbers for the combination arrangement, and for the cross flow only arrangement. Figure 39 shows the associated area-averaged Nusselt number data. When compared to the cross flow only configuration, values of line-averaged and area-averaged Nusselt number data are higher for the impingement/cross flow combination

arrangement, when compared at the same blowing ratio and x/d_e values. The cross flow restricts the impingement flow, thus causing the Nusselt numbers to vary, with changing Reynolds number, more similarly to a cross flow only configuration, than to an impingement only configuration.

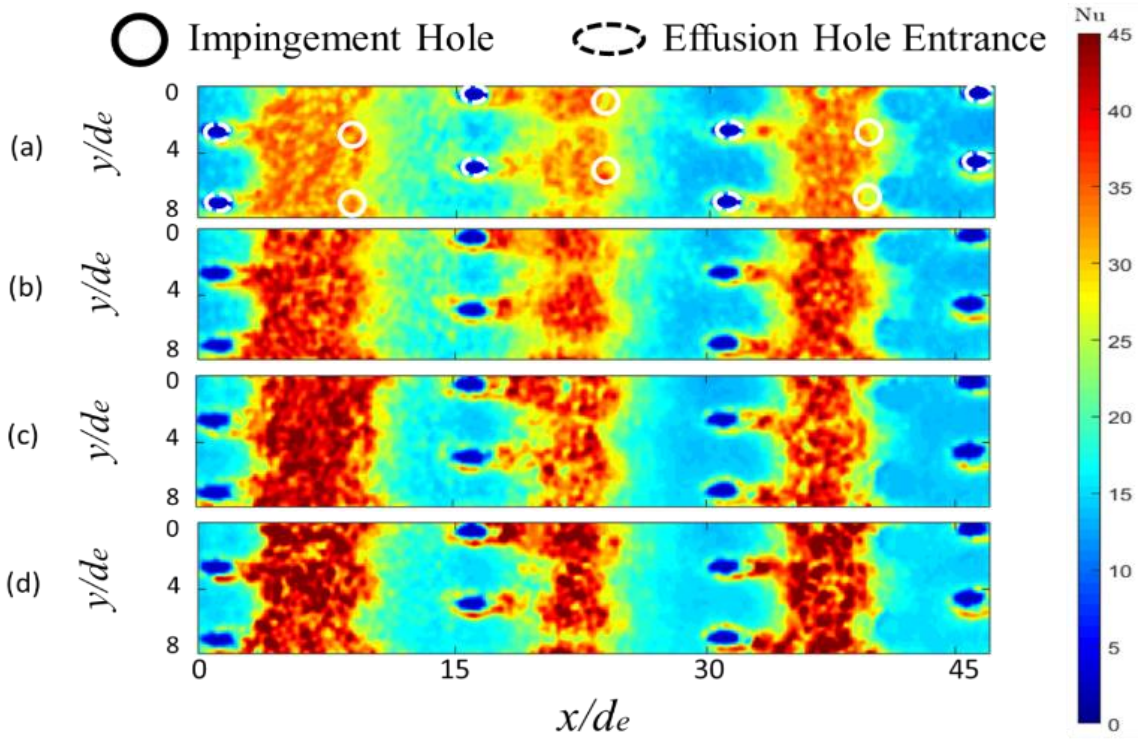

Figure 33. Surface Nusselt number variations for combined impingement and cross flow arrangement. Impingement and effusion hole locations are indicated within part (a). (a), BR=5.4 (b), BR=6.4 (c), BR=7.3 (d) BR=8.2. Data is for CASE 2 configuration for constant Re_{cf}, as Re_{imp} varies. Re_{ms} ranges from 102,709 to 107,029, and $Re_{ms,Avg}$ ranges from 164,000 to 171,000.

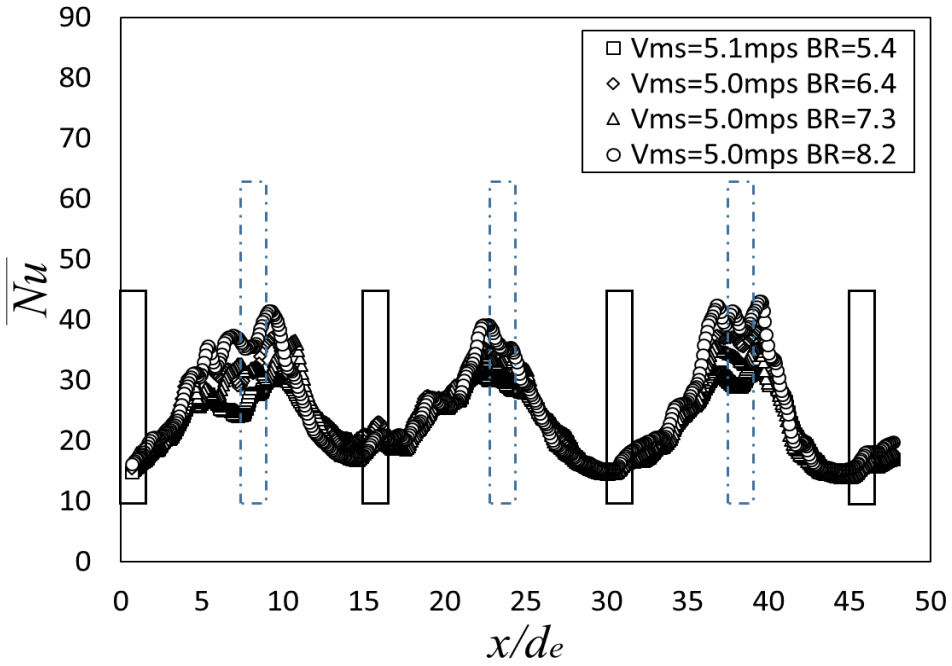

Figure 34. Line-averaged Nusselt number data for combined impingement and cross flow arrangement. Effusion hole locations are denoted by black boxes. Impingement hole locations are denoted by blue dashed boxes. Data is for CASE 2 configuration for constant Re_{cf}, as Re_{imp} varies. Re_{ms} ranges from 102,709 to 107,029, and $Re_{ms,Avg}$ ranges from 164,000 to 171,000.

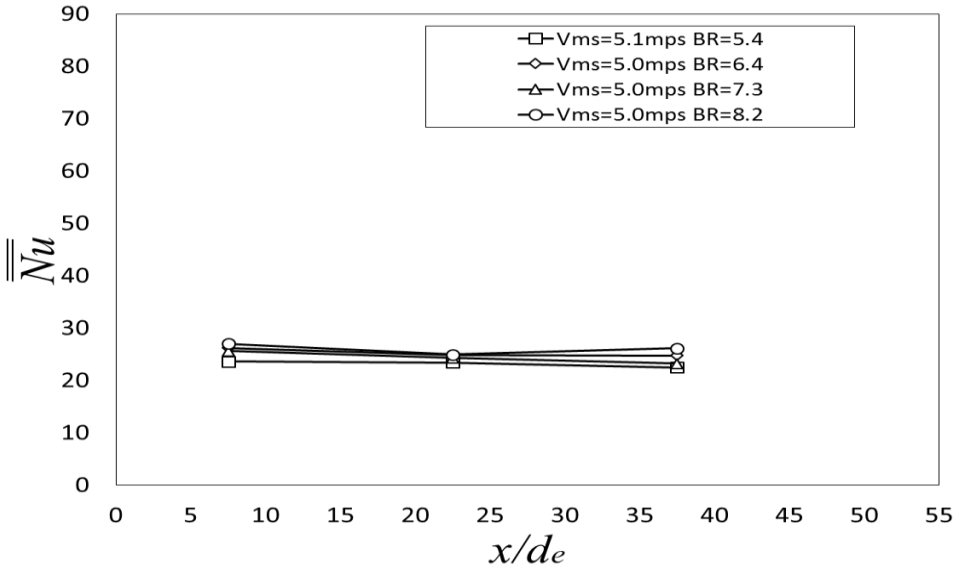

Figure 35. Spatially-averaged Nusselt number data for combined impingement and cross flow arrangement. Data is for CASE 2 configuration for constant Re_{cf}, as Re_{imp} varies. Re_{ms} ranges from 102,709 to 107,029, and $Re_{ms,Avg}$ ranges from 164,000 to 171,000.

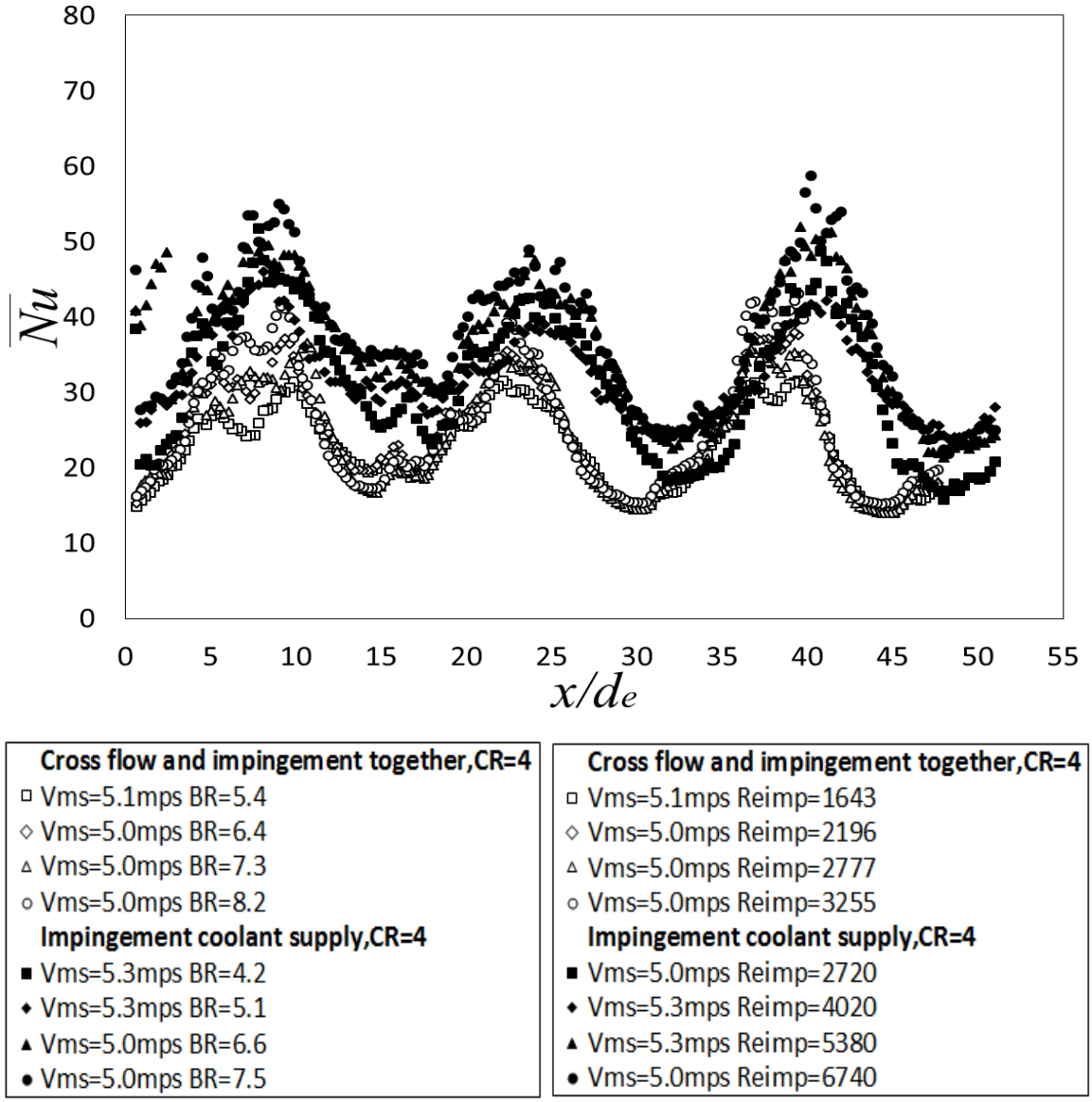

Figure 36. Line-averaged Nusselt number comparison for all experimental conditions for combined impingement and cross flow arrangement and impingement only, CR=4. Data is for CASE 2 configuration for constant Re_{cf}, as Re_{imp} varies. Re_{ms} ranges from 102,709 to 107,029, and $Re_{ms,Avg}$ ranges from 164,000 to 171,000.

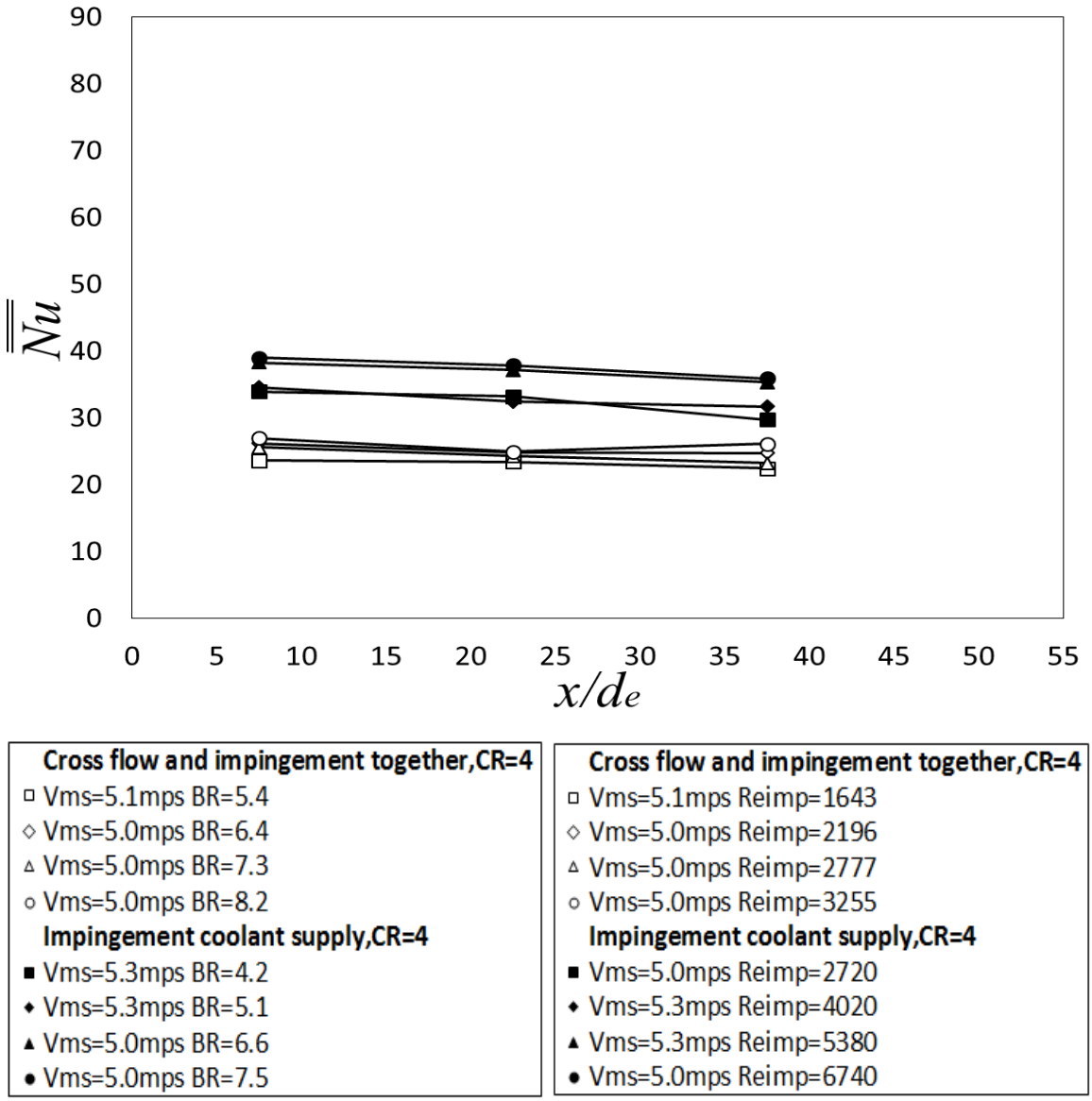

Figure 37. Spatially-averaged Nusselt number comparison for all experimental conditions for combined impingement and cross flow arrangement and impingement only, CR=4. Data is for CASE 2 configuration for constant Re_{cf}, as Re_{imp} varies. Re_{ms} ranges from 102,709 to 107,029, and $Re_{ms,Avg}$ ranges from 164,000 to 171,000.

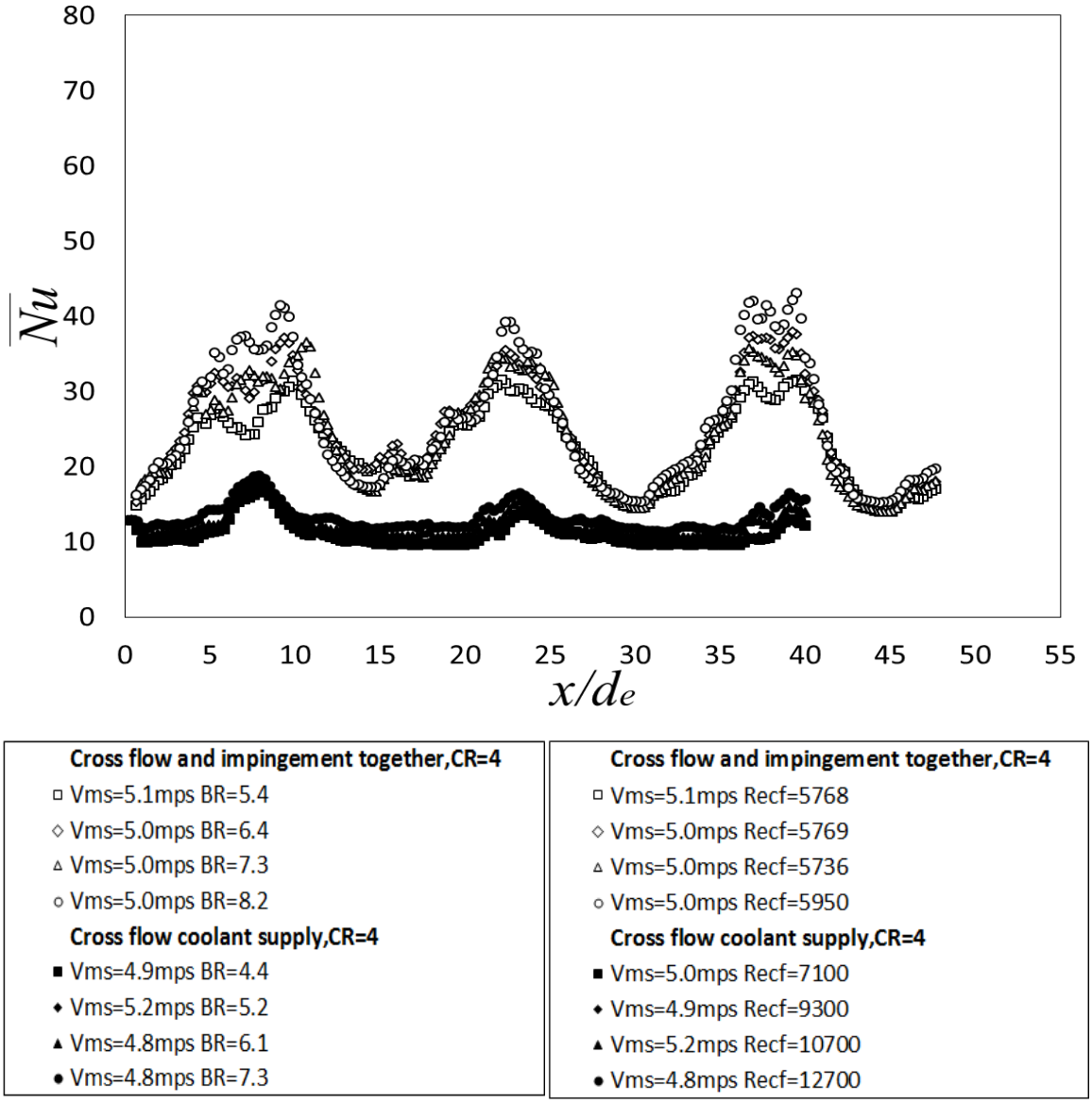

Figure 38. Line-averaged Nusselt number comparison for all experimental conditions for combined impingement and cross flow arrangement and cross flow only, CR=4. Data is for CASE 2 configuration for constant Re_{cf}, as Re_{imp} varies. Re_{ms} ranges from 102,709 to 107,029, and $Re_{ms,Avg}$ ranges from 164,000 to 171,000.

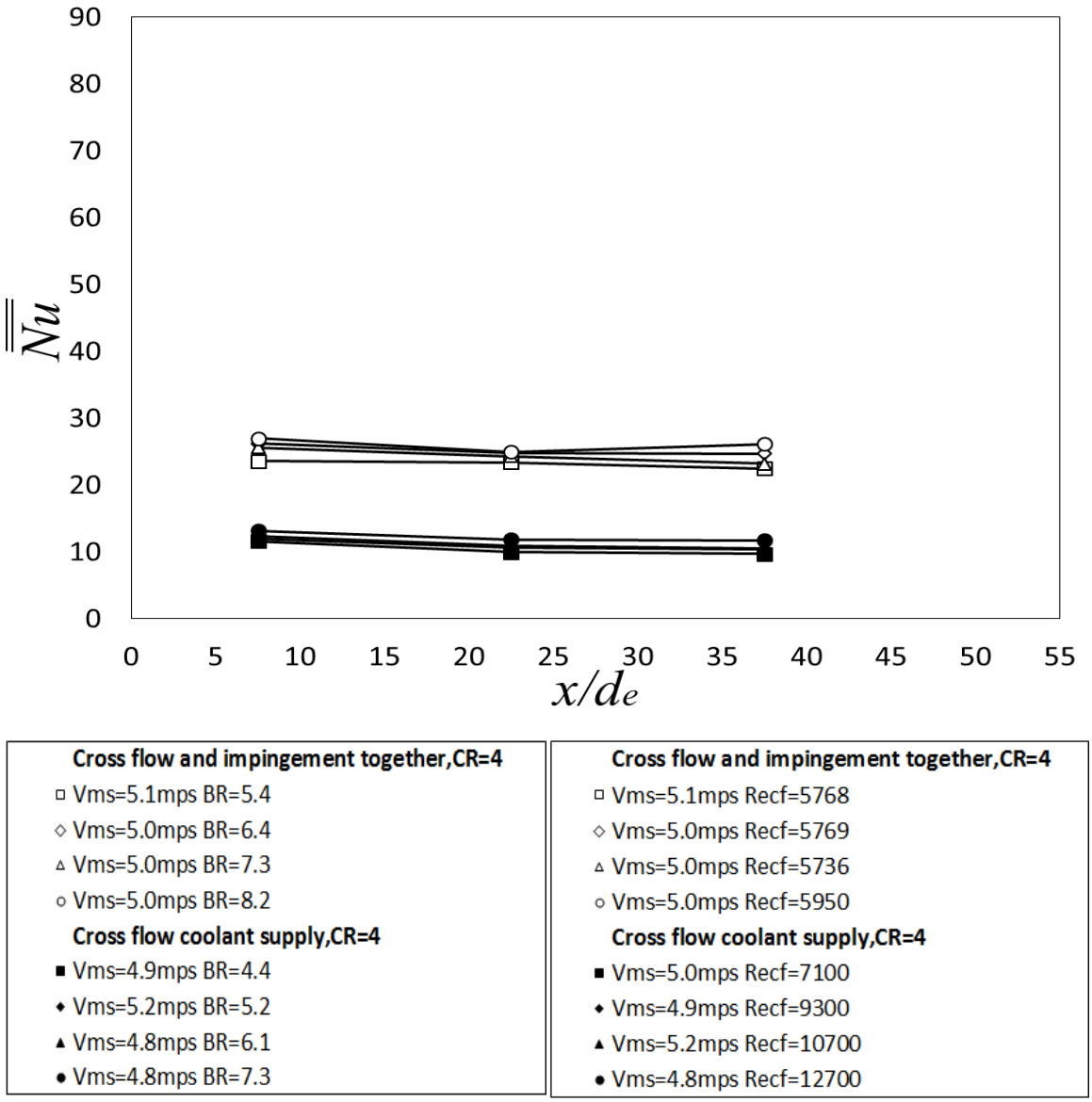

Figure 39. Spatially-averaged Nusselt number comparison for all experimental conditions for combined impingement and cross flow arrangement and cross flow only, CR=4. Data is for CASE 2 configuration for constant Re_{cf}, as Re_{imp} varies. Re_{ms} ranges from 102,709 to 107,029, and $Re_{ms,Avg}$ ranges from 164,000 to 171,000.

3.5 Experimental Data for Constant Re_{imp} and Varying Re_{cf} for Mainstream Reynolds Numbers $Re_{ms,Avg}$ of 236,000 to 245,000

3.5.1 Experimental Conditions for Constant Re_{imp} and Varying Re_{cf} for Mainstream Reynolds Numbers $Re_{ms,Avg}$ of 236,000 to 245,000

Table 6. Experimental conditions and blower settings for CASE 3 high mainstream Reynolds number/constant impingement flow Reynolds number/varying cross flow Reynolds number.

Experimental Conditions for Pressure Drop Measurements																				
Main Flow						Cross Flow				Impingement Flow				Effusion Flow						
	Blower Setting	V_{ms}	Mass Flow Rate	Re_{ms}	$Re_{ms,avg}$	Blower Setting	V_{cf}	Mass Flow Rate	Re_{cf}	Blower Setting	V_{imp}	Mass Flow Rate	Re_{imp}	V_{ef}	Mach Number	Re_{ef}	Density Ratio	Velocity Ratio	Momentum Flux Ratio	Blowing Ratio
Test	[Hz]	[m/s]	[kg/s]			[Hz]	[m/s]	[kg/s]		[Hz]	[m/s]	[kg/s]		[m/s]			DR	VR	I	BR
1	46	7.85	0.989	162338	244741	24.5	0.87	0.039	8914	20	4.92	0.027	2719	45.0	0.13	19318	1.0	5.8	33.61	5.8
2	46	7.78	0.980	160947	241887	28.5	1.05	0.047	10708	22.75	4.85	0.027	2678	50.9	0.15	21826	1.0	6.6	44.11	6.6
3	46	7.70	0.970	159267	238571	32.5	1.34	0.060	13679	25.65	4.93	0.027	2723	56.9	0.17	24398	1.0	7.5	56.72	7.5
4	46	7.67	0.966	158601	235544	36.5	1.63	0.073	16655	28.6	4.90	0.027	2706	63.0	0.18	27087	1.0	8.4	70.89	8.4

Table 7. Experimental heat transfer conditions and blower settings for CASE 3 high mainstream Reynolds number/constant impingement flow Reynolds number/varying cross flow Reynolds number.

Experimental Conditions for Heat Transfer Measurements																				
Main Flow						Cross Flow				Impingement Flow				Effusion Flow						
	Blower Setting	V_{ms}	Mass Flow Rate	Re_{ms}	$Re_{ms,avg}$	Blower Setting	V_{cf}	Mass Flow Rate	Re_{cf}	Blower Setting	V_{imp}	Mass Flow Rate	Re_{imp}	V_{ef}	Mach Number	Re_{ef}	Density Ratio	Velocity Ratio	Momentum Flux Ratio	Blowing Ratio
Test	[Hz]	[m/s]	[kg/s]			[Hz]	[m/s]	[kg/s]		[Hz]	[m/s]	[kg/s]		[m/s]			DR	VR	I	BR
1	46	7.97	0.973	159838	240971	24.5	0.87	0.039	8914	20	4.92	0.027	2719	44.9	0.13	19329	1.04	5.7	33.49	5.9
2	46	7.90	0.965	158429	238102	28.5	1.05	0.047	10708	22.75	4.85	0.027	2678	50.9	0.15	21832	1.04	6.5	43.92	6.7
3	46	7.82	0.954	156751	234803	32.5	1.34	0.060	13679	25.65	4.93	0.027	2723	56.9	0.17	24373	1.04	7.4	56.34	7.6
4	46	7.76	0.954	156716	232746	36.5	1.63	0.073	16655	28.6	4.90	0.027	2706	63.2	0.18	27020	1.03	8.3	70.20	8.5

Table 6 presents the experimental conditions for pressure drop measurements. Table 7 gives the experimental conditions for the heat transfer measurements. These values are taken for the CASE 3 configuration. Re_{ms} ranges from 158,601 to 162,338, $Re_{ms,Avg}$ ranges from 236,000 to 245,000, Re_{cf} ranges from 8,914 to 16,655, and Re_{imp} ranges from 2,678 to 2,723. For this case, Re_{imp} is kept constant while the Re_{cf} is varied. Included in the tables are blower settings, velocities, mass flow rates, and Reynolds numbers. These values are given for main flow, cross flow, impingement flow, and effusion flow.

3.5.2 Local Line-averaged and Area-averaged Nu Variations with Initial Blowing Ratio

Time-averaged, spatially-resolved surface Nusselt number variations are shown in Figure 40. Figure 41 presents line-averaged Nusselt number data. Figure 42 presents area-averaged Nusselt numbers with varying x/d_e, for a combined impingement and cross flow arrangement. As Re_{cf} and initial blowing ratio increase, while Re_{imp} is held constant, values of Nusselt number tend to decrease, but only by small amounts as blowing ratio, BR, changes. Within Figure 40, magnitudes of coolant build up tend to decrease with streamwise development along the effusion test plate. Locations of coolant build up also decrease and almost disappear with increasing initial blowing ratio. At the highest blowing ratio, two weak recirculating zones, indicated by near-zero Nusselt numbers, appear slightly left of their corresponding impingement hole locations. These zones likely appear due to complex flow interactions between the impingement flow and cross flow, occurring as the impingement jets turn upstream to enter the effusion holes. These trends are also reflected in line-average Nusselt Number data from Figure 41. Higher values of Re_{cf} are the main cause for such behavior. Compared to CASE 1 and CASE 2, where thermal protection often increases with increasing initial blowing ratio, CASE 3 shows a decrease in thermal protection both with streamwise development and with increasing initial blowing ratio.

3.5.3 Comparisons with CR=4 Impingement Only Data

Figure 43 shows line-averaged Nusselt number comparisons for the combination arrangement, and for the impingement only data. Figure 44 shows associated area-averaged Nusselt number comparisons. As Reynolds number and initial blowing ratio increase, area-averaged Nusselt number and the line-averaged Nusselt number data (between the peaks in Figure 43) vary by very small amounts. Combination Nusselt number data also show a decrease with increasing initial blowing ratio. As for previous cases, Nusselt numbers are generally lower compared to impingement only data, when compared at the same x/d_e and initial blowing ratio.

3.5.4 Comparisons with CR=4 Cross Flow Only Data

Figure 45 shows line-averaged Nusselt number comparisons for the combination arrangement, and for the cross flow only configuration. Figure 46 shows associated area-averaged Nusselt number comparisons. Line-averaged and area-averaged Nusselt number data for the impingement/cross flow combination arrangement are generally higher, compared to the cross flow only configuration, when compared at the x/d_e and blowing ratio. However, Nusselt

number data for the combination arrangement vary more with increasing Reynolds number and initial blowing ratio, compared to the cross flow only data, especially near local-maximum locations.

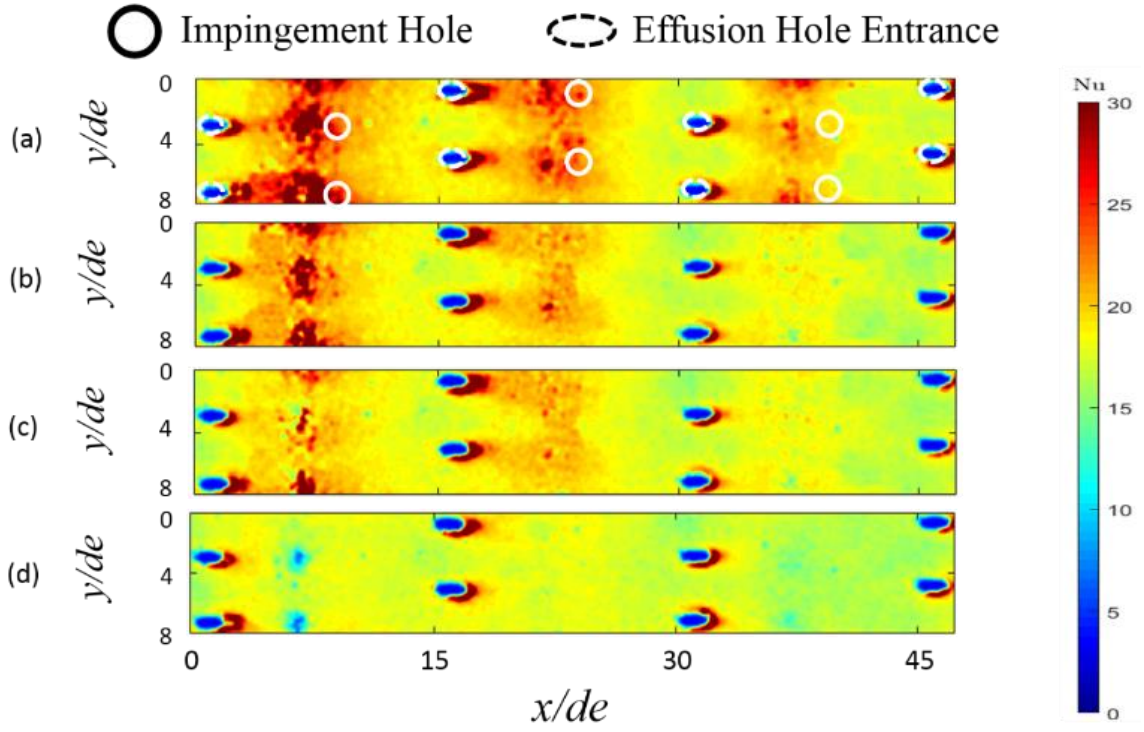

Figure 40. Surface Nusselt number variations for combined impingement and cross flow arrangement. Impingement and effusion hole locations are indicated within part (a). (a), BR=5.8, (b) BR=6.6, (c) BR=7.5, (d) BR=8.4. Data is for CASE 3 configuration for constant Re_{imp}, as Re_{cf} varies. Re_{ms} ranges from 158,601 to 162,338, and $Re_{ms,Avg}$ ranges from 236,000 to 245,000.

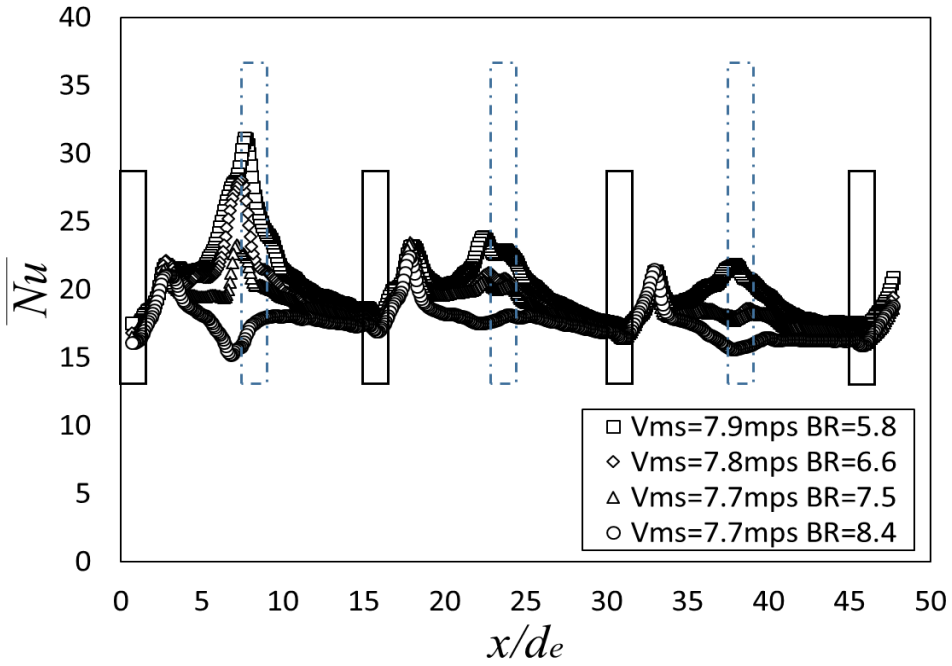

Figure 41. Line-averaged Nusselt number data for combined impingement and cross flow arrangement. Effusion hole locations are denoted by black boxes. Impingement hole locations are denoted by blue dashed boxes. Data is for CASE 3 configuration for constant Re_{imp}, as Re_{cf} varies. Re_{ms} ranges from 158,601 to 162,338, and $Re_{ms,Avg}$ ranges from 236,000 to 245,000.

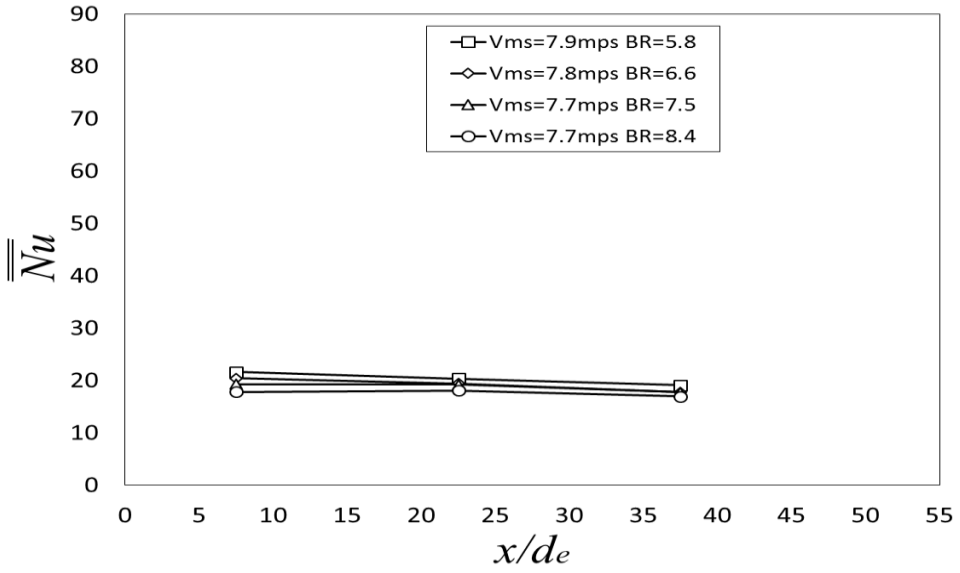

Figure 42 Spatially-averaged Nusselt number data for combined impingement and cross flow arrangement. Data is for CASE 3 configuration for constant Re_{imp}, as Re_{cf} varies. Re_{ms} ranges from 158,601 to 162,338, and $Re_{ms,Avg}$ ranges from 236,000 to 245,000.

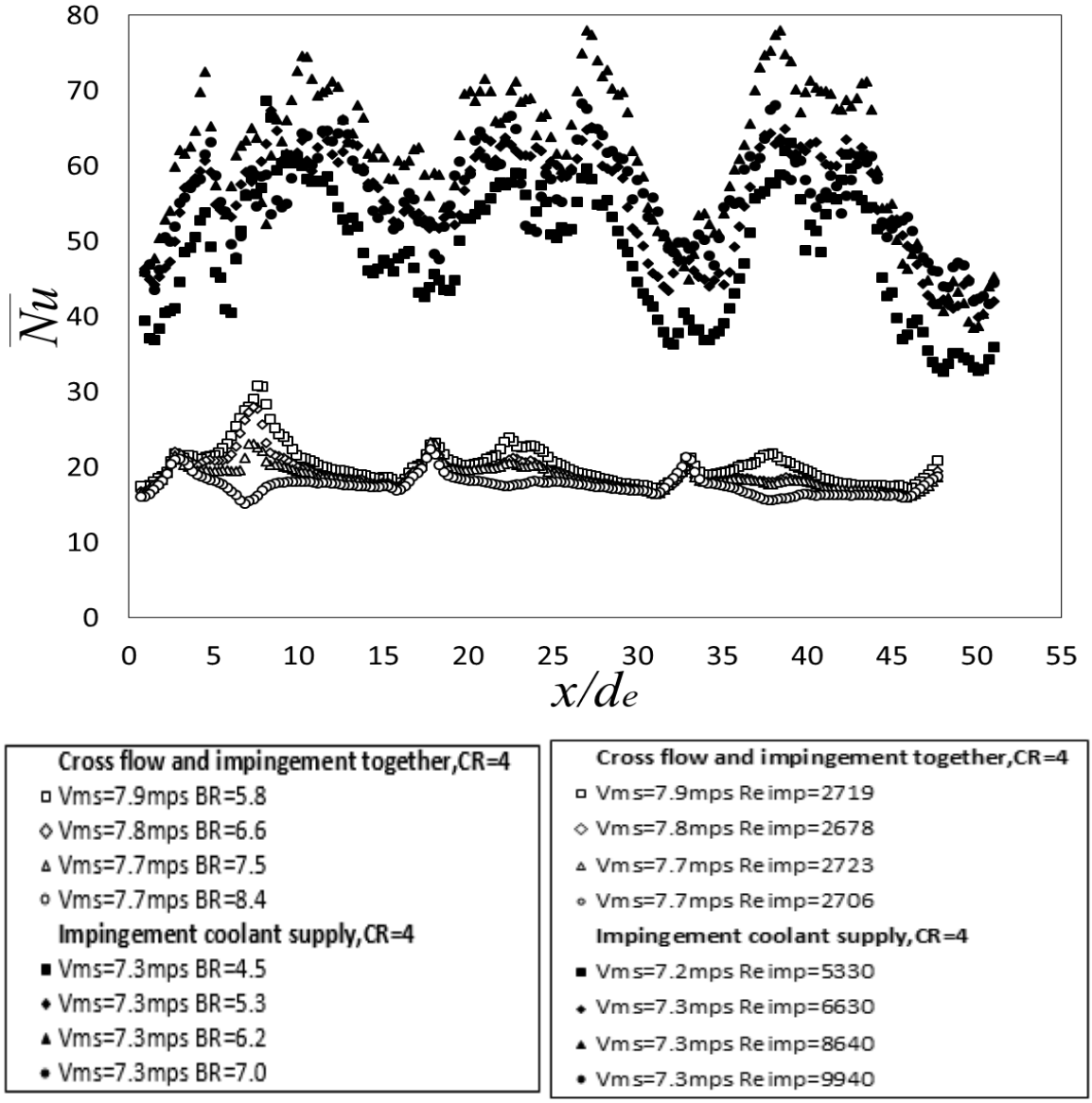

Figure 43. Line-averaged Nusselt number comparison for all experimental conditions for combined impingement and cross flow arrangement and impingement only, CR=4. Data is for CASE 3 configuration for constant Re_{imp}, as Re_{cf} varies. Re_{ms} ranges from 158,601 to 162,338, and $Re_{ms,Avg}$ ranges from 236,000 to 245,000.

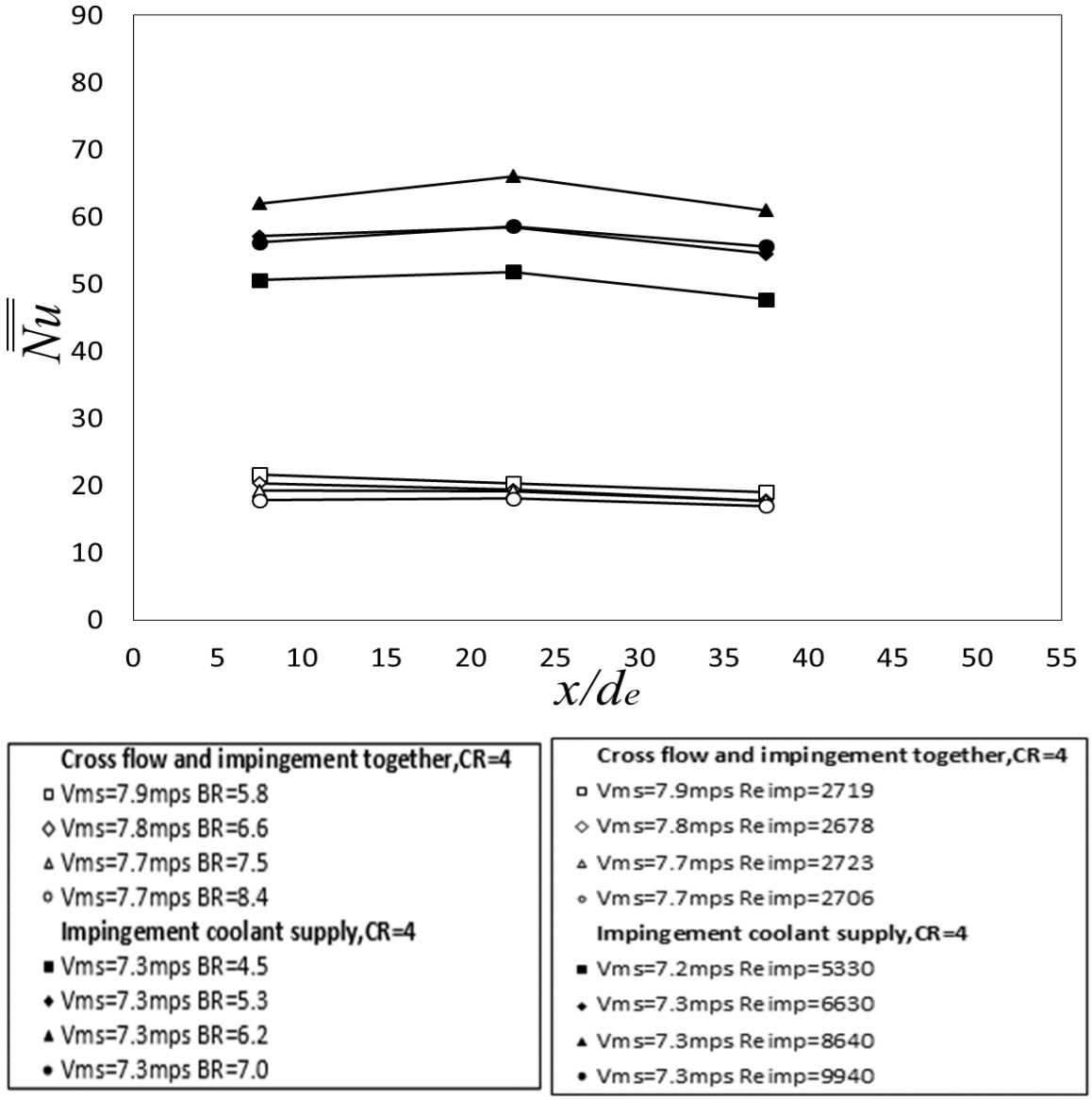

Figure 44. Spatially-averaged Nusselt number comparison for all experimental conditions for combined impingement and cross flow arrangement and impingement only, CR=4. Data is for CASE 3 configuration for constant Re_{imp}, as Re_{cf} varies. Re_{ms} ranges from 158,601 to 162,338, and $Re_{ms,Avg}$ ranges from 236,000 to 245,000.

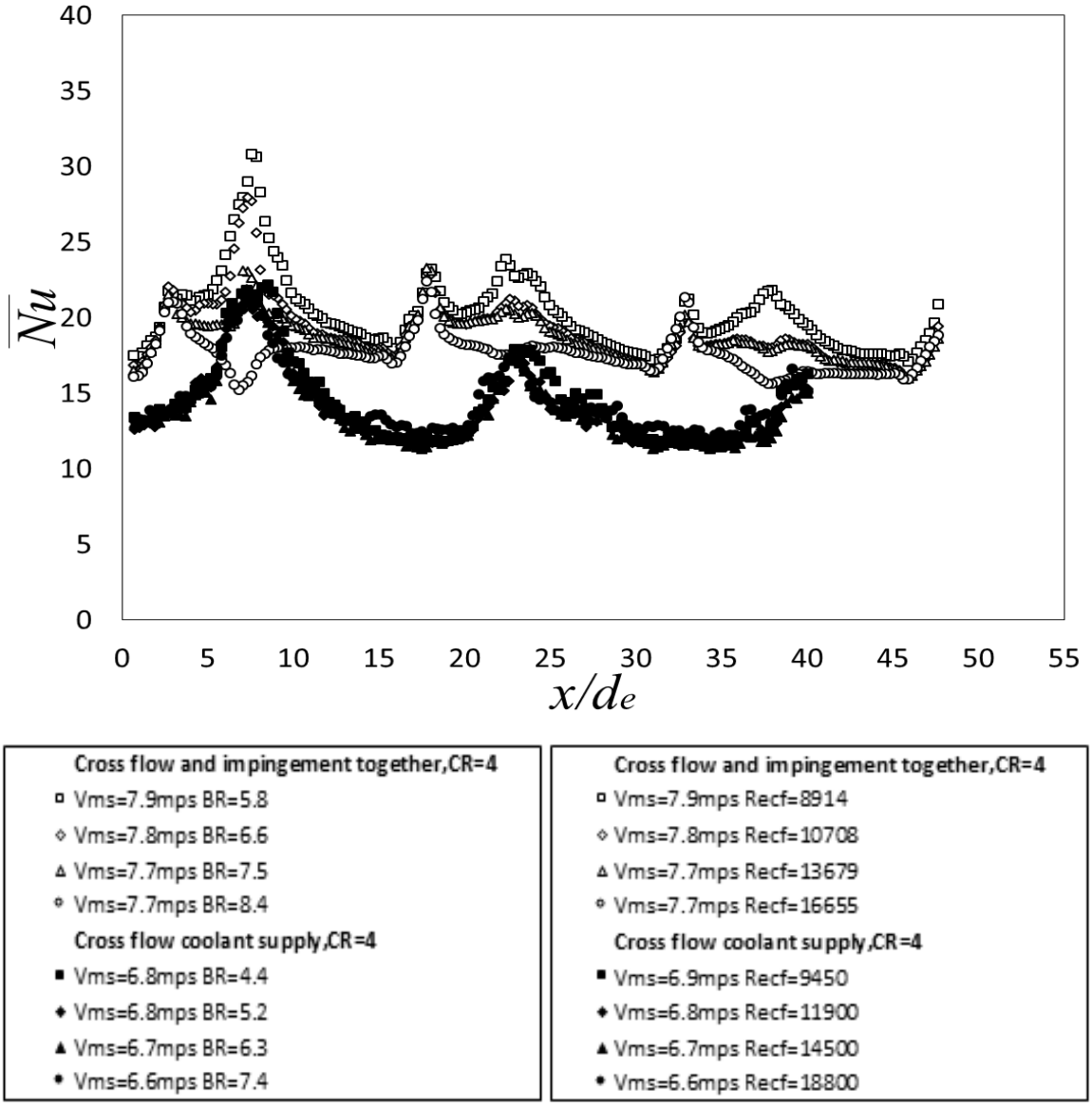

Figure 45. Line-averaged Nusselt number comparison for all experimental conditions for combined impingement and cross flow arrangement and cross flow only, CR=4. Data is for CASE 3 configuration for constant Re_{imp}, as Re_{cf} varies. Re_{ms} ranges from 158,601 to 162,338, and $Re_{ms,Avg}$ ranges from 236,000 to 245,000.

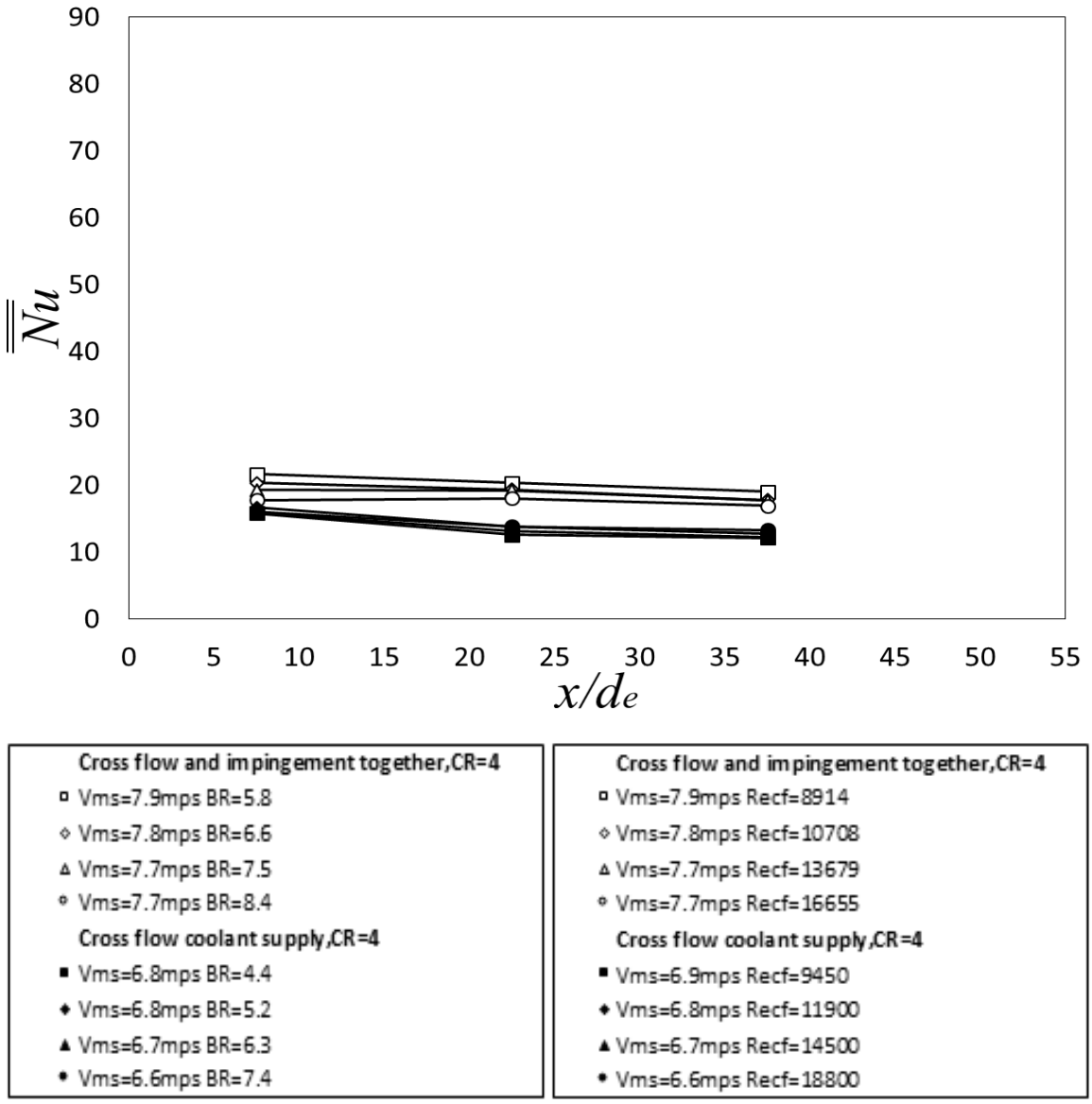

Figure 46. Spatially-averaged Nusselt number comparison for all experimental conditions for combined impingement and cross flow arrangement and cross flow only, CR=4. Data is for CASE 3 configuration for constant Re_{imp}, as Re_{cf} varies. Re_{ms} ranges from 158,601 to 162,338, and $Re_{ms,Avg}$ ranges from 236,000 to 245,000.

3.6 Experimental Data for Constant Re_{imp} and Varying Re_{cf} for Mainstream Reynolds Numbers $Re_{ms,Avg}$ of 162,000 to 168,000

3.6.1 Experimental Conditions for Constant Re_{imp} and Varying Re_{cf} for Mainstream Reynolds Numbers $Re_{ms,Avg}$ of 162,000 to 168,000

Table 8. Experimental conditions and blower settings for CASE 4 low mainstream Reynolds number/constant impingement flow Reynolds number/varying cross flow Reynolds number.

Experimental Conditions for Pressure Drop Measurements																				
Main Flow						Cross Flow				Impingement Flow				Effusion Flow						
	Blower Setting	V_{ms}	Mass Flow Rate	Re_{ms}	$Re_{ms,avg}$	Blower Setting	V_{cf}	Mass Flow Rate	Re_{cf}	Blower Setting	V_{imp}	Mass Flow Rate	Re_{imp}	V_{ef}	Mach Number	Re_{ef}	Density Ratio	Velocity Ratio	Momentum Flux Ratio	Blowing Ratio
Test	[Hz]	[m/s]	[kg/s]			[Hz]	[m/s]	[kg/s]		[Hz]	[m/s]	[kg/s]		[m/s]			DR	VR	I	BR
1	33	4.94	0.623	102389	168237	14	0.64	0.029	6550	12.5	2.89	0.016	1596	27.8	0.08	11989	1.0	5.7	31.98	5.7
2	33	4.94	0.624	102398	166736	17	0.83	0.037	8441	14.4	2.83	0.016	1565	31.9	0.09	13657	1.0	6.5	42.14	6.5
3	33	4.91	0.619	101707	164158	20	0.99	0.044	10101	16.5	2.87	0.016	1584	36.3	0.11	15493	1.0	7.5	55.61	7.5
4	33	4.79	0.605	99305	161881	23	1.20	0.054	12240	18.6	2.79	0.015	1542	41.0	0.12	17433	1.0	8.6	74.43	8.6

Table 9. Experimental heat transfer conditions and blower settings for CASE 4 low mainstream Reynolds number/constant impingement flow Reynolds number/varying cross flow Reynolds number.

Experimental Conditions for Heat Transfer Measurements																				
Main Flow						Cross Flow				Impingement Flow				Effusion Flow						
	Blower Setting	V_{ms}	Mass Flow Rate	Re_{ms}	$Re_{ms,avg}$	Blower Setting	V_{cf}	Mass Flow Rate	Re_{cf}	Blower Setting	V_{imp}	Mass Flow Rate	Re_{imp}	V_{ef}	Mach Number	Re_{ef}	Density Ratio	Velocity Ratio	Momentum Flux Ratio	Blowing Ratio
Test	[Hz]	[m/s]	[kg/s]			[Hz]	[m/s]	[kg/s]		[Hz]	[m/s]	[kg/s]		[m/s]			DR	VR	I	BR
1	33	5.02	0.614	100869	165740	14	0.64	0.029	6550	12.5	2.89	0.016	1596	27.8	0.08	12019	1.04	5.5	31.88	5.8
2	33	5.01	0.615	100971	164412	17	0.83	0.037	8441	14.4	2.83	0.016	1565	31.8	0.09	13702	1.04	6.3	41.87	6.6
3	33	4.99	0.610	100145	161636	20	0.99	0.044	10101	16.5	2.87	0.016	1584	36.2	0.11	15531	1.04	7.3	55.32	7.6
4	33	4.87	0.595	97794	159418	23	1.20	0.054	12240	18.6	2.79	0.015	1542	40.9	0.12	17473	1.04	8.4	73.99	8.8

Table 8 presents the experimental conditions for pressure drop measurements. Table 9 gives the experimental conditions for the heat transfer measurements. These values are taken for the CASE 4 configuration. Re_{ms} ranges from 99,305 to 102,398, $Re_{ms,Avg}$ ranges from 162,000 to 168,000, Re_{cf} ranges from 6,550 to 12,240, and Re_{imp} ranges from 1,542 to 1,596. For this case, Re_{imp} is kept constant while the Re_{cf} is varied. Included in the tables are blower settings, velocities, mass flow rates, and Reynolds numbers. These values are given for main flow, cross flow, impingement flow, and effusion flow.

3.6.2 Local Line-averaged and Area-averaged Nu Variations with Initial Blowing Ratio

Time-averaged, spatially-resolved surface Nusselt number variations are shown in Figure 47. Figure 48 presents associated line-averaged Nusselt number data. Figure 49 presents area-averaged Nusselt numbers with varying x/d_e, for a combined impingement and cross flow arrangement. As Re_{cf} and initial blowing ratio increase, while Re_{imp} is held constant, values of Nusselt numbers tend to increase, but only by very small amounts as blowing ratio changes. Figure 47 shows that areas of larger surface Nusselt number augmentation decrease slightly with increasing streamwise development. This decrease becomes more apparent at higher initial blowing ratio values. This trend is also evident in Figure 48. Figures 47 and 49 also show that Nusselt numbers for an initial blowing ratio of 8.6 are sometimes less than for an initial blowing ratio of 7.5.

3.6.3 Comparisons with CR=4 Impingement Only Data

Figure 50 shows line-averaged Nusselt number comparison plots for the combination arrangement, and for the with impingement only arrangement. Figure 51 shows associated area-averaged Nusselt number comparisons. Like CASE 1 and 2, combination arrangement line-averaged and area-averaged Nusselt number data vary by only small amounts, as initial blowing ratio and Reynolds number change. Unlike the impingement only data, combination line-averaged Nusselt number data peaks tend to decrease with increasing x/d_e. In addition, magnitudes of combination impingement/cross flow Nusselt numbers are often lower than impingement only data, when compared at the same x/d_e and blowing ratio.

3.6.4 Comparisons with CR=4 Cross Flow Only Data

Figure 52 shows line-averaged Nusselt number comparison plots for the combination arrangement, and for the cross flow only arrangement. Figure 53 shows associated area-averaged Nusselt number data. Similar to CASES 1, 2, and 3, values of line-averaged and area-averaged Nusselt number data for the combination impingement/cross flow arrangement are often higher than for the cross flow only arrangement. While cross flow only Nusselt number data generally increase with increasing initial blowing ratio, Nusselt number data for the combination impingement/cross flow arrangement often decrease somewhat as initial blowing ratio increases.

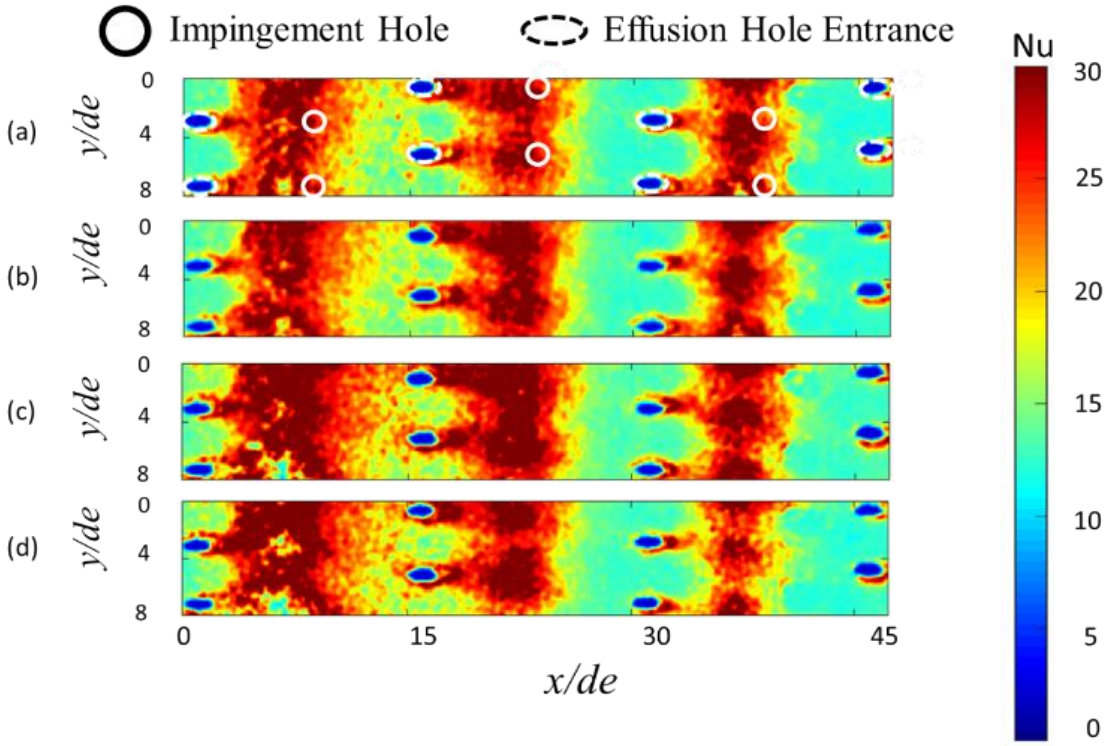

Figure 47. Surface Nusselt number variations for combined impingement and cross flow arrangement. Impingement and effusion hole locations are indicated within part (a). (a), BR=5.7 (b), BR=6.5 (c), BR=7.5 (d) BR=8.6. Data is for CASE 4 configuration for constant Re_{imp}, as Re_{cf} varies. Re_{ms} ranges from 99,305 to 102,398, and $Re_{ms,Avg}$ ranges from 162,000 to 168,000.

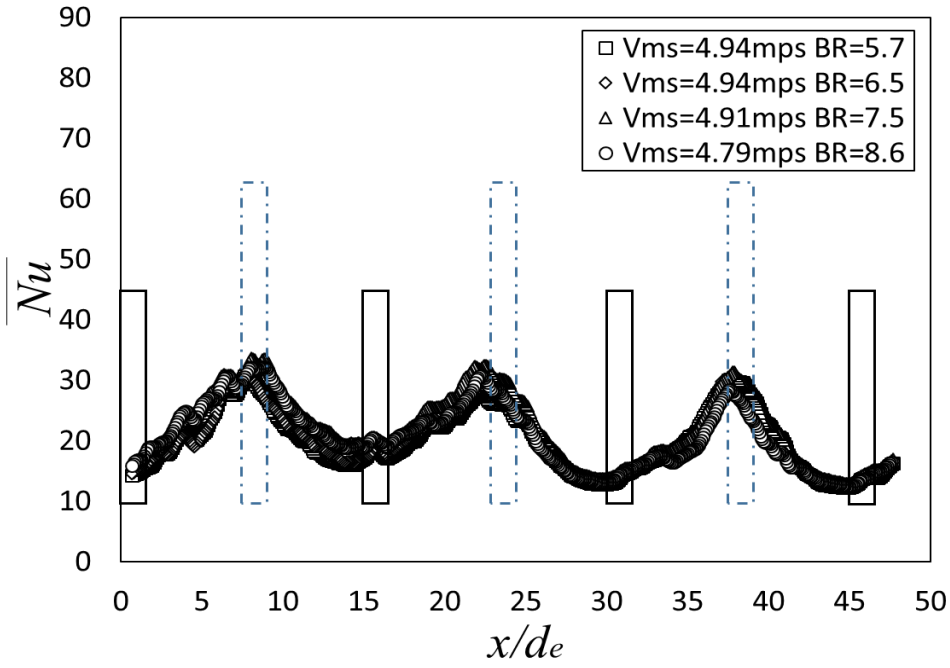

Figure 48. Line-averaged Nusselt number data for combined impingement and cross flow arrangement. Effusion hole locations are denoted by black boxes. Impingement hole locations are denoted by blue dashed boxes. Data is for CASE 4 configuration for constant Re_{imp}, as Re_{cf} varies. Re_{ms} ranges from 99,305 to 102,398, and $Re_{ms,Avg}$ ranges from 162,000 to 168,000.

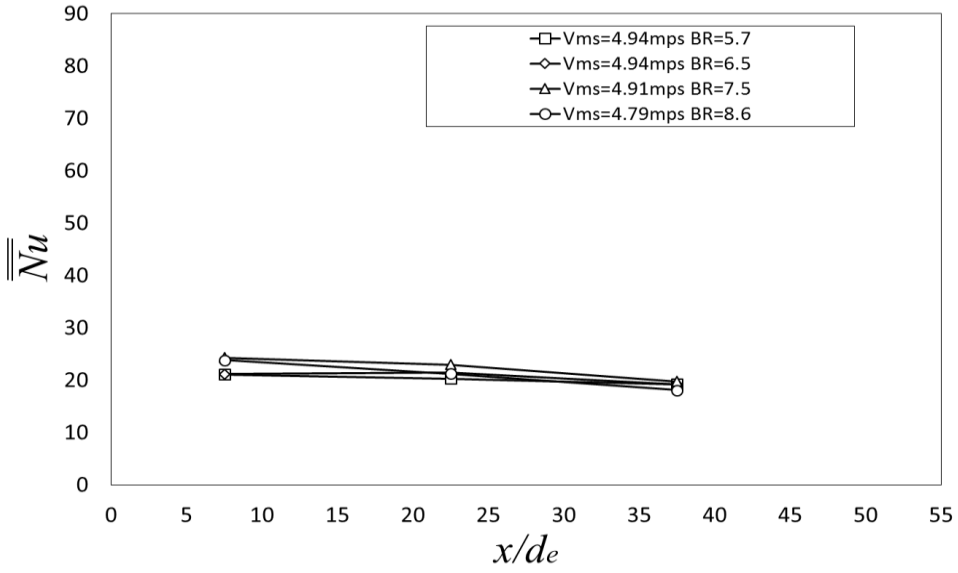

Figure 49. Spatially-averaged Nusselt number data for combined impingement and cross flow arrangement. Data is for CASE 4 configuration for constant Re_{imp}, as Re_{cf} varies. Re_{ms} ranges from 99,305 to 102,398, and $Re_{ms,Avg}$ ranges from 162,000 to 168,000.

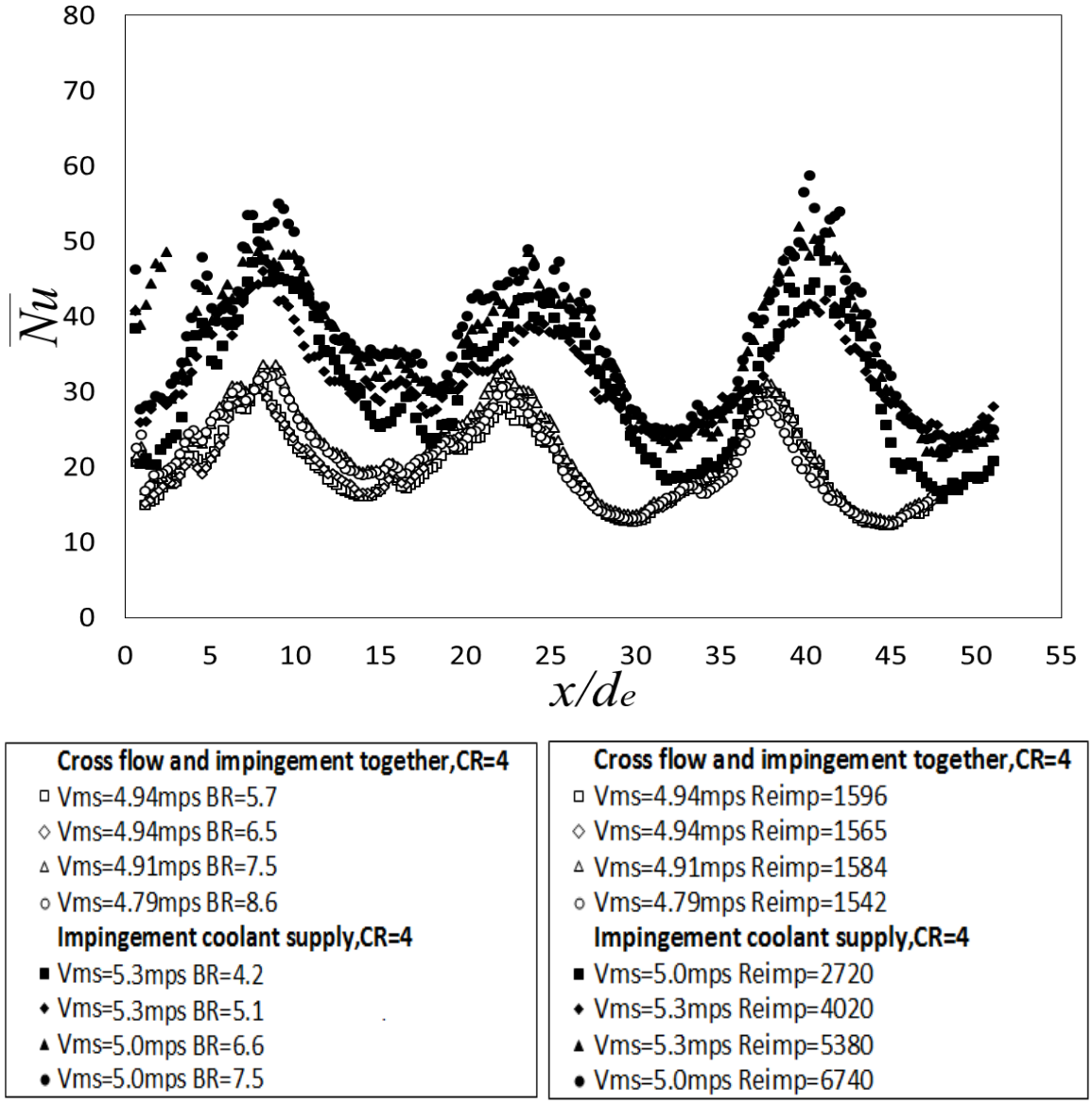

Figure 50. Line-averaged Nusselt number comparison for all experimental conditions for combined impingement and cross flow arrangement and impingement only, CR=4. Data is for CASE 4 configuration for constant Re_{imp}, as Re_{cf} varies. Re_{ms} ranges from 99,305 to 102,398, and $Re_{ms,Avg}$ ranges from 162,000 to 168,000.

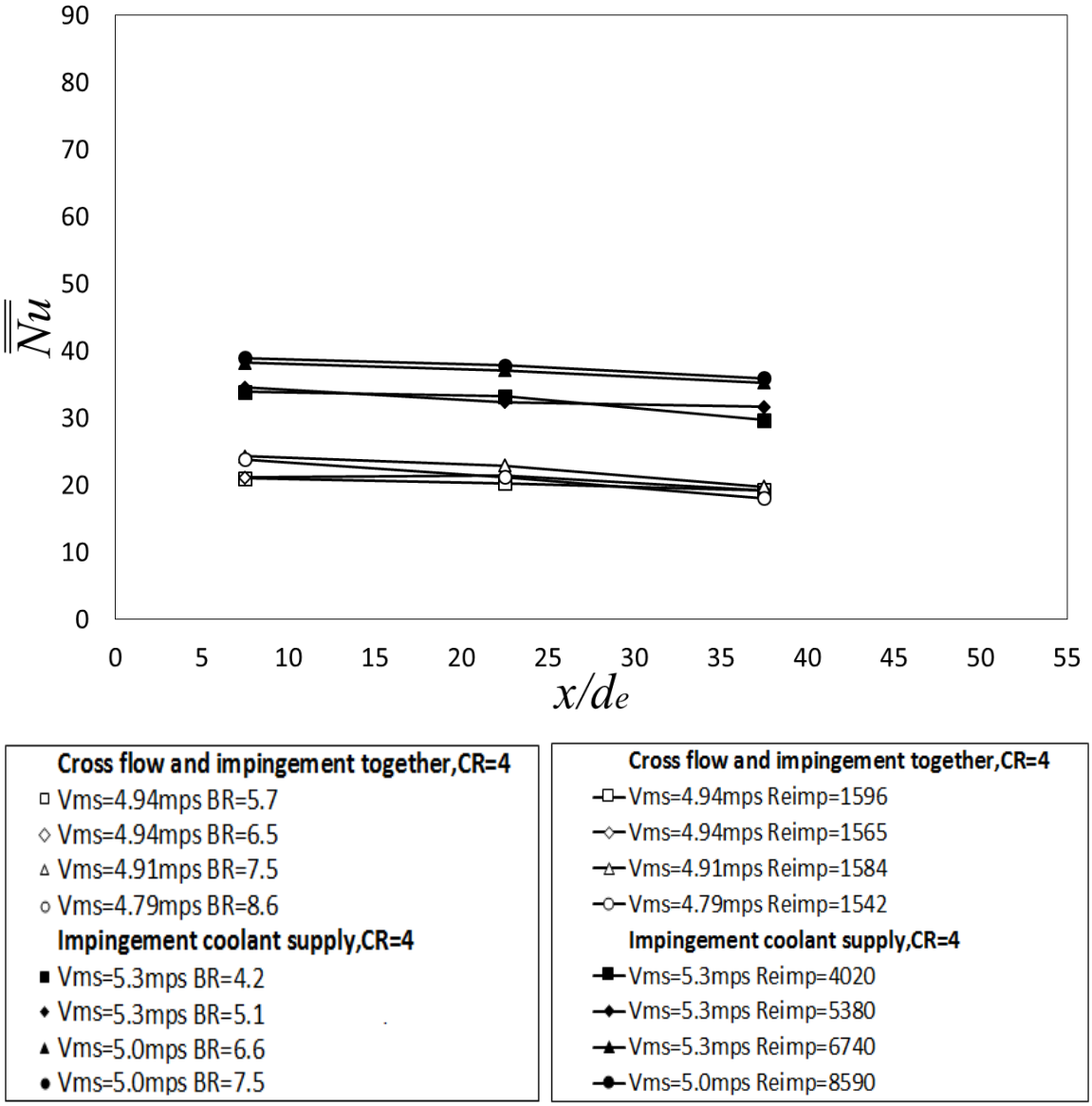

Figure 51. Spatially-averaged Nusselt number comparison for all experimental conditions for combined impingement and cross flow arrangement and impingement only, CR=4. Data is for CASE 4 configuration for constant Re_{imp}, as Re_{cf} varies. Re_{ms} ranges from 99,305 to 102,398, and $Re_{ms,Avg}$ ranges from 162,000 to 168,000.

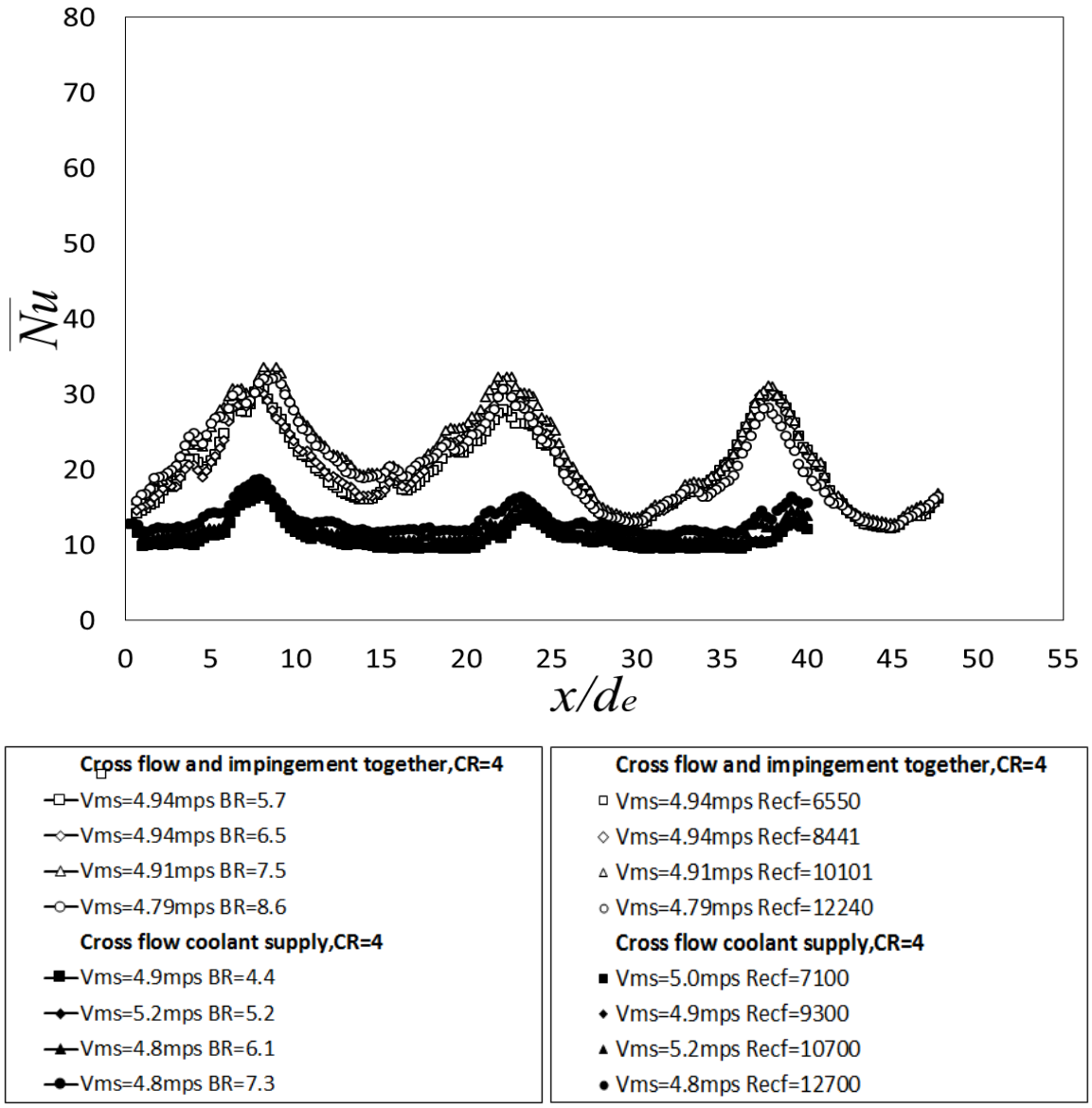

Figure 52. Line-averaged Nusselt number comparison for all experimental conditions for combined impingement and cross flow arrangement and cross flow only, CR=4. Data is for CASE 4 configuration for constant Re_{imp}, as Re_{cf} varies. Re_{ms} ranges from 99,305 to 102,398, and $Re_{ms,Avg}$ ranges from 162,000 to 168,000.

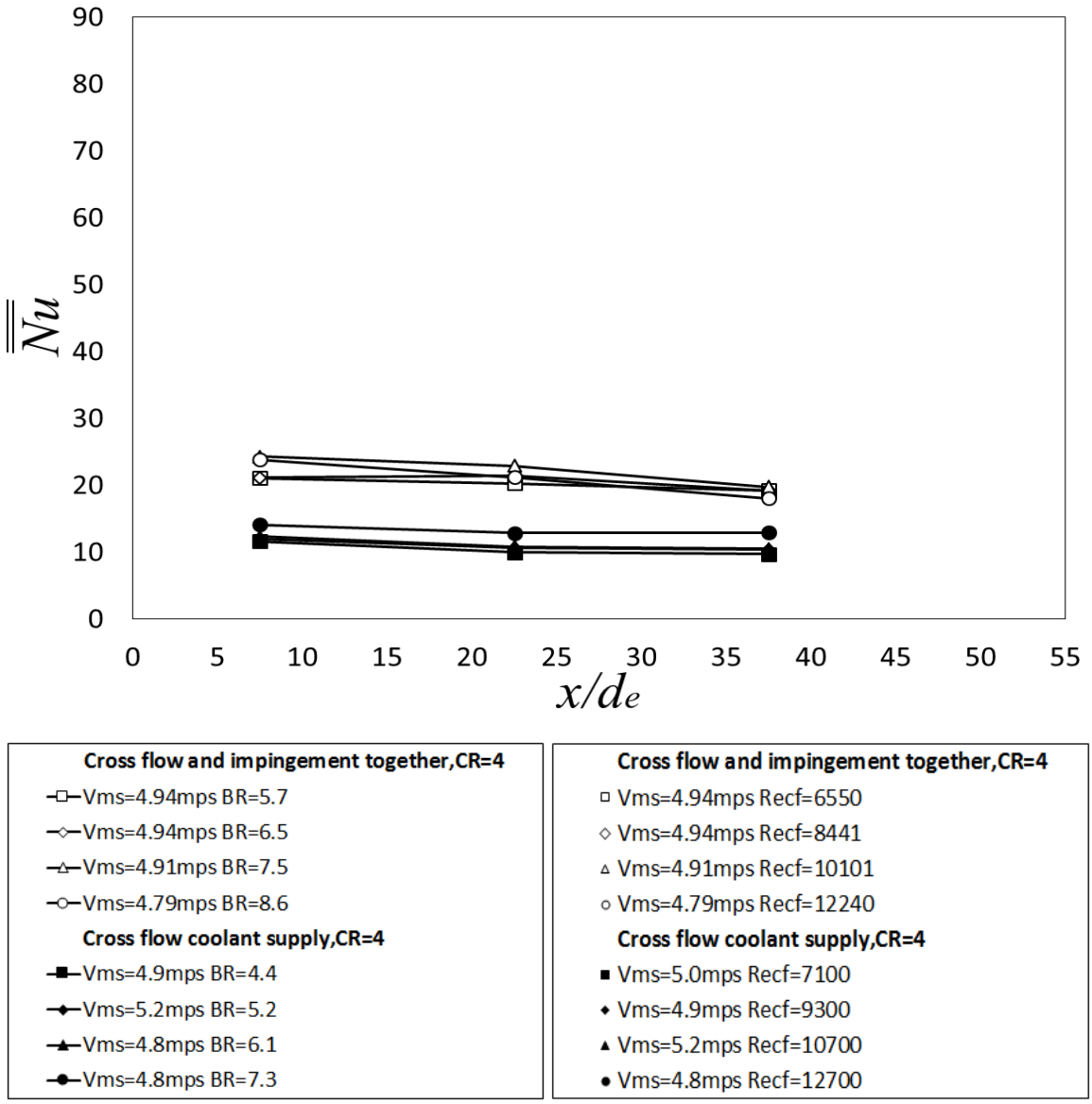

Figure 53. Spatially-averaged Nusselt number comparison for all experimental conditions for combined impingement and cross flow arrangement and cross flow only, CR=4. Data is for CASE 4 configuration for constant Re_{imp}, as Re_{cf} varies. Re_{ms} ranges from 99,305 to 102,398, and $Re_{ms,Avg}$ ranges from 162,000 to 168,000.

CHAPTER 4

SUMMARY AND CONCLUSIONS

Experimental data are provided for four different sets of experimental conditions for the coolant-side of a double wall cooled effusion test plate. This work on double wall film cooling is motivated by a need to effectively thermally protect and cool combustion chamber liners of gas turbine engines from potentially detrimental thermal effects from the hot gas flowing through the chamber. Employed are three different passages for main flow, cross flow, and impingement flow. Coolant is supplied through the cross flow channel and by means of an impingement jet array to the coolant-side of the effusion test plate. This coolant then supplies all effusion hole entrances. The impingement plate and effusion plate both contain six staggered rows of 10 holes per row, where impingement holes are offset so that each is located between effusion hole entrance locations. Installed within the effusion test plate on the coolant-side is a custom-manufactured etched-foil heater, which is employed to provide a uniform surface heat flux thermal boundary condition. The inlet and outlet of the main flow passage are configured with a contraction ratio of 4 to provide a strong favorable pressure gradient with streamwise development. Liquid crystal thermography is employed to measure spatially-resolved distributions of surface Nusselt number values along the cold-side of the effusion plate. Of particular interest is the simultaneous use of cross flow and impingement flow, as associated Reynolds numbers and mass flow rates are varied. Resulting data are compared to measured data (from previous investigations) using arrangements which employed cooling air provided either by a cross flow only configuration, or by an impingement only arrangement.

The four arrangements which utilize combination impingement and cross flow data are: (1) CASE 1: high mainstream Reynolds number/constant cross flow Reynolds number/varying impingement Reynolds number, (2) CASE 2: low mainstream Reynolds number/constant cross flow Reynolds number/varying impingement Reynolds number, (3) CASE 3: high mainstream Reynolds number/constant impingement Reynolds number/varying cross flow Reynolds number, and (4) CASE 4: low mainstream Reynolds number/constant impingement Reynolds number/varying cross flow Reynolds number. Associated Reynolds numbers for these four sets of data are provided in Table 10.

Table 10. Reynolds number results for four different experimental arrangements.

	Re_{ms}	$Re_{ms,avg}$	Re_{cf}	Re_{imp}
CASE 1	157,201-161,193	233,00-244,000	8,180-9,060	2,410-5,120
CASE 2	102,709-107,029	164,000-171,000	5,736-5,950	1,643-3,255
CASE 3	158,601-162,338	236,000-245,000	8,914-16,655	2,678-2,723
CASE 4	99,305-102,398	162,000-168,000	6,550-12,240	1,542-1,596

In the present study, surface Nusselt number distributions are strongly affected by distributions and concentrations of coolant distributed across the surface on the coolant-side of the effusion plate. Here, higher surface Nusselt number values indicate increased surface heat transfer augmentation, and improved cooling and thermal protection along on the surface. This is often due to increased local turbulent transport and the presence of impingement jet stagnation locations. Conversely, lower surface Nusselt number values indicate lower thermal protection and less surface cooling. In general, all combination flow CASES were higher in Nusselt number values than the cross flow only arrangement and lower in Nusselt number values than the impingement only arrangement, when compared at the same x/d_e location and initial blowing ratio, BR. As such, CASES 1 and 2 behave more closely to an impingement only arrangement, whereas CASES 3 and 4 behave somewhat closely to a cross flow only arrangement.

Results indicate that the impingement only arrangement provides the most effective distribution of coolant along the cold-side of the effusion test plate, when compared to the combination arrangements and to the cross flow only arrangements. As initial blowing ratio and Re_{imp} increase, while Re_{cf} is held constant, impingement flow begins to overpower the cross flow, which leads to the higher Nusselt number values for CASE 1 and 2. However, for CASES 3 and 4, the cross flow restricts the impingement flow, thus causing the Nusselt numbers to vary, with changing Reynolds number, more similarly to a cross flow only configuration, than to an impingement only configuration. Such a restriction in impingement flow results in situations where Nusselt number values decrease with increasing blowing ratio, as evidenced by CASE 3 data and by portions of CASE 4 data.

APPENDIX A

DATA FILE DIRECTORY

A listing of data files by filename now follows. These data files include both the raw and reduced data files for the results presented in this thesis. Here, $Re_{ms,Avg}$ is the average mainstream Reynolds number, calculated based on the average variation of mean mainstream velocity through the main flow test section. BR is the local effusion hole exit blowing ratio based on values of effusion hole exit and mainstream parameters, measured at the inlet of the test section.

$Re_{ms,avg}$	BR	Data File Name	Description
243861	5.9	Flow Data A1.txt - Flow Data A5.txt	Pressure readings from LabView
		Temperatures A1.txt - Temperatures A5.txt	Temperature readings from LabView
		Averages A.xlsx	Excel file to average flow data and teperature data
		High Re A.xlsx	Excel file to calculate the heat transfer data on the coolant side of the effusion test plate
241633	6.9	Flow Data B1.txt - Flow Data B5.txt	Pressure readings from LabView
		Temperatures B1.txt - Temperatures B5.txt	Temperature readings from LabView
		Averages B.xlsx	Excel file to average flow data and teperature data
		High Re B.xlsx	Excel file to calculate the heat transfer data on the coolant side of the effusion test plate
237017	8.3	Flow Data C1.txt - Flow Data C5.txt	Pressure readings from LabView
		Temperatures C1.txt - Temperatures C5.txt	Temperature readings from LabView
		Averages C.xlsx	Excel file to average flow data and teperature data
		High Re C.xlsx	Excel file to calculate the heat transfer data on the coolant side of the effusion test plate
232515	9.8	Flow Data D1.txt - Flow Data D5.txt	Pressure readings from LabView
		Temperatures D1.txt - Temperatures D5.txt	Temperature readings from LabView
		Averages D.xlsx	Excel file to average flow data and teperature data
		High Re D.xlsx	Excel file to calculate the heat transfer data on the coolant side of the effusion test plate
		Cf Cnst Cold Side High Re.xlsx	Excel file to calculate and plot the line-averaged and spatially-averaged Nusselt number distributions
		Reduced Points High Re Constant Cf.xlsx	Excel file to plot reduced data for more clear plots
		High Re Pressure Calcs Cf Cnst 7-12-2018.xlsx	Excel file to calculate experimental conditions for pressure measurements
		labVIEW Readings High Re Cnst Cf	Excel File to calculate experimental temperatures
		High Re Pressure Calcs Cf Cnst HT.xlsx	Excel file to calculate experimental conditions for heat transfer measurements

170601	5.4	Flow Data A1.txt - Flow Data A5.txt	Pressure readings from LabView
		Temperatures A1.txt - Temperatures A5.txt	Temperature readings from LabView
		Averages A.xlsx	Excel file to average flow data and teperature data
		High Re A.xlsx	Excel file to calculate the heat transfer data on the coolant side of the effusion test plate
167940	6.4	Flow Data B1.txt - Flow Data B5.txt	Pressure readings from LabView
		Temperatures B1.txt - Temperatures B5.txt	Temperature readings from LabView
		Averages B.xlsx	Excel file to average flow data and teperature data
		High Re B.xlsx	Excel file to calculate the heat transfer data on the coolant side of the effusion test plate
166360	7.3	Flow Data C1.txt - Flow Data C5.txt	Pressure readings from LabView
		Temperatures C1.txt - Temperatures C5.txt	Temperature readings from LabView
		Averages C.xlsx	Excel file to average flow data and teperature data
		High Re C.xlsx	Excel file to calculate the heat transfer data on the coolant side of the effusion test plate
164323	8.2	Flow Data D1.txt - Flow Data D5.txt	Pressure readings from LabView
		Temperatures D1.txt - Temperatures D5.txt	Temperature readings from LabView
		Averages D.xlsx	Excel file to average flow data and teperature data
		High Re D.xlsx	Excel file to calculate the heat transfer data on the coolant side of the effusion test plate
		Cf Cnst Cold Side Low Re.xlsx	Excel file to calculate and plot the line-averaged and spatially-averaged Nusselt number distributions
		Reduced Points Low Re Constant Cf.xlsx	Excel file to plot reduced data for more clear plots
		Low Re Pressure Calcs Cf Cnst 5-8-2018.xlsx	Excel file to calculate experimental conditions for pressure measurements
		labVIEW Readings Low Re Cnst Cf	Excel File to calculate experimental temperatures
		Low Re Pressure Calcs Cf Cnst HT.xlsx	Excel file to calculate experimental conditions for heat transfer measurements

244741	5.8	Flow Data A1.txt - Flow Data A5.txt	Pressure readings from LabView
		Temperatures A1.txt - Temperatures A5.txt	Temperature readings from LabView
		Averages A.xlsx	Excel file to average flow data and teperature data
		High Re A.xlsx	Excel file to calculate the heat transfer data on the coolant side of the effusion test plate
241887	6.6	Flow Data B1.txt - Flow Data B5.txt	Pressure readings from LabView
		Temperatures B1.txt - Temperatures B5.txt	Temperature readings from LabView
		Averages B.xlsx	Excel file to average flow data and teperature data
		High Re B.xlsx	Excel file to calculate the heat transfer data on the coolant side of the effusion test plate
238571	7.5	Flow Data C1.txt - Flow Data C5.txt	Pressure readings from LabView
		Temperatures C1.txt - Temperatures C5.txt	Temperature readings from LabView
		Averages C.xlsx	Excel file to average flow data and teperature data
		High Re C.xlsx	Excel file to calculate the heat transfer data on the coolant side of the effusion test plate
235544	8.4	Flow Data D1.txt - Flow Data D5.txt	Pressure readings from LabView
		Temperatures D1.txt - Temperatures D5.txt	Temperature readings from LabView
		Averages D.xlsx	Excel file to average flow data and teperature data
		High Re D.xlsx	Excel file to calculate the heat transfer data on the coolant side of the effusion test plate
		Imp Cnst Cold Side High Re.xlsx	Excel file to calculate and plot the line-averaged and spatially-averaged Nusselt number distributions
		Reduced Points High Re Constant IMP.xlsx	Excel file to plot reduced data for more clear plots
		High Re Pressure Calcs Imp Cnst 6-6-2018.xlsx	Excel file to calculate experimental conditions for pressure measurements
		labVIEW Readings High Re Cnst Imp	Excel File to calculate experimental temperatures
		High Re Pressure Calcs Imp Cnst HT.xlsx	Excel file to calculate experimental conditions for heat transfer measurements

168237	5.7	Flow Data A1.txt - Flow Data A5.txt	Pressure readings from LabView
		Temperatures A1.txt - Temperatures A5.txt	Temperature readings from LabView
		Averages A.xlsx	Excel file to average flow data and teperature data
		High Re A.xlsx	Excel file to calculate the heat transfer data on the coolant side of the effusion test plate
166736	6.5	Flow Data B1.txt - Flow Data B5.txt	Pressure readings from LabView
		Temperatures B1.txt - Temperatures B5.txt	Temperature readings from LabView
		Averages B.xlsx	Excel file to average flow data and teperature data
		High Re B.xlsx	Excel file to calculate the heat transfer data on the coolant side of the effusion test plate
164158	7.5	Flow Data C1.txt - Flow Data C5.txt	Pressure readings from LabView
		Temperatures C1.txt - Temperatures C5.txt	Temperature readings from LabView
		Averages C.xlsx	Excel file to average flow data and teperature data
		High Re C.xlsx	Excel file to calculate the heat transfer data on the coolant side of the effusion test plate
161881	8.6	Flow Data D1.txt - Flow Data D5.txt	Pressure readings from LabView
		Temperatures D1.txt - Temperatures D5.txt	Temperature readings from LabView
		Averages D.xlsx	Excel file to average flow data and teperature data
		High Re D.xlsx	Excel file to calculate the heat transfer data on the coolant side of the effusion test plate
		Imp Cnst Cold Side Low Re.xlsx	Excel file to calculate and plot the line-averaged and spatially-averaged Nusselt number distributions
		Reduced Points Low Re Constant IMP.xlsx	Excel file to plot reduced data for more clear plots
		Low Re Pressure Calcs Imp Cnst 5-30-2018.xlsx	Excel file to calculate experimental conditions for pressure measurements
		labVIEW Readings Low Re Cnst Imp	Excel File to calculate experimental temperatures
		Low Re Pressure Calcs Imp Cnst HT.xlsx	Excel file to calculate experimental conditions for heat transfer measurements

APPENDIX B

SOFTWARE DIRECTORY

A listing of software by filename, with a brief description for each of the different software used in this thesis.

Software	**File Name**	**Description**
LabView Professional Development System version 17.0 (2017)	Facility Measurements_Liquid Crystal.vi	LabView program used to collect and store raw flow condition data from thermocouples and pressure transducers, for coolant side of the effusion plate
LiquiTherm Image Processor	LiquiTherm Image Processor.bat file (version 1.0)	Used to analyze liquid crystal images into hue angle values
FlyCapture Viewer software	Point Grey FlyCap2.exe v2.9.3.11	Used to collect and store liquid crystal images
Flir ResearchIR	N/A	Used to collect and store infrared images from the infrared camera
Excel (2016)	LCCalibration.xlsx	Used to determine correlation between voltage inputs and liquid crystal hue values
Excel (2016)	N/A	Used to determine surface Nusselt number values for cold-side of the effusion test plate
MATLAB	ContourPlotCFandImp.m	Used to generate surface contour plots for cold-side heat transfer data.

REFERENCES

Al Dabagh, A., Andrews, G., Hussain, R. A., Hussain C., Nazari, A., Wu, J., 1990, "Impingement/Effusion Cooling: The Influence of the Number of Impingement Holes and Pressure Loss on the Heat Transfer Coefficient," ASME Journal of Turbomachinery, 112(3), pp. 467-476.

Andrews, G., Asere, A., Mkpadi, M., Tirmahi, A., 1986, "Transpiration cooling: Contributions of Film Cooling to the Overall Cooling Effectiveness," ASME 86-GT-136, pp. V004T09A019.

Andrews G. E., Asere A. A., Husain C. I., Mkpadi M. C., and Nazari A., "Impingement/Effusion Cooling: Overall Wall Heat Transfer," Paper Number 88-GT-290, ASME TURBO EXPO 1988: Turbine Technical Conference and Exposition, Amsterdam, The Netherlands, June 6-9, 1988

Andrews, G. E., Al-Dabagh, A. M., Asere, A. A., Bazdidi-Tehrani, F., Mkpadi, M. C., and Nazari, A., "Impingement/Effusion Cooling". AGARD Conference Proceedings 527, 80th Symposium on Heat Transfer and Cooling in Gas Turbines, AGARD Propulsion and Energetics Panel, Antalya, Turkey, pp. 30.1-30.10, October 12-16, 1992.

Andrews G. E., and Nazari, A., 1999, "Impingement/Effusion Cooling: Influence of Number of Holes On the Cooling Effectiveness For An Impingement X/D of 10.5 and Effusion X/D of 7.0," Paper Number IGTC TS-51, Proceedings of the GTSJ Int. Gas Turbine Congress, Vol. II, pp. 639 - 646.

Bailey, J. C., Intile, J., Tolpadi, A., Fric, T., Nirmalan, N. V., and Bunker, R. S., 2002, "Experimental and Numerical Study of Heat Transfer in a Gas Turbine Combustor Liner," ASME Transactions – Journal of Engineering for Gas Turbines and Power, 125(5), pp.994-1002.

Cho, H. H., and Rhee, D. H., 2001, "Local Heat/Mass Transfer Measurement on the Effusion Plate In Impingement/Effusion Cooling Systems," ASME Transactions-Journal of Turbomachinery, 123 (3), pp. 601-608.

Cho H. H., Rhee D. H., and Goldstein, R. J., 2008, "Effects of Hole Arrangements on Local Heat/Mass Transfer for Impingement/Effusion Cooling With Small Hole Spacing," ASME Transactions – Journal of Turbomachinery, 130 (1), pp. 1-11.

El-Jummah A. M., Andrews G. E. and Staggs J. E. J., "Impingement/Effusion Cooling Wall Heat Transfer Conjugate Heat Transfer Computational Fluid Dynamic Predictions," Paper Number GT2016-56961, ASME TURBO EXPO 2016: Turbomachinery Technical Conference and Exposition, Seoul, South Korea, June 13-17, 2016.

El-Jummah, A. M., Nazari, A., Andrews, G. E., and Staggs, J. E. J., "Impingement/Effusion Cooling Wall Heat Transfer: Reduced Number of Impingement Jet Holes Relative to the Effusion Holes," Paper Number GT2017-63494, ASME TURBO EXPO 2017: Turbomachinery Technical Conference and Exposition, Charlotte, North Carolina, USA, June 26-30, 2017.

FlyCapture 2.9.3.11 Viewer software, 2016, Retrieved from http://www.pgrey.com/support/downloads. [Accessed 15-Jun-2016].

Hay, J. L., Hollingsworth, D. K., 1998, “Calibration of micro-encapsulated liquid crystals using hue angle and a dimensionless temperature ", Experimental Thermal and Fluid Science, 18, pp. 251-257.

Hong S. K., Rhee D. H., and Cho H. H., 2007, “Effects of Fin Shapes and Arrangements on Heat Transfer for Impingement/Effusion Cooling With Cross-Flow,” ASME Transactions – Journal of Heat Transfer, 129 (12), pp. 1697-1707.

Jackowski, T., Schulz, A., Bauer, H.-J., Gerendas, M., and Behrendt, T., 2016, “Effusion Cooled Combustor Liner Tiles With Modern Cooling Concepts: A Comparative Experimental Study,” Paper Number GT2016-56598, ASME TURBO EXPO 2016: Turbomachinery Technical Conference and Exposition, Seoul, South Korea, June 13-17, 2016.

Ji, Y., Ge, B., Zang, S., Yu, J., and Zhang, J., 2016, “Experimental Investigation of Effusion Cooling Performance on the Liner of a Scaled Three Injector Annular Combustor,” Paper Number GT2016-57035, ASME TURBO EXPO 2016: Turbomachinery Technical Conference and Exposition, Seoul, South Korea, June 13-17, 2016.

Ji, Y., Ge, B., Zang, S., Xin, J., Ye, C., and Song, H., 2017, “Effect of Holes Array on Effusion Cooling Characteristics of a Three-Nozzle Model Combustor Liner,” Paper Number GT2017-64247, ASME TURBO EXPO 2017: Turbomachinery Technical Conference and Exposition, Charlotte, North Carolina, USA, June 26-30, 2017.

Kelly, G. B., and Bogard, D. G., 2003, “An Investigation of the Heat Transfer for Full Coverage Film Cooling,” Paper Number GT2003-38716, ASME Turbo Expo 2003, June 16–19, 2003, Atlanta, Georgia, USA.

Kline, S. J., and McClintock, F. A., 1953, "Describing Uncertainties in Single Sample Experiments," Mechanical Engineering, 75, pp. 3-8.

Krewinkel, R., 2013, “A Review of Gas Turbine Effusion Cooling Studies,” International Journal of Heat and Mass Transfer, 66, pp. 706-722.

Ledezma, G. A., Lachance, J., Wang, G., Wang, A., and Laskowski, G. M., 2016, “Experimental and Numerical Investigations of Effusion Cooling for High Pressure Turbine Components Part 2: Numerical Results,” Paper Number GT2016-56400, ASME TURBO EXPO 2016: Turbomachinery Technical Conference and Exposition, Seoul, South Korea, June 13-17, 2016.

Ligrani P, Ren Z, Vanga S, et al., 2018, “Double Wall Cooling of a Full Coverage Effusion Plate with Cross Flow Supply Cooling and Main Flow Pressure Gradient,” University of Alabama in Huntsville.

Lin, Y., Song, B., Li, B., Liu, G., and Wu, Z., 2003, “Investigation of Film Cooling Effectiveness of Full-Coverage Inclined Multihole Walls with Different Hole Arrangements,” Paper Number GT-2003-38881, TURBO EXPO 2003, Atlanta, Georgia, USA, June 16-19, 2003.

Martiny, M., Schulz, A., and Wittig, S., 1995, “Full-Coverage Film Cooling Investigation: Adiabatic Wall Temperatures and Flow Visualization,” ASME International Mechanical Engineering Congress & Exposition.

McClintic, J. W., Anderson, J. B., Bogard, D. G., Dyson, T. E., and Webster, Z. D., 2017, “Effect of Internal Crossflow Velocity on Film Cooling Effectiveness – Part I: Axial Shaped Holes,” Paper Number GT2017-64616, ASME TURBO EXPO 2017: Turbomachinery Technical Conference and Exposition, Charlotte, North Carolina, USA, June 26-30, 2017.

McClintic, J. W., Anderson, J. B., Bogard, D. G., Dyson, T. E., and Webster, Z. D., 2017, “Effect of Internal Crossflow Velocity on Film Cooling Effectiveness – Part II: Compound Angle Shaped Holes,” Paper Number GT2017-64624, ASME TURBO EXPO 2017: Turbomachinery Technical Conference and Exposition, Charlotte, North Carolina, USA, June 26-30, 2017.

Moffat, R. J., 1988, "Describing the Uncertainties in Experimental Results," Experimental Thermal and Fluid Science, 1(1), pp. 3-17.

Nguyen, M. N., Fénot, M., Lalizel, G., and Dorignac, E., 2012, “Experimental Study of Full Coverage Film Cooling Optimization,” Journal of Physics: 6th European Thermal Sciences Conference, Retrieved from http://iopscience.iop.org/1742-6596/395/1/012031. [Accessed 11-Mar-2019].

Oguntade, H. I., Andrews, G. E., Burns, A. D., Ingham, D. B., and Pourkashanian, M., 2017. “Impingement/Effusion Cooling with Low Coolant Mass Flow,” Paper Number GT2017- 63484, ASME TURBO EXPO 2017: Turbomachinery Technical Conference and Exposition, Charlotte, North Carolina, USA, June 26-30, 2017.

Ren, Z., 2018, “Investigation of Effusion, Impingement, and Cross Flow Cooling Within Double Wall Cooling Configuration,” Ph.D dissertation, University of Alabama in Huntsville, July, 2018.

Ren Z, Vanga S, Ritchie D, Click AJ, et al., 2018, “Double Wall Cooling of a Full Coverage Effusion Plate with Main Flow Pressure Gradient, Including Internal Impingement Array Cooling,” University of Alabama in Huntsville.

Rogers, N., 2015, “Performance of Full Coverage Effusion Cooling with Cross Flow Supply,” (Master’s Thesis), Retrieved from http://cdm16608.contentdm.oclc.org/cdm/ref/collection/p16608coll23/id/34605. [Accessed 11-Mar-2019].

Rogers, N., Ren, Z., Buzzard, W., Tinker, N., Sweeney, B., Ligrani, P., Hollingsworth, K., Liberatore, F., Patel, R., Moon, H-K., 2016, “Effects of Double Wall Cooling Configuration and

Conditions on Performance of Full Coverage Effusion Cooling," Proceedings of ASME Turbo Expo 2016: Turbomachinery Technical Conference and Exposition, June 13-17, 2016, Seoul, South Korea, GT2016-56515.

Sasaki, M., Takahara, K., Kumagai, T., and Hamano, M., 1979, "Film Cooling Effectiveness for Injection from Multirow Holes," ASME Journal of Engineering Power, 101(1), pp. 101–108.

Schulz, A., 2001, "Combustor Liner Cooling Technology in Scope of Reduced Pollulant Formation and Rising Thermal Efficiencies," Heat Transfer in Gas Turbine Systems (Editor: R. J. Goldstein), Annals of the New York Academy of Sciences: New York, 934, pp. 135-146.

Shi, B., Li, J., Li, M., Ren, J., and Jiang, H., "Cooling Effectiveness on a Flat Plate With Both Film Cooling and Impingement Cooling in Hot Gas Conditions," Paper Number GT2016-57224, ASME TURBO EXPO 2016: Turbomachinery Technical Conference and Exposition, Seoul, South Korea, June 13-17, 2016.

Sung, Y., Dord, A., Laskowski, G. M., Shunn, L., Natsui, G., and Kapat, J., 2016, "Detailed Large Eddy Simulations (LES) of Multi-Hole Effusion Cooling Flow For Gas Turbines," Paper Number GT2016-57957, ASME TURBO EXPO 2016: Turbomachinery Technical Conference and Exposition, Seoul, South Korea, June 13-17, 2016.

Vanga, S., 2016, "Performance of Full Coverage Effusion Cooling with a Crossflow Supply Channel, Measured using Infrared Thermography and Liquid Crystal Thermography," M.S. thesis, University of Alabama in Huntsville

Vinton, K. R., and Wright, L. M., 2017, "Effect of Flow Acceleration on Mainstream-to-Coolant Flow Interaction for Round and Shaped Film Cooling Holes," Paper Number GT2017-63818, ASME TURBO EXPO 2017: Turbomachinery Technical Conference and Exposition, Charlotte, North Carolina, USA, June 26-30, 2017.

Wang, G., Ledezma, G. A., DeLancey, J., and Wang, A., 2016, "Experimental and Numerical Investigations of Effusion Cooling for High Pressure Turbine Components Part 1: Experimental Study With PSP," Paper Number GT2016-56398, ASME TURBO EXPO 2016: Turbomachinery Technical Conference and Exposition, Seoul, South Korea, June 13-17, 2016.

Willard, J., 2013, "LiquiTherm Image Processor (Version 1.0)," [computer software program].